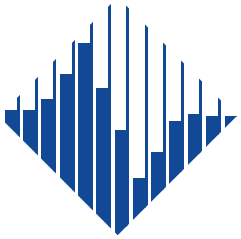

PACIFIC EARTHQUAKE ENGINEERING
RESEARCH CENTER

Shake Table Tests on a Shallow Foundation on Liquefiable Soils Supported on Helical Piles

Milad Jahed Orang

Ramin Motamed

Department of Civil and Environmental Engineering
University of Nevada, Reno

PEER Report No. 2021/07

Pacific Earthquake Engineering Research Center
Headquarters at the University of California, Berkeley
September 2021

PEER 2021/07
September 2021

Disclaimer

The opinions, findings, and conclusions or recommendations expressed in this publication are those of the author(s) and do not necessarily reflect the views of the study sponsor(s), the Pacific Earthquake Engineering Research Center, or the Regents of the University of California.

Shake Table Tests on a Shallow Foundation on Liquefiable Soils Supported on Helical Piles

Milad Jahed Orang

Ramin Motamed

Department of Civil and Environmental Engineering
University of Nevada, Reno

PEER Report 2021/07
Pacific Earthquake Engineering Research Center
Headquarters at the University of California, Berkeley

September 2021

ABSTRACT

Extensive damage to buildings and infrastructure observed during past earthquakes resulting from the liquefaction of shallow saturated soil deposits underneath structures has demonstrated the necessity for further research in the area of liquefaction-induced ground movement effects. This study explores utilizing helical piles as a countermeasure to reduce liquefaction-induced foundation settlement and investigates their seismic performance in liquefiable grounds. Two large-scale shake table test series, one without any mitigation measures and one using helical piles, were conducted using the shake table facility at the University of California, San Diego. During each test series, the soil and superstructure models were extensively instrumented and subjected to two consistently applied shaking sequences. The model ground included a shallow liquefiable layer aimed at replicating the subsurface ground conditions observed in the past earthquakes in New Zealand, Japan, and Turkey.

Liquefaction-induced foundation settlement mechanisms are broadly categorized as follows: (1) shear-induced, (2) volumetric-induced, and (3) ejecta-induced. In the first test series (referred to as the Baseline test hereafter), all these three components were realistically reproduced, while in the second test series (referred to as the Helical Pile test hereafter) the volumetric and ejecta-induced mechanisms were mainly mitigated, resulting in significant reductions in the foundation settlement.

Results from the first test series (i.e., Baseline test) indicated that the flow velocity due to the hydraulic transient gradient displayed an upward flow in the loose layer, which explains the observed sand ejecta. This series of shake table tests resulted in an average total foundation settlement of 28 cm and 42.7 cm during two shaking sequences. The measured foundation settlements were compared to the estimated foundation settlement obtained from Liu and Dobry [1997] and Bray and Macedo's [2017] simplified procedures. The observed foundation settlements generally were higher than the estimated values. In the second large-scale test series, an identical test setup to the first test series was used except for a group of four helical piles were attached to the shallow foundation to mitigate liquefaction-induced settlements. In this series of tests, a reduced excess pore-water pressure generation around the group of helical piles was observed and is mainly attributed to the increased relative density around their zone of influence as a result of installation. The foundation supported on helical piles underwent almost no differential settlement and tilt. A significant reduction in the total foundation settlement was achieved during the Helical Pile test series compared to the Baseline test series.

This shake table project is the first experimental study that reproduced all the key mechanisms mentioned above including the effects of sediment ejecta, which have not been captured in prior experimental studies.

In addition, this series of large-scale shake table tests provides a unique benchmark for the calibration of numerical models and simplified procedures to reliably estimate liquefaction-induced building settlements. Although this study introduced helical piles as a reliable and highly efficient measure to mitigate liquefaction-induced foundation tilt and settlement, the proper design

and application of helical piles in seismic areas still need thorough investigation due to possible amplified superstructure response.

ACKNOWLEDGMENTS

This study was sponsored by the Pacific Earthquake Engineering Research Center (PEER) under Contract 1130-NCTRRM. Any opinions, findings, and recommendations expressed in this material are those of the author(s) and do not necessarily express those of the funding agency(ies), PEER, or the Regents of the University of California. The authors would like to acknowledge Ram Jack for in-kind support during the helical pile tests. In addition, the authors would like to express their sincere gratitude to Professor Ahmed Elgamal and Athul Prabhakaran, and the staff of UC San Diego's Powell Laboratory for their valuable advice and support during the shake table tests.

CONTENTS

LIST OF TABLES

LIST OF FIGURES

NOTATION

A = area of the helical bearing plate

B = width of the foundation

CAV = cumulative absolute velocity

CAV_{dp} = damage potential cumulative absolute velocity for no-liquefaction free-field condition

C_c = coefficient of curvature

C_u = coefficient of uniformity

c = soil cohesion

$c1$ = -7.48 for LBS > 16 and -8.35 for LBS ≤ 16

$c2$ = 0.014 for LBS > 16 and 0.072 for LBS ≤ 16

D = pile's outer diameter

D_e = ejecta-induced settlement

D_f = foundation embedment depth

D_r = relative density

D_s = shear-induced settlement

D_t = total foundation settlement

D_v = volumetric -induced settlement

$D_{5\text{-}75}$ = significant duration (time interval between 5% and 75% of the total recorded energy)

$D_{5\text{-}95}$ = significant duration (time interval between 5% and 95% of the total recorded energy)

$(EI)_p$ = bending stiffness of pile's cross-section

e_{max} = maximum void ratio

e_{min} = minimum void ratio

FS = factor of safety

FS_L = factor of safety against liquefaction

G_s = specific gravity

H = box height

H_L = cumulative thickness of layers with $FS_L \leq 1.0$

$H(x)$ = Heaviside Step Function ($H(x) = 0$ for $x < 0$ and $H(x) = 1$ for $x \geq 1$)

I_a = arias intensity

i = hydraulic gradient

K = hydraulic conductivity of the soil

k_{dense} = hydraulic conductivity of dense specimen

k_{loose} = hydraulic conductivity of loose specimen

L = box length

LBS = liquefaction building settlement index [Eq. (4.2)]

M = bending moment

N = number of discrete 1-s time intervals

N_c, N_q, N_γ = bearing capacity factors

PGA_i = peak ground acceleration in i^{th} time interval

PGV = peak ground velocity

Q = foundation contact pressure

q_c = cone tip resistance

q' = effective overburden pressure

r_u = excess pore-water pressure ratio

Sa_1 = spectral acceleration at T = 1 sec

S_f = measured foundation settlements

S_v = spectral velocity

T = period

t = time

V = velocity of pore-water

V_s = shear-wave velocity

W = box width

γ = soil unit weight

ε = uncertainty parameter (normal random variable with zero mean and 0.50 standard deviation)

ε_1, ε_2 = strain gauge reading at opposite sides of pile

ρ_{max} = maximum mass density

ρ_{min} = minimum mass density

ϕ = angle of internal friction

τ_{cyc} = equivalent cyclic shear stress induced by earthquake

$\tau_{cyc,L}$ = cyclic shear stress required to cause liquefaction

1 Introduction

1.1 OVERVIEW

Recent research trends in the areas of infrastructure are focused on resilient design considerations with regards to performance-based engineering, which entails developing effective measures against geo-hazards. Liquefaction is one of the main geo-hazards adversely affecting resiliency and post-earthquake recovery of infrastructure in urban areas. The liquefaction phenomenon is known as one of the most destructive geo-hazards during an earthquake, which occurs mainly in loose, sandy material and sands, and to some extent with fine-grained soil. During liquefaction, the strength of the soil reduces significantly due to the increase in the excess pore-water pressure. One of the effects of this phenomenon, known as liquefaction-induced settlement, causes catastrophic loss and damage to structures overlain on a liquefiable ground. Post-disaster reconnaissance of areas affected by earthquakes has documented extensive damage to shallow foundations of structures within liquefaction-prone areas. For example, the 2010 and 2011 Canterbury Earthquake Sequence (CES) in New Zealand caused severe and widespread liquefaction throughout the town of Christchurch and subsequent damage to more than 20,000 residential buildings [Bray et al. 2014]. Similarly, over 27,000 buildings in Japan experienced substantial damage due to liquefaction during the 2011 Tohoku earthquake [Tokimatsu and Katsumata 2012]. Liquefaction has been extensively observed throughout California in its urban areas such as during the 1989 Loma Prieta earthquake, and future earthquake events can result in similar damage to structures. Having a good understanding of the above-mentioned issues is of great importance to minimize the cost, fatalities, and damage due to liquefaction.

During seismic events, foundations play a vital role in providing integrity to the structures found in soils susceptible to liquefaction. Continuing research into the performance of foundations in seismic areas is essential to maintain public safety. Seismically upgrading existing structures requires additional research to provide guidelines to properly design underpinning systems. Helical piles are a type of deep foundation used regularly to underpin both new and existing structures. Current practice lacks a cost-effective yet robust solution for underpinning residential buildings and low-story structures that protect such structures from liquefaction that occurs during earthquakes. The main goal of this research is to experimentally evaluate the performance of helical piles as an alternative solution for mitigating the settlement of shallow foundations in liquefiable soils. Additionally, this study is expected to have a broader application in the resilient design of bridges and structures by providing a more cost-effective and environmentally friendly solution to reduce the effects of liquefaction-induced settlement due to earthquakes.

1.2 BACKGROUND

Previous research has provided valuable insight into the liquefaction phenomenon and its subsequent effects. This includes the observed behavior of foundation performance through numerous case histories around the world. The literature on liquefaction-induced settlement mechanisms and subsequent mitigation procedures to estimate the amount of free-field and foundation settlement due to liquefaction is well populated. Additionally, various measures have been introduced to minimize the associated damage of the liquefaction effects including liquefaction-induced settlement and lateral spreading of the ground. All of the above-mentioned aspects are further described below.

1.2.1 Documented Case Histories

Documented case histories regarding the devastating effects of liquefaction during past earthquakes have rendered valuable information to the researchers. Past earthquakes, including the 1964 Niigata earthquake in Japan and the 1990 Luzon Philippine earthquake, caused extensive damage to structures and the built environment [Yoshimi and Tokimatsu 1977; Adachi et al. 1992]. Recent examples of damaging earthquakes—such as the 2010–2011 Canterbury Earthquake Sequence (CES) in New Zealand and the 2011 Tohoku earthquake in Japan— are modern examples of earthquakes that have caused considerable liquefaction-induced damage to buildings and their foundations [Cubrinovski et al. 2011; Yasuda et al. 2012; Cubrinovski 2013; and Henderson 2013]. Excessive foundation settlements were observed during CES in 2010–2011, where field reconnaissance reported differential settlements as high as 12 cm in some buildings after the 2011 Christchurch earthquake [Bray et al. 2017]). In many cases, the differential settlement and tilt of the foundations resulted in the demolition of buildings after the CES [Bray et al. 2014]. Other documented case histories such as the 1999 Kocaeli earthquake in Turkey [Bray and Stewart 2000; Sancio et al. 2002; and Bray et al. 2004] and 2010 Maule, Chile, earthquake [Bray and Frost 2010; Bray et al. 2012] also illustrate the catastrophic nature of liquefaction phenomenon and its adverse effects on the superstructures in urban areas.

Consequences of liquefaction include lateral spreading of the ground, which has been extensively documented at port facilities in Japan, as well as settlement of structures supported on shallow foundations. Liquefaction has caused extensive damage to lifeline facilities and pipeline systems due to the induced ground deformation. Lateral displacement of the soil and subsequent countermeasures to tackle this issue have been studied using 1*g* shake table tests [Motamed and Towhata 2009; Motamed et al. 2009; Motamed et al. 2013; and Ebeido et al. 2019a] and dynamic centrifuge experiments [Zeghal et al. 1999; Dobry et al. 2001; Abdoun et al. 2003; and Boulanger et al. 2003]. The liquefaction-induced movement of structures during strong ground motion has been further evaluated using numerical analyses, experimental studies, and field reconnaissance, which are summarized below.

1.2.2 Liquefaction-Induced Foundation Settlement

Past research on the behavior of shallow foundations in liquefiable soils consists of utilizing shake table tests [Yoshimi and Tokimatsu 1977; Kokusho 1999; Jacobs 2016; Rasouli et al. 2016; Toth and Motamed 2017; Honnette 2018; Jahed Orang et al. 2019a,b; Bahadori et al. 2020; Prabhakaran et al. [2020a]; Jahed Orang et al. 2021a,b], centrifuge experiments [Lambe and Whitman 1985; Liu and Dobry 1997; Hausler [2002]; Dashti et al. [2010a,b]; Hayden et al. [2015]; Jafarian et al. [2017]; Kirkwood and Dashti [2018]; Mehrzad et al. [2018]; Tokimatsu et al. 2019], field reconnaissance [Yoshimi and Tokimatsu 1977; Adachi et al. 1992; Bray and Frost 2010; Cubrinovski et al. [2010, 2011]; Tokimatsu et al. 2011; Tokimatsu and Katsumata [2012]; Bray et al. 2014], and numerical simulations [Dashti and Bray 2013; Karamitros et al. 2013; Karimi and Dashti 2016; Karimi et al. 2018; and Macedo and Bray 2018]. These studies have investigated the controlling mechanisms of liquefaction-induced building settlement and the effects of key parameters on the overall foundation response. The hierarchy of the highlighted research and the evolutionary progress regarding the mechanisms of the liquefaction-induced foundation settlement are summarized hereafter.

The 1964 Niigata earthquake resulted in the widespread liquefaction-induced settlement of buildings, attracting the interest of researchers in field reconnaissance that was followed by experimental research. During the Niigata event, 340 reinforced concrete buildings experienced damage resulting from liquefaction. Field reconnaissance after the event estimated that liquefaction occurred to maximum depths of 20 m, and maximum building settlements reached 3.8 m [Yoshimi and Tokimatsu 1977]. In addition to the field observations, Yoshimi and Tokimatsu [1977] conducted scaled 1*g* shake table tests to explore the effects of different parameters on building settlement as a result of liquefaction in sub-soils. Their study is believed to be the first experimental research focused on the behavior of shallow foundations in liquefiable soils. Based on the documented case histories from the 1964 Niigata earthquake and the complementary scaled 1*g* shake table tests, Yoshimi and Tokimatsu [1977] concluded that the average settlement (S) normalized by the thickness of the liquefiable layer (D) shows an inverse relation with building width (B).

Contributing mechanisms to liquefaction-induced settlement have been widely studied. For example, Tokimatsu and Seed [1987] and Ishihara and Yoshimine [1992] proposed empirical procedures assuming free-field conditions. One of the very first studies regarding settlement of ground due to liquefaction phenomenon was conducted by Ishihara and Yoshimine [1992], who used simple shear tests to correlate the volumetric strain (ε_v) with the relative density (D_r) of clean sand and a factor of safety (FS) against liquefaction. The predicted amount of settlement based on the laboratory test results was compared to the observed settlements from the 1964 Niigata earthquake. The amount of volumetric strain for clean sand was calculated based on the FS against liquefaction and relative density of each layer with a chart that leads to the calculation of overall ground settlement by integrating the volumetric strains generated within each layer. The methodology proposed by Ishihara and Yoshimine [1992] allows the calculation of ground (i.e., free-field) settlement due to liquefaction during earthquakes but does not account for external loads (i.e., structures and foundations).

Liu and Dobry [1997] conducted eight centrifuge tests to examine settlement characteristics of circular foundations founded on liquefiable soils. They also reviewed two field case histories, which included the 1964 Niigata and the 1990 Luzon Philippine earthquakes to compare their experimental results. They reported that the degree of settlement is dependent upon foundation width and the liquefiable layer thickness, which was in line with the conclusions drawn by Yoshimi and Tokimatsu [1977].

Dashti et al. [2010a] conducted centrifuge experiments to model the mechanisms of liquefaction-induced settlement that identified the effects of shear-induced mechanism along with partial drainage component of volumetric-induced mechanism as the dominant mechanisms contributing to the settlement of buildings in liquefiable soils. The dependency of these mechanisms on the characteristics of ground motion, subsurface conditions, and superstructure was also presented in Dashti et al. [2010a]. Liquefaction-induced foundation settlement has been now been categorized into three main mechanisms: (1) shear-induced, (2) volumetric-induced, and (3) ejecta-induced, where each mechanism is further sub-categorized to its contributing effects, which are briefly discussed here. The mechanisms contributing to the volumetric-induced settlement are partial drainage, sedimentation or solidification, and post-liquefaction reconsolidation. The shear-induced settlement is attributed to the partial bearing capacity failure of the foundation and soil–structure–interaction (SSI) induced ratcheting displacement near the edges of the foundation [Bray and Dashti 2014]. These effects can be captured using numerical simulations such as FLAC-2D, FLAC-3D [Dashti and Bray 2013; Karamitros et al. 2013; and Macedo and Bray 2018], or OpenSees [Karimi and Dashti 2016 and Karimi et al. 2018].

In a recent paper, Motamed et al. [2020] discussed the use of different numerical simulation techniques and their efficiency in predicting liquefaction-induced foundation and free-field settlements. The ejecta-induced settlement is manifested by the sand boils on the ground surface. The ground failure indices, along with the correlations between ejecta volume and foundation settlement, can be used to further quantify ejecta-induced settlement [Bray and Macedo 2017]; Jahed Orang et al. 2019a]. Researchers have observed that much of the foundation settlement takes place during shaking, indicating a higher contribution of shear-induced mechanisms and partial drainage due to high hydraulic transient gradients [Dashti et al. 2010a,b; Bray and Dashti 2014].

In a more recent study, Bray and Macedo [2017] proposed a simplified method to estimate the shear-induced element of liquefaction-induced building settlement and provided a framework to estimate it along with the volumetric-induced settlement based on past studies. They made further recommendations on how to estimate the ejecta-induced settlement to add to the previous two components for estimating the overall settlement of buildings due to liquefaction. Lu [2017] and Bullock et al. [2018] also presented semi-empirical procedures to calculate the total settlement of the foundation due to liquefaction. In this report, Bray and Macedo's [2017] simplified procedure is employed to estimate the shake table settlement results and to compare them with the observed values.

1.2.3 Liquefaction Mitigation Measures

In addition to better understanding the key mechanisms of liquefaction-induced foundation settlement, it is essential to evaluate different ground improvement and foundation underpinning techniques. Several studies examined various ground improvement techniques that considered the contributing mechanisms of liquefaction-induced settlement. Among these liquefaction mitigation measures are the use of ground densification methods [Liu and Dobry 1997; Yegian et al. 2007; Dashti et al. 2010a,b; Olarte et al. 2017; and Rasouli et al. 2018]; drainage methods such as using underground columns [Ashford et al. 2000; Adalier et al. 2003; Badanagki et al. 2018 and Bahmanpour et al. 2019], Prefabricated vertical drains (PVD) [Howell et al. 2012; Olarte et al. 2017; Paramasivam et al. 2018; and Kirkwood and Dashti 2019], and diagonal drains [Rasouli et al. 2018]; ground bracing methods such as gravel drains [Hayden and Baez 1994; Iai et al. 1994; and Adalier et al. 2003], in-ground structural walls (i.e., sheet pile walls) [Olarte et al. 2017 and Rasouli et al. 2018], and soil-cement walls [Khosravi et al. 2016 and Boulanger et al. 2018]; microbial induced calcite precipitation (MICP) [Montoya et al. 2013 and Darby et al. 2019]; induced partial saturation [Eseller-Bayat et al. 2013; Mousavi and Ghayoomi 2019; and Mousavi and Ghayoomi 2021]; and the use of geocomposite and geogrid reinforcement [Bahadori et al. 2020].

The listed ground improvement techniques address some of the liquefaction-induced settlement mechanisms, providing varying mitigation efficiencies depending on different ground conditions and shaking intensities. Prabhakaran et al. [2020a] studied the use of polymer injection to minimize liquefaction-induced foundation settlement using large-scale shake table tests. The results indicated the salient performance of a shallow foundation in a shallow liquefiable stratum rehabilitated with synthetic polymer. Although various methods provide some extent of efficiency in reducing foundation tilt and settlement, the cost-effectiveness and higher-order efficiencies in mitigating liquefaction-induced settlement still need further investigation.

1.2.4 Helical Piles

The behavior of pile foundations in liquefied and lateral spreading grounds has been investigated through 1*g* shake table experiments [Motamed and Towhata 2009; Motamed et al. 2009; Motamed et al. 2013; and Ebeido et al. 2019a] and centrifuge testing [Zeghal et al. 1999; Dobry et al. 2001; Abdoun et al. 2003; and Boulanger et al. 2003]. Although several types of deep foundations have been studied, there is a lack of knowledge regarding the response of helical piles in the liquefiable grounds.

Helical piles are a type of deep-foundation element that are used for underpinning foundations in existing and new construction, especially in areas with limited access and low headroom. In addition, helical piles have the benefit of fast and easy installation with minimal equipment. The main components of helical piles consist of a lead section, an extension part, helical plates, and coupling connections [Perko 2009]. Due to the increasing utilization of helical piles, evaluation of their seismic response is of great importance. Helical piles could be a cost-effective solution for retrofitting low-story buildings in areas susceptible to liquefaction. Although

the satisfactory performance of helical piles has been observed during past earthquakes in New Zealand, Japan, and the United States, design codes do not address their use in highly seismic zones [Cerato et al. 2017]. Their efficacy in mitigating the effects of liquefaction has prompted recent interest in the dynamic behavior of helical piles.

Past published studies on the dynamic behavior of helical piles examined the post-cyclic axial capacity considering various parameters such as helix number, helix size, shaft size, and helical pile type, including reinforced and unreinforced grouted pulldown micropiles [El Naggar and Abdelghany 2007a,b; Abdelghany 2008; Cerato and Victor 2008, 2009]. Past research has expanded the knowledge on the behavior of helical piles under axial loading (static and dynamic) in various subsurface ground conditions. Recently, the dynamic response of different helical piles and helical pile groups in dense dry sand has been recently examined using shake table experiments.

Recent large-scale shake table test at the UCSD outdoor shake table facility [ElSawy et al. 2019a]) and scaled 1*g* shake table test at UNR [Jahed Orang et al. 2019b] shed light on the adequate performance of helical piles in dry sand. ElSawy et al. [2019a, b] conducted a series of full-scale 1*g* shake table experiments using UCSD's large high-performance outdoor shake table (LHPOST) to evaluate the dynamic behavior of different helical piles with different shaft shape, length and size with variable top weights, and number of helices. Ten steel piles (9 helical piles and 1 driven pile) located within 1 m (i.e., center to center) from each other were installed in a uniform dense sand layer. Two different earthquake loadings, including Northridge (1994) and Kobe (1995), with different intensities and frequency content, were applied as input motions to assess the dynamic behavior of helical piles. All of these shake table experiments intended to examine several parameters such as the effects of loading frequency and intensity, installation methods, number of helices, pile shaft shape, and pile group damping characteristics [ElSawy et al. 2019a,b; Jahed Orang et al. 2019b; and Shahbazi et al. 2020a,b]. Yet, the seismic performance of helical piles in liquefiable ground conditions and their efficiency in improved soil–pile–foundation response to liquefaction-induced settlement and tilt has not been well understood.

1.3 RESEARCH OBJECTIVES

Two large-scale shake table test series were conducted to evaluate the performance of a shallow foundation in a layered soil profile. The first test series were conducted without any mitigation measures (i.e., Baseline tests); the second test series tested a group of helical piles used as a liquefaction mitigation measure (i.e., Helical Pile tests). The main purpose of this research was to evaluate using helical piles as a mitigation measure against liquefaction-induced shallow foundation settlement. The UCSD large-scale 1*g* shake table is able to replicate ground conditions observed in recent earthquakes in Japan, New Zealand, Turkey, and the United States [Bray et al. 2004; Bray et al. 2014; and Luque and Bray 2017]. An overview of various objectives followed through this research are summarized below:

- Reliably reproduce all the mechanisms controlling the behavior of shallow foundations underlain by near-surface liquefiable soils using a prototype soil profile.

- Provide a holistic understanding of the phenomenon of liquefaction-induced building settlement where surficial loose liquefiable soils are located at shallow depths.
- Gain knowledge on the contribution of each liquefaction-induced foundation settlement mechanism during the Baseline and Helical Pile Tests.
- Realistically reproduce surface manifestation of liquefaction (sand ejecta) and quantify its contribution to the total foundation settlement
- Evaluate the performance of helical piles in surficial liquefiable deposits while supporting a shallow foundation.
- Compare the existing remediation methods and the use of helical piles as a mitigation measure.
- Provide greater efficacy in reducing liquefaction-induced foundation settlement and tilt.

The experimental data gleaned from these tests can be used as a benchmark to validate numerical simulations of liquefaction-induced building settlements and evaluate the effectiveness of different liquefaction mitigation measures. The overall scope of this study was to assess a cost-effective remedial measure for liquefaction-induced foundation settlements, including helical piles and their efficacy in reducing liquefaction-induced foundation settlements.

1.4 ORGANIZATION OF THE REPORT

This report is compiled in six chapters. Below, a summary of the general content provided in each chapter is explained:

Chapter 1: Introduction. This chapter provides an overview of the field reconnaissance on liquefaction and its effects during past earthquakes. A literature review about liquefaction-induced mechanisms, liquefaction mitigation measures, and helical piles is also provided in this chapter. Finally, the research objectives for this project are presented.

Chapter 2: Shake Table Testing Program. This chapter provides details regarding the shake table testing program for the two test series. The model preparation—including soil, foundation, and superstructure, instrumentation, and shaking sequences—is discussed separately for each test series (i.e., Baseline and Helical Pile tests).

Chapter 3: Experimental Results. This chapter presents the major findings through these test series. Detailed discussions regarding excess pore-water pressure generation (EPWP), the effect of transient hydraulic gradients, shear stress–strain hysteresis response, variation of damage potential cumulative absolute velocity at different depths and locations, foundation tilt and differential settlement, liquefaction-induced foundation and near-foundation settlement, surface manifestation of liquefaction (ejecta), and contribution of each mechanism are discussed.

Chapter 4: Liquefaction-Induced Building Settlement Estimation. This chapter discusses the procedures used for estimating liquefaction-Induced foundation settlement. Each liquefaction-

induced settlement mechanism is estimated separately, and a comparison between various procedures and the measured foundation settlement is provided

Chapter 5: Efficiency Evaluation of Different Mitigation Measures. This chapter describes two efficiency evaluation methods to assess various ground improvement methods for mitigating liquefaction-induced settlement and tilt. A final discussion considers the influence of different countermeasures on the superstructure response.

Chapter 6: Concluding Remarks. This chapter summarizes the major findings and results of this shake table study and provides preliminary recommendations about the applicability and limitations of the test results.

2 Shake Table Testing Program

2.1 LARGE-SCALE SHAKE TABLE TESTING PROGRAM

This study conducted a series of two separate shake table tests at UCSD's Powell Laboratory. Herein, the first test series is referred to as the "Baseline" tests, and the second series is referred to as the "Helical Pile" tests. In the Baseline test series, no mitigation measure was applied, and the of these tests was to focus on the mechanisms controlling the response of shallow foundations on liquefiable soils. In the Helical Pile test series (the second test series), four single-helix helical piles were used to underpin the shallow foundation against liquefaction-induced settlement. Two shaking sequences were conducted for each test series where the first shake is referred to as "Shake 1-1" and "Shake 1" and the second shake is referred to as "Shake 1-2" and "Shake 2" throughout this report. Details regarding the shake tale testing program for the Baseline test are provided in Section 2.2.

2.2 BASELINE TEST SERIES

A series of large-scale shake table tests were conducted at the shake table facility at UCSD's Powell Laboratory in June 2018 to evaluate the effects of liquefaction-induced settlement on shallow foundations. The facility is equipped with a large laminar soil box with internal dimensions of 3.9 m (L) × 1.8 m (W) × 2.9 m (H), shown Figure 2.1, which was used to conduct a two-phase liquefaction experimental study sponsored by the Pacific Earthquake Engineering Research (PEER). The first phase, which included no mitigation strategy, is presented herein and is referred to as the "Baseline" test throughout this report. The second phase of the test series consisted of a group of helical piles as a mitigation strategy.

Section 2.2 focuses on the results of the first phase of the large-scale tests, which is intended to establish a baseline for future shake table tests with different mitigation measures. A three-layer soil model was tested, consisting of saturated dense and loose layers overlain by medium dense, unsaturated crust layer. The physical ground model simulates prototype ground conditions representative of soil profiles with shallow liquefiable layers observed at specific locations during the Adapazari 1999 Kocaeli earthquake [Bray et al. 2004]) and Christchurch 2010–2011 Canterbury Earthquake Sequence (CES) where FTG-7 and CTUC buildings were located [Bray et al. 2014; Luque and Bray 2017]. The input motion sequences (Shake 1-1 and Shake 1-2) were applied, with peak acceleration ranging from 0.53g to 0.66g and a constant frequency of 2 Hz for

15 sec including 6-sec cyclic ramp up, followed by 6 sec of uniform amplitude motion, and finally 3 sec of tapering down. These input motions were as-recorded motions without any filtering. Table 2.1 provides a summary of the target and achieved peak accelerations of the input motions in the shake table tests as well as some additional parameters. The target input motions were somewhat lower than the achieved table motion (table feedback). Although the table's actual motions were higher, the achieved input motions were approximately similar to the motions recorded during the Christchurch event at two different stations in terms of PGAs. The table acceleration time histories are illustrated in Figure 2.2. Table 2.2 presents the achieved relative densities of soil layers, depth of ground water, and foundation dimensions. Further details about the model configuration, instrumentation, soil properties, and shaking sequences in the Baseline test are discussed below.

Table 2.1 Shaking sequences and motion parameters for Baseline tests.

Parameters	Shake 1-1	Shake 1-2
Target peak acceleration (*g*)	0.15	0.30
Achieved peak acceleration (*g*)	0.53	0.66
I_a (m/sec)	3.42	9.21
CAV^*(*g*.sec)	1.35	2.36
CAV_{dp} (g.sec)	1.28	2.28
$D_{5\text{-}95}$ (sec)	10.10	9.74
$D_{5\text{-}75}$ (sec)	7.97	7.62

*For 25 sec of recorded data.

Table 2.2 Relative density and ground water level for Baseline tests.

Layer	D_r (%)	Foundation dimensions (*L*W*H*) (m)	G.W. level below ground (m)
Crust	50-55	1.3*0.6*0.4	-0.6
Liquefiable	40-45		
Dense	85-90		

Figure 2.1 **Shake table facility and laminar soil box at UC San Diego's Powell Laboratory.**

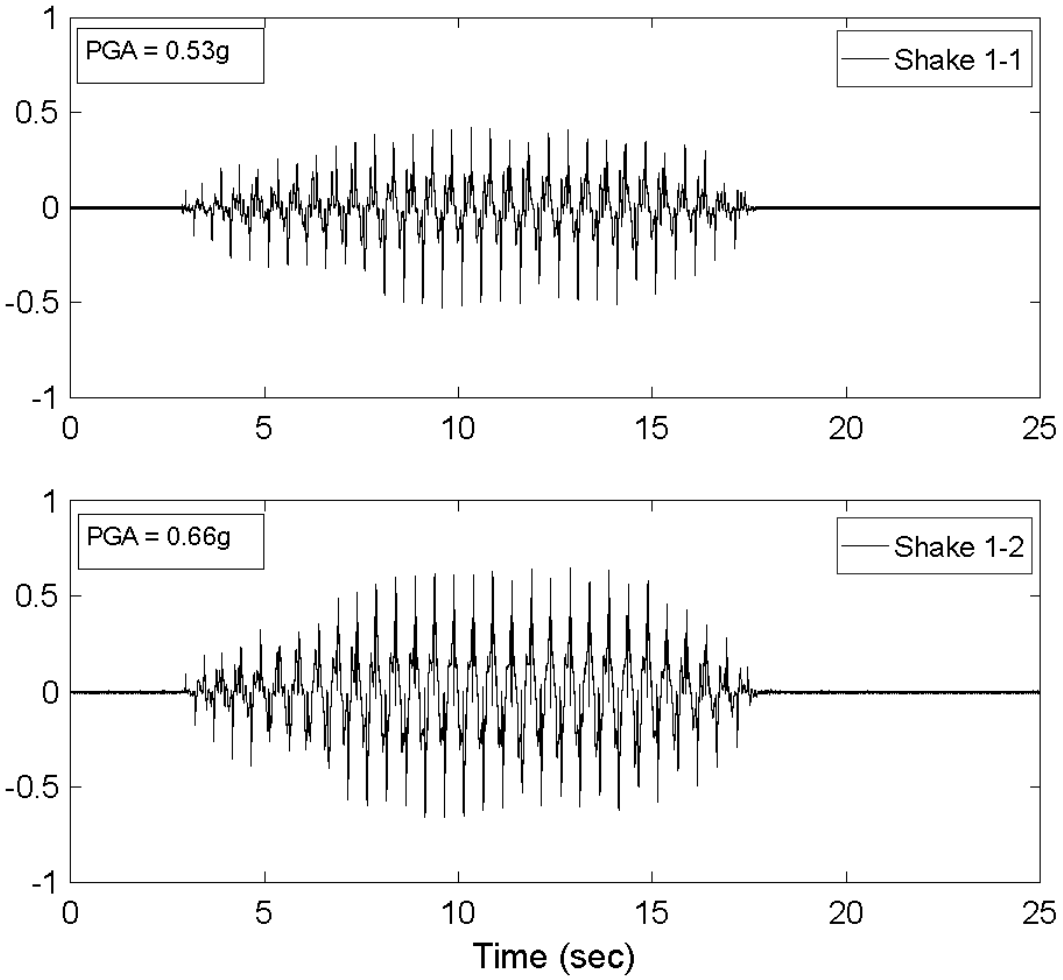

Figure 2.2 Acceleration time histories for shaking sequences.

2.2.1 Model Preparation and Instrumentation

This study aimed at reproducing a realistic prototype model ground in the shake table testing program that included shallow liquefiable soils. Some of the field case studies used to develop the model ground profile in the experiments are briefly reviewed herein. For example, Bray et al. [2014] documented that the critical liquefiable soil layer thicknesses under the southern part of the CTUC building and the northern part of the SA building during CES were 2.5 m and 0.7 m, respectively. Additionally, Bray et al. [2004] found shallow layers of liquefiable material (i.e., only a meter or so in thickness) during the 1999 Kocaeli earthquake in Adapazari, Turkey. These case studies, which highlighted the importance of shallow surficial liquefiable soil layers on liquefaction-induced building settlements, were carefully reviewed and used to establish a representative model ground in this research using the large-scale laminar soil box at UCSD. This allowed a realistic model ground to be prepared to reproduce all the mechanisms of liquefaction-

induced settlement of a shallow foundation including sand ejecta and evaluate its performance during strong ground shaking.

The laminar soil box is made of 43 steel frames with a total mass of 4229 kg mounted on 16 cold-rolled steel pipes to minimize boundary effects [Ebeido et al. 2019b]. The model ground consisted of three layers; dense, loose-liquefiable, and unsaturated crust. A 1-m-thick dense layer was overlain by a 1.3-m-thick liquefiable loose sand layer, underlying 0.6 m of medium dense crust layer. The achieved relative densities for these layers are presented in Table 2.2. The soil used to build the model was Ottawa F-65 sand in three different layers with varying relative densities (D_r). A summary of the properties of Ottawa F-65 sand is presented in Table 2.3; additional details can be found in Bastidas [2016]. The dense layer was compacted in a moisture-conditioned state in three equal lifts using a handheld vibratory compactor. The achieved relative density for the dense layer was about 85–90%. After reaching the desired thickness for the dense layer, saturation was achieved by adding water through two vertically positioned pipes located at each corner of the laminar box. The vertical pipes were conjoined using a system of horizontally connected perforated pipes positioned at the base of the soil box. Care was taken to ensure that the dense layer was not subjected to boiling conditions during saturation. During saturation, the initial water level was raised to one-third of the anticipated height of the loose layer for the next step of model preparation. As the middle liquefiable layer was being constructed, a free water level was maintained to ensure full saturation. Before the construction of the loose liquefiable layer, ten white-noise motions were applied to further densify the dense layer. The loose liquefiable layer was built by pluviating dry Ottawa F65 sand through two sets of screens (one below the sand hopper and one on top of recent layer with reasonable offset, ensuring a constant height of fall) into the water. The relative density of the loose layer was about 40–45% based on weight-volume calculations. Finally, the top crust layer was built through the air pluviation method using only one screen below the hopper. The foundation was placed on the soil model after the thickness of crust layer reached 20 cm. The final thickness of the crust was about 60 cm, and the achieved relative density of the crust layer was about 50–55%. The initial water content of crust layer material (5%) along with the capillary rise of the water inside this layer resulted in an unsaturated crust layer. All relative densities in Table 2.2 were calculated based on the weight of the soil used to build the layer and its corresponding volume as occupied in the laminar box. A dynamic cone penetrometer test (DCPT) was conducted to estimate relative densities for each layer. The calculation of relative density based on the DCPT data yielded reasonable results only for the dense layer—about 83%—because the cone tip penetrated into crust and loose layer with its weight without the application of any force.

To assess the dynamic response of superstructure and three-layered model ground, extensive instrumentation was installed to measure displacements, pore-water pressure, and accelerations at different depths. A total of 134 instruments were used in this study to capture the seismic performance of the soil–foundation–structure system. Table 2.4 presents a breakdown of the employed instruments, and Figure 2.3 illustrates the instrumentation layout. As shown in Figure 2.3, three arrays of accelerometers and pore pressure sensors were utilized in the north of, south of, and below the foundation to capture acceleration and pore-water pressure. A total of 13 string potentiometers were also employed to capture the horizontal displacement of the laminar

box at different depths. Four string potentiometers and four linear potentiometers were used to measure the foundation and free-field ground settlements, respectively.

Table 2.3 Ottawa F-65 sand properties.

Parameter	Value
Specific Gravity (G_s)	2.65
Maximum Void Ratio (e_{max})	0.853
Minimum Void Ratio (e_{min})	0.503
Coefficient of curvature (C_c)	0.96
Coefficient of uniformity (C_u)	1.61
Maximum mass density, ρ_{max} (kg/m^3)	1759
Minimum mass density, ρ_{min}, (kg/m^3)	1446
Hydraulic conductivity of loose specimen, k_{loose} (cm/sec)	0.022
Hydraulic conductivity of dense specimen, k_{dense} (cm/sec)	0.016

Source: Data from Bastidas [2016].

Table 2.4 Type and number of instruments for Baseline tests.

Type	Accelerometer	High resolution accelerometer	PWP sensors	String potentiometer	Linear potentiometer	Total
Number	35	28	47	18	6	134

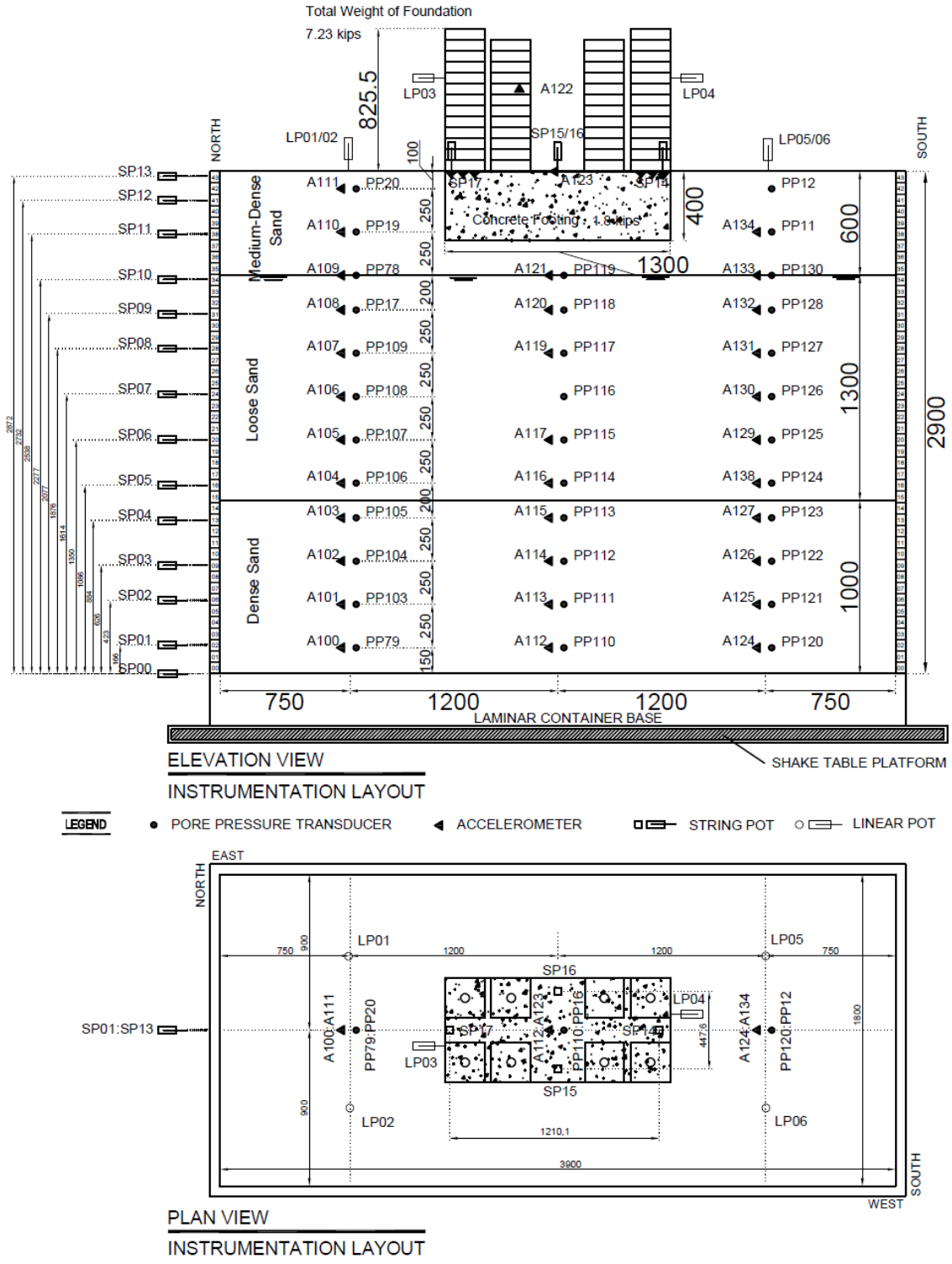

Figure 2.3 **Elevation and plan view of instrumentation layout for Baseline test (all units are in mm). Three arrays of accelerometers and pore water pressure sensors were installed, two at free-field (north and south) and one under the foundation.**

2.2.2 System Identification

A number of high-resolution accelerometers (PCB333B50, PCB PIEZOTRONICS, Depew, NY, USA) were installed in the model ground in the form of arrays to measure the shear-wave velocity profile before the shaking sequences. These accelerometers have a broadband resolution of 0.00005 m/sec^2 root-mean-square (RMS) amplitude, with a frequency range from 0.5 to 3,000 Hz. A total of 28 high-resolution accelerometers were installed in two different arrays to capture the travelling shear waves in the form of acceleration time histories during white-noise shakings prior to the main shaking. Figure 2.4 presents the configuration of the high-resolution accelerometers used in the Baseline test. The frequency of data acquisition for these accelerometers was 25,600 Hz, facilitating the observation of arrival time and time difference between two consecutive sensors which, in turn, resulted in a shear-wave velocity profile with depth.

To capture the predominant frequency of the soil model before each strong shaking, white-noise motion was applied for 6 sec with an amplitude of 0.05*g* and frequency between 5 to 20 Hz. The Fourier amplitude spectra and the resulting transfer functions are presented in Figures 2.5 and 2.6 for the white-noise shake before the main Shake 1-1. The predominant frequency (first mode) of the soil model based on these results ranges from 4.78 to 5.10 Hz (0.21 to 0.19 sec).

The shear-wave velocity profile for the constructed ground model was calculated based on the white-noise motion arrival time and the time difference between two consecutive high-resolution accelerometers. Figure 2.7 illustrates the shear-wave velocity profile for the soil model measured before Shake 1-1. The results of the shear-wave velocity calculation are also tabulated in Table 2.5. The depth of each sensor is measured from surface, and the distance between sensors is depicted in Figure 2.4, ranging between 0.2 to 0.25 m. The shear-wave velocity profile indicates higher shear-wave velocities in the dense layer compared to the loose and crust layer.

Table 2.5 Measured shear-wave velocity profile along depth of model ground before Shake 1-1.

Depth (m)	Arrival Time (s)	V_s (m/s)	Layer
0.1	7.5882	56.8	Crust
0.35	7.5838	62.5	Crust
0.60	7.5798	83.3	Crust
0.80	7.5774	82	Liquefiable
1.3	7.5713	100	Liquefiable
1.55	7.5688	92.6	Liquefiable
1.8	7.5661	134.6	Dense
2.25	7.5625	156.25	Dense

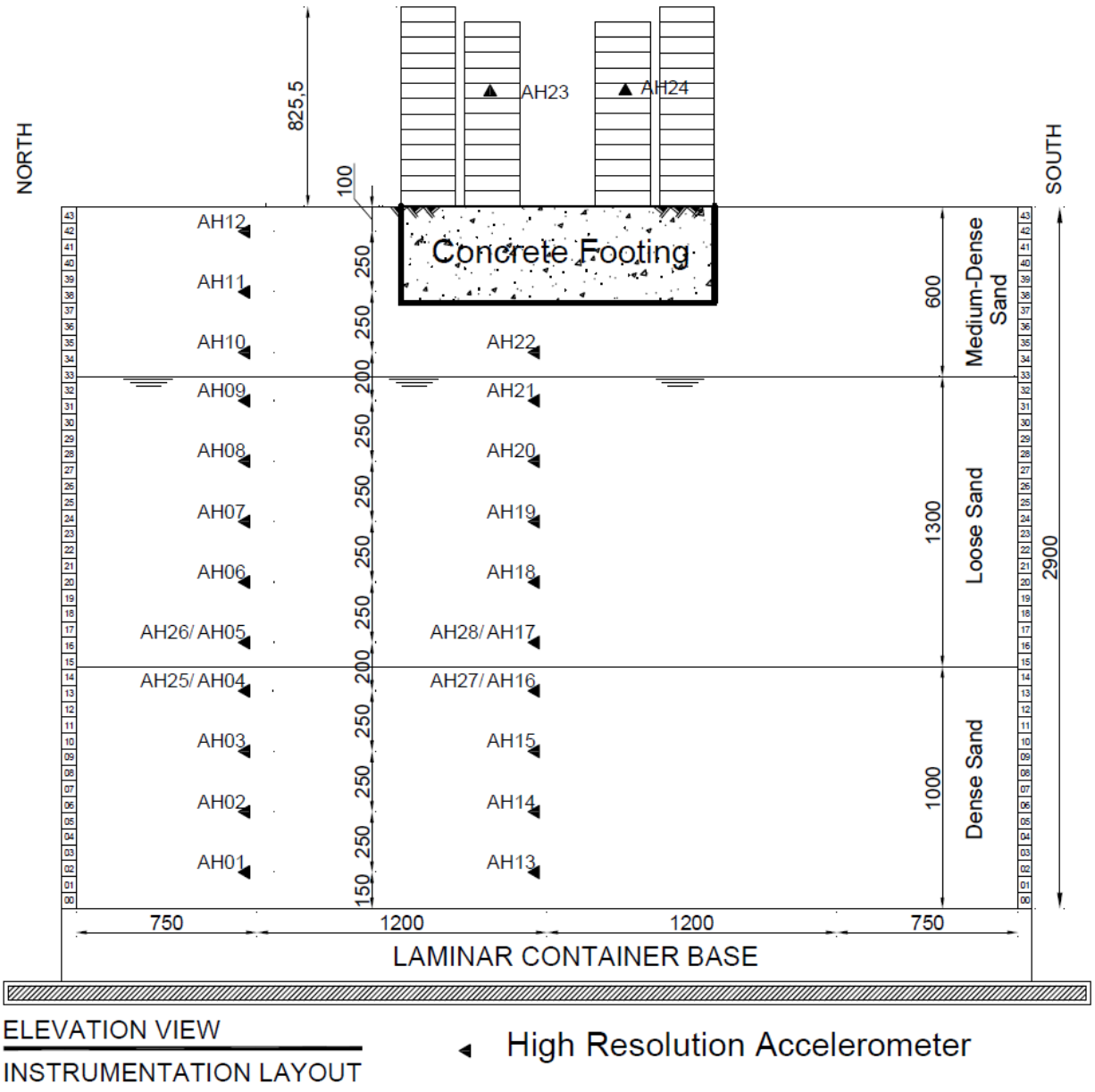

Figure 2.4 **Instrumentation layout for high-resolution accelerometers (all units are in mm). Two arrays of accelerometers were installed, one at the free field (north) and one beneath the foundation.**

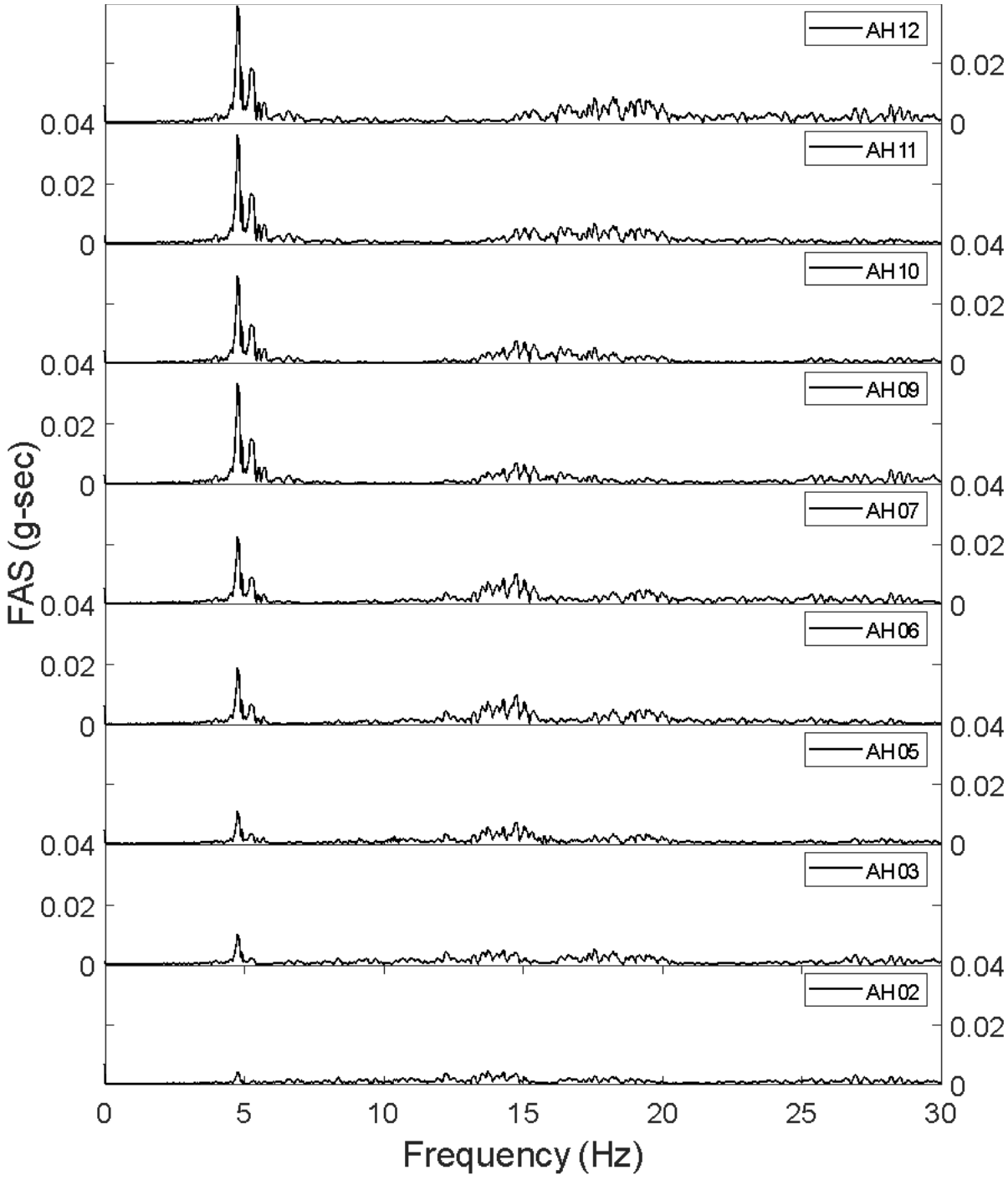

Figure 2.5 **Fourier amplitude spectra based on high-resolution accelerometer data (free-field array) prior to Shake 1-1.**

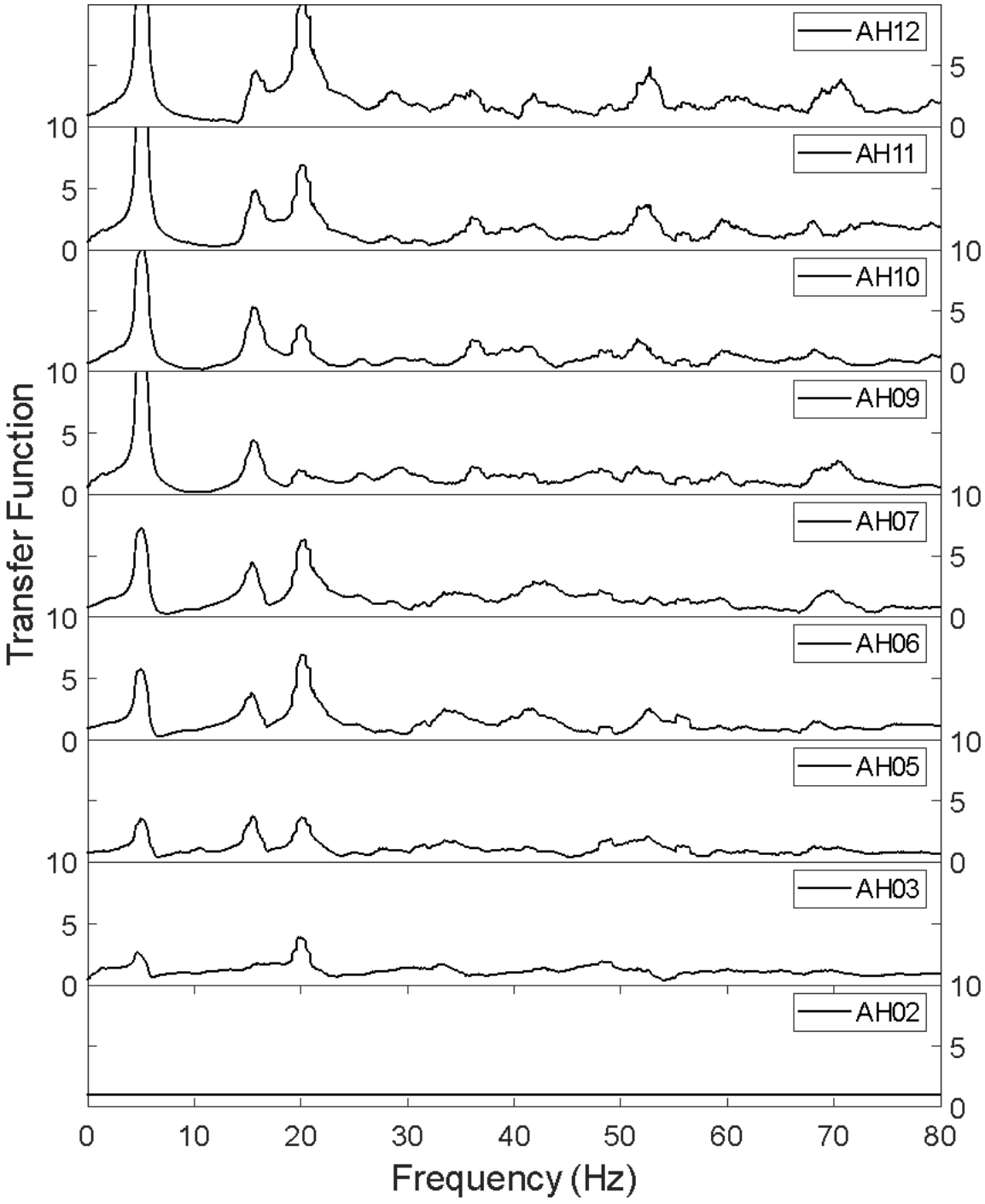

Figure 2.6 **Transfer functions based on high-resolution accelerometer data (free-field array) prior to Shake 1-1.**

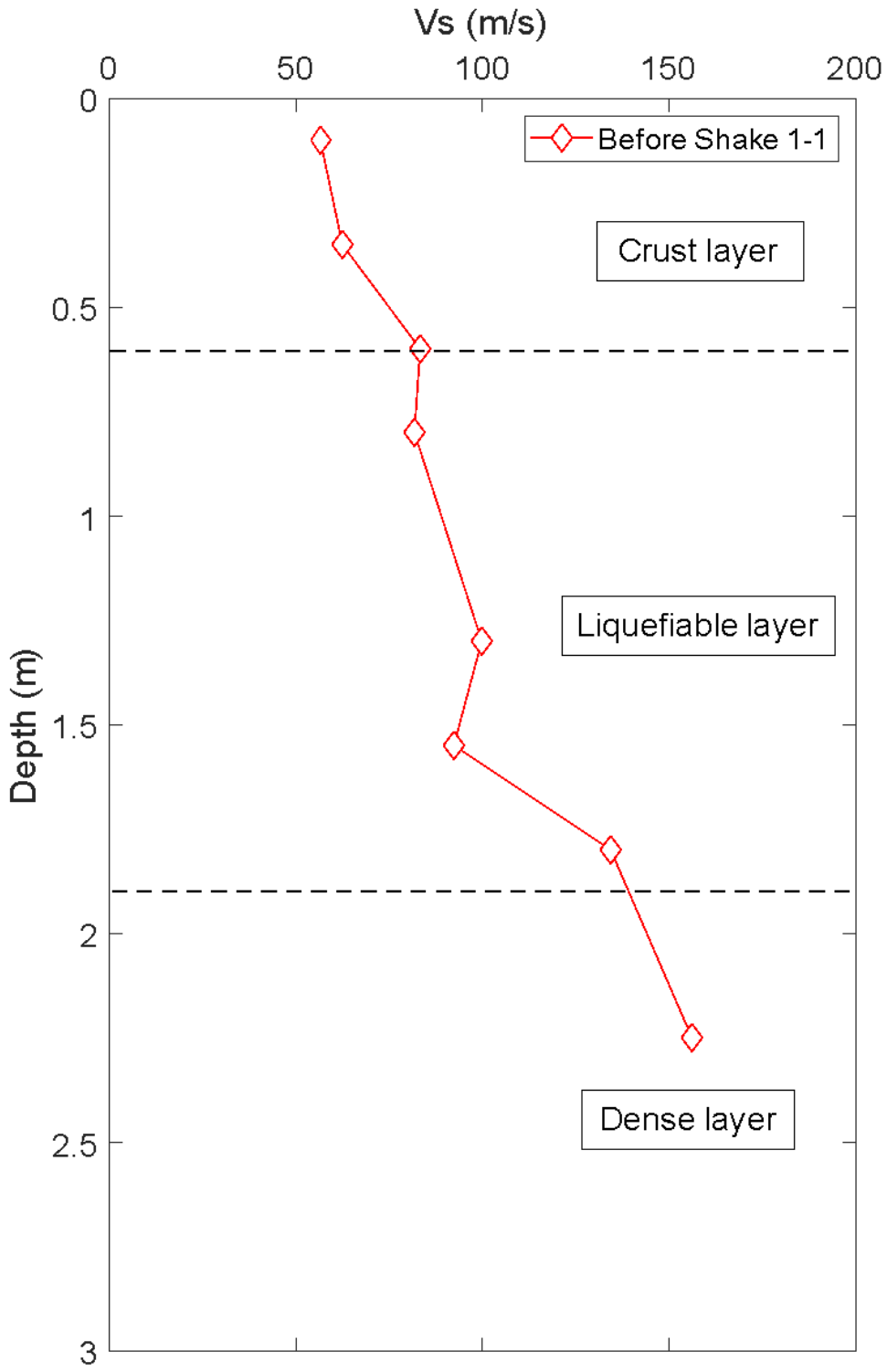

Figure 2.7 **Shear-wave velocity profile along depth of the soil model before Shake 1-1 in Baseline test.**

2.2.3 Shaking Sequences

During testing, a series of input motions were used to assess the dynamic response of shallow foundation along with free-field ground model for this baseline test. As mentioned earlier in Section 2.2, these two shaking sequences had different peak accelerations but with the same duration and frequency. Sufficient time was allowed between these two shakings for the generated pore-water pressure to dissipate. The acceleration response spectra for Shake 1-1 are presented in Figure 2.8, including response spectra for the base motion, foundation, and free-field surface ground motions. The predominant period of the input motion is shown to be 0.5 sec, and the spectral acceleration of the foundation and surface free field were de-amplified due to the 1.3 m liquefiable layer, resulting in lower responses of the foundation and the surrounding ground surface.

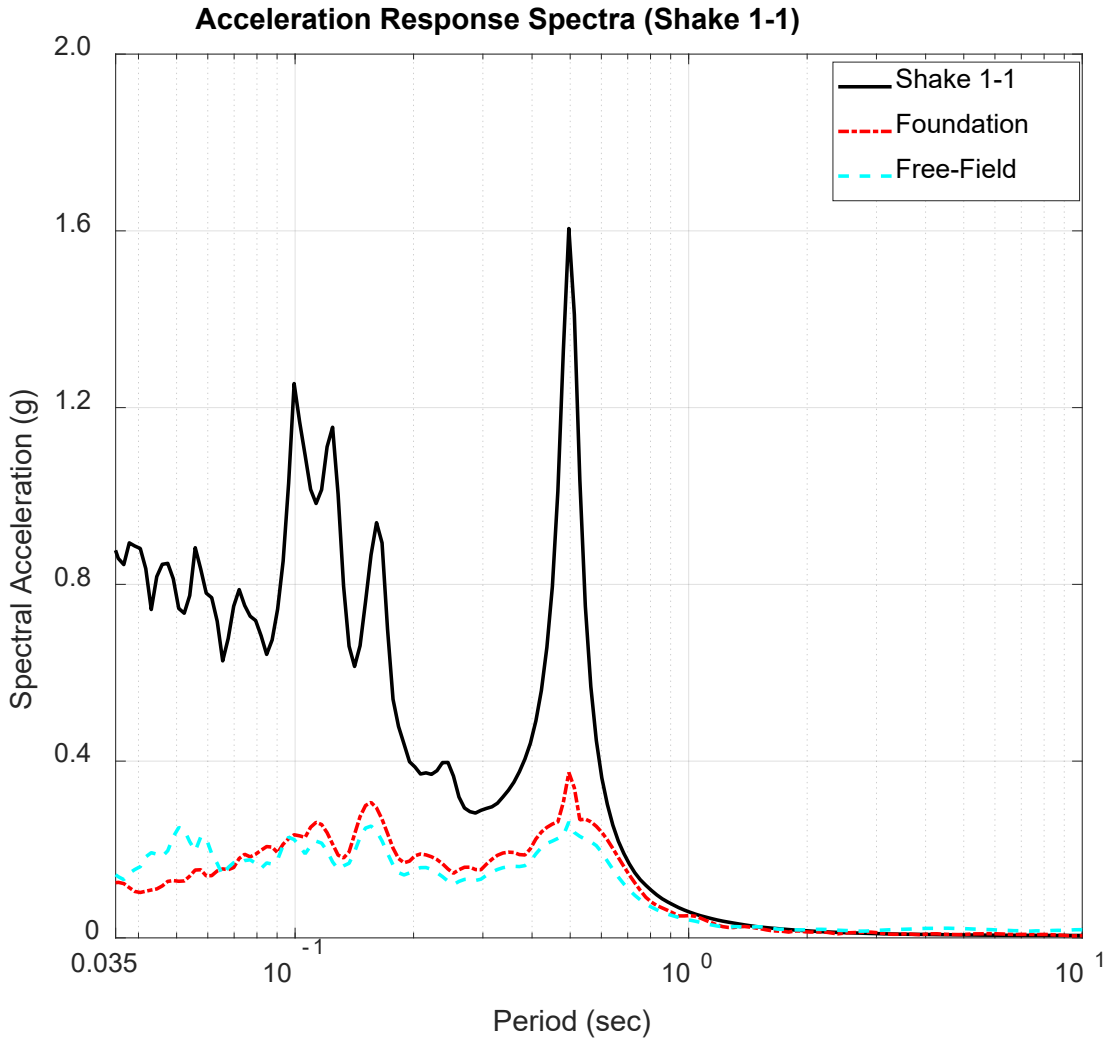

Figure 2.8 Acceleration response spectra (5% damped) for Shake 1-1.

2.3 HELICAL PILE TEST SERIES

This section provides the details of the shake table experimental program mainly for the Helical Pile tests. Additionally, the combined summary of shaking sequences, input motion properties, and number of instrumentation for both Baseline and Helical Pile tests are provided below.

2.3.1 Shake Table Experimental Program

Each test series comprised of two shakings: "Shake 1" and "Shake 2." The main characteristics of the table motion during each shaking are summarized in Table 2.6. Both test series featured fairly comparable table motion characteristics, although there were minor differences observed in some of the parameters. The acceleration time histories of the table motions in both shakings are presented in Figure 2.9. The test series were performed in a displacement-controlled setup, with a target input displacement history provided to the shake table controller. The achieved input acceleration time histories for Shake 1 and Shake 2 were obtained through unfiltered recordings from double integration of displacement time histories recorded by a string potentiometer connected to base of the laminar container. As shown in Figure 2.9, the shaking scheme for both tests included 6 sec of ramp up, followed by 6 sec of uniform motion with a constant amplitude that ceased through 3 sec of motion tapering down (total of 15 sec). The input motions for both Shake 1 and Shake 2 were applied at a constant frequency of 2 Hz, with the peak acceleration ranging from 0.53*g* to 0.66*g*. Details about ground-motion selection and soil-box specifications can be found in Jahed Orang et al. [2021a].

Table 2.6 Ground motion parameters for Baseline and Helical Pile test series.

Parameters	Baseline		Helical Pile	
	Shake 1	Shake 2	Shake 1	Shake 2
Achieved peak acceleration (*g*)	0.53	0.66	0.57	0.55
Arias intensity, I_a (m/sec)	3.42	9.21	4.47	9.19
Significant duration, $D_{5\text{-}95}$ (sec)	10.10	9.74	10.08	11.31
Peak Ground Velocity, PGV (cm/sec)*	121.05	121.43	42.91	52.21
Cumulative Absolute Velocity, CAV (*g*.sec)*	1.35	2.36	1.51	2.38

*For 25 sec of recorded data.

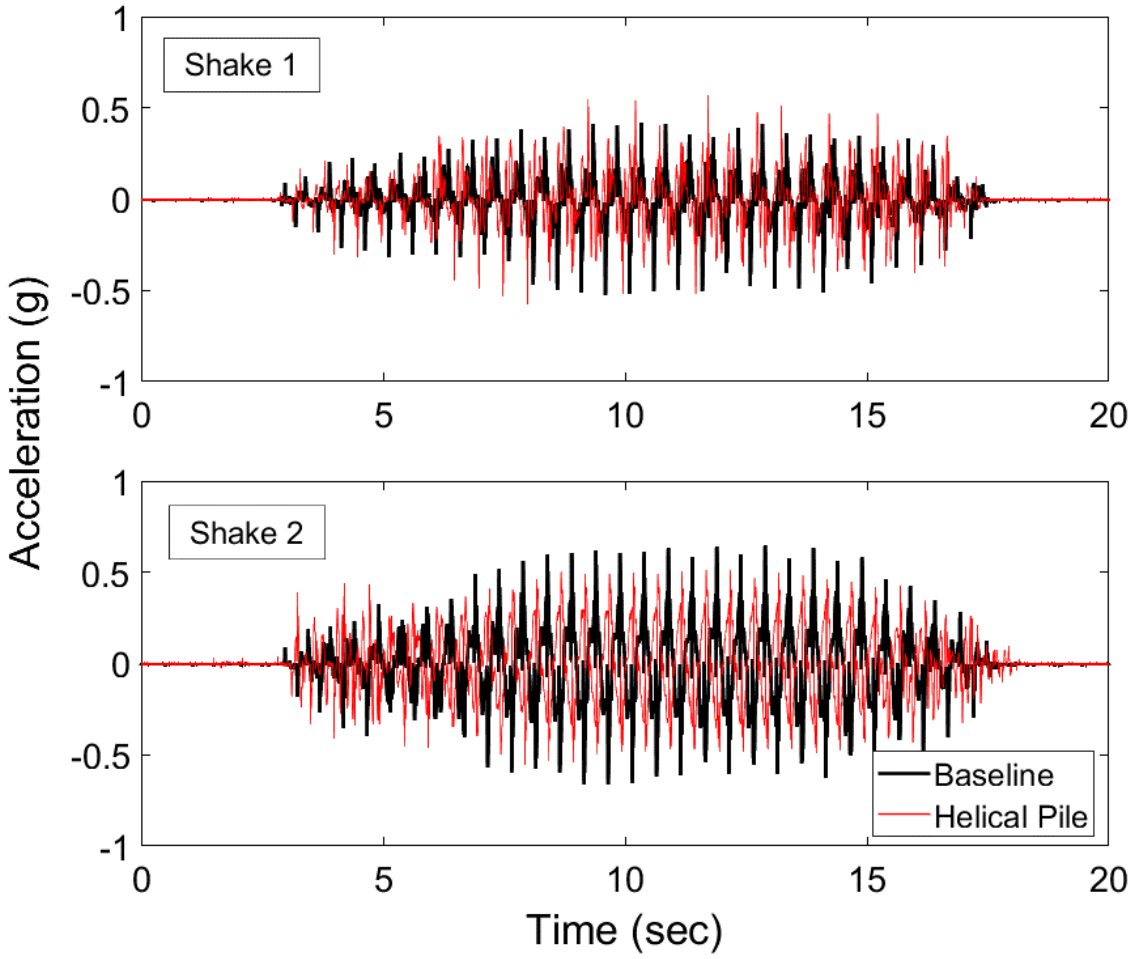

Figure 2.9 **Acceleration time histories for both shakes during Baseline and Helical Pile tests.**

Figure 2.10 presents the isometric view of Helical Pile test before Shake 1. The 2.9-m-tall laminar box was used to contain the sand and structural components inside and on top of the sandy soil medium. A total of six cameras were used to videotape all the shakings from different angles to capture the soil–foundation response. More details about ground-model preparation and instrumentation, helical-pile specification, protection and instrumentation, and further ground-model identification were provided in the following sections. Note: the details of Baseline test series and discussions on the controlling mechanisms of shallow foundation response on top of a liquefiable soil layer is presented in Jahed Orang et al. [2021a]; this paper presents the Helical Pile test series mainly focusing on the response of helical piles and their performance in liquefied soils.

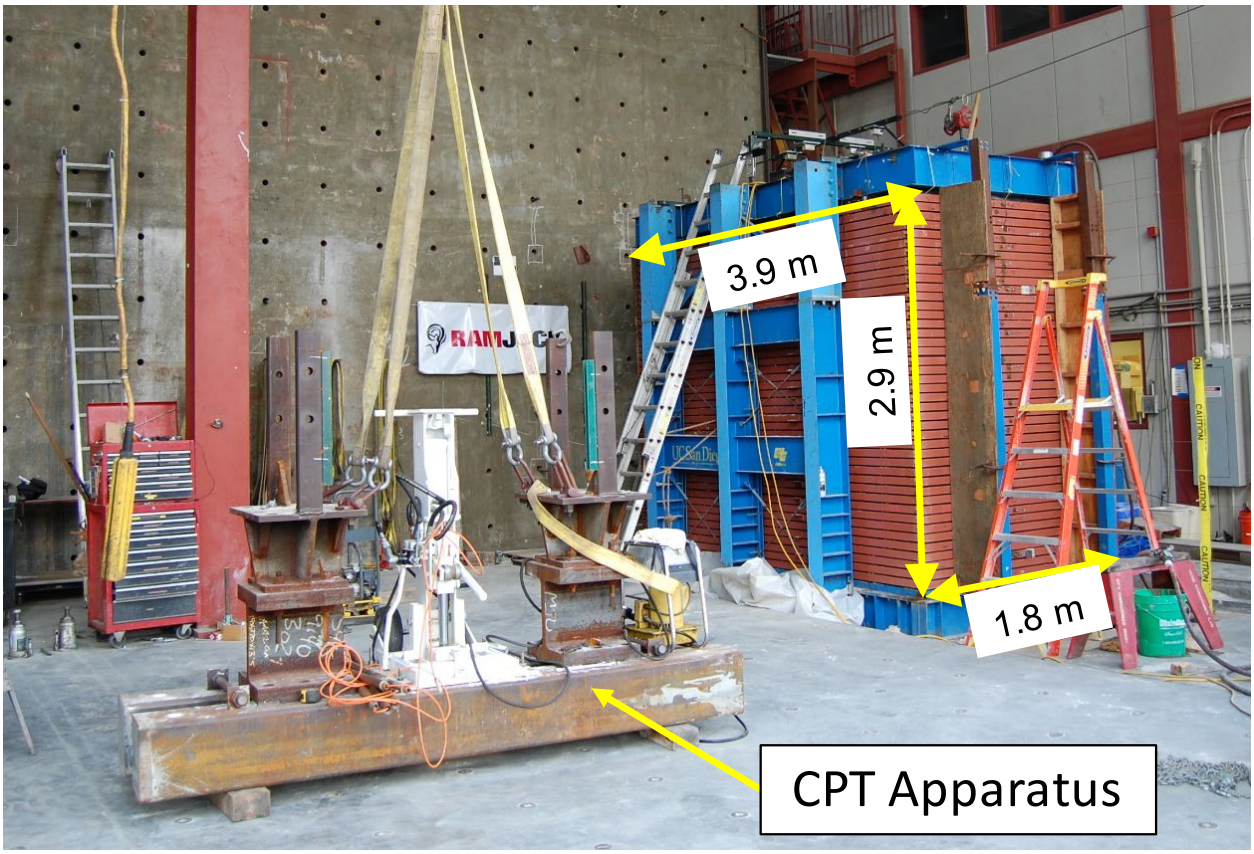

Figure 2.10 Isometric view of Helical Pile test before Shake 1.

2.3.2 Model Ground Preparation and Instrumentation

Ottawa F-65 sand was used to build a three-layer ground model including dense, loose, and crust layers in both test series (i.e., Baseline and Helical Pile tests). The geotechnical properties of Ottawa F-65 sand can be found in Bastidas [2016]. The thickness of dense, loose, and crust layers were 1.0, 1.3, and 0.6 m, respectively. The bottom layer was constructed as a dense-sand medium, overlain by loose-sand deposit. Finally, a top crust layer was constructed to place the shallow foundation. The ground water level was located at the top of the liquefiable layer (i.e., 0.6 m below ground level). The achieved relative densities for dense, loose, and crust layers were in the range of 85–90%, 40–45%, and 50–55%, respectively. Details regarding the construction method and achieved relative densities for each layer can be found in Jahed Orang et al. [2021a]. The model ground for both Baseline and Helical Pile test series was constructed in similar conditions. Four instrumented single-helix helical piles were tied to the shallow foundation in the Helical Pile test to examine the efficacy of these deep-foundation elements in mitigating liquefaction-induced settlements in shallow foundations. Details of instrumentation, strain gauge protection, and helical pile installation will be discussed in Section 2.3.3.

The shallow foundation embedded in the crust layer was 1.3 m in length, 0.6 m in width, and 0.4 m in depth. The 23 kg single weights stacked in six rows added a 3280 kg load on top of

the shallow foundation; see Figure 2.11. The final foundation contact pressure was about 41.6 kPa, which replicated the contact pressure of a two-to-four story building.

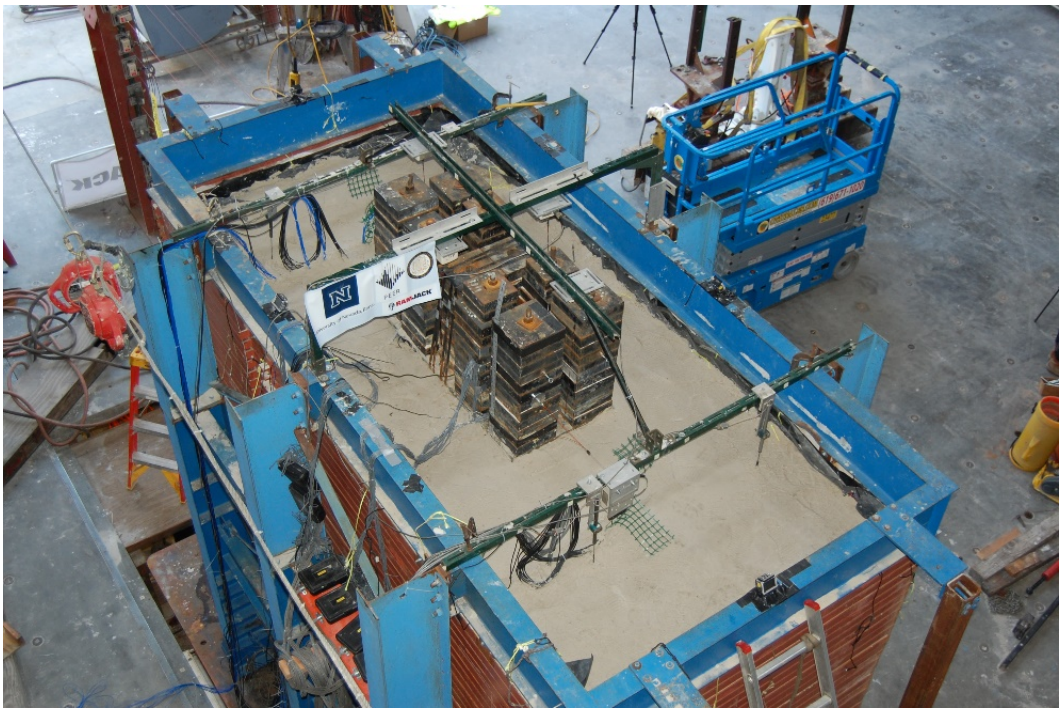

Figure 2.11 Model shallow foundation and superstructure weights in Helical Pile test.

2.3.2.1 Ground-Model Instrumentation

Various instruments were utilized to capture the seismic response of the soil–pile–foundation-superstructure system. A breakdown of the instrumentation used in Baseline and Helical Pile test series are provided in Table 2.7. A total of 150 sensors were used in Helical Pile test series. The instrumentation layout for Helical Pile tests is presented in Figure 2.12. A similar instrumentation plan was used in both test series except the strain gauges, which were only used on four helical piles to examine their dynamic response in the Helical Pile tests.

As illustrated in Figure 2.12, three arrays of pore-water pressure sensors and accelerometers were installed to capture the ground-model response. A total of 14 string potentiometers were used to capture the lateral displacement of the laminar box. The foundation and near-foundation settlements were measured using four string and four linear potentiometers located at four corners of the foundation and the ground model, respectively. Seven pairs of strain gauges were attached to each helical pile. Two pairs of these strain gauges were located in the dense medium, where the rest were located within the liquefiable layer. The location and spacing of the strain gauges (Figure 2.12) were designated based on pile length, type and dimensions of strain gauge protective measures, length of the helical pile guide sleeve, and depth of the loose-dense layer interface.

Table 2.7 **Types and number of instrumentation used in Baseline and Helical Pile tests.**

	Test	
Type	**Baseline**	**Helical pile**
Accelerometer	35	14
PCB accelerometer	28	24
Pore-water pressure sensor	47	33
String potentiometer	18	19
Linear potentiometer	6	4
Strain gauge	-	56
Total	134	150

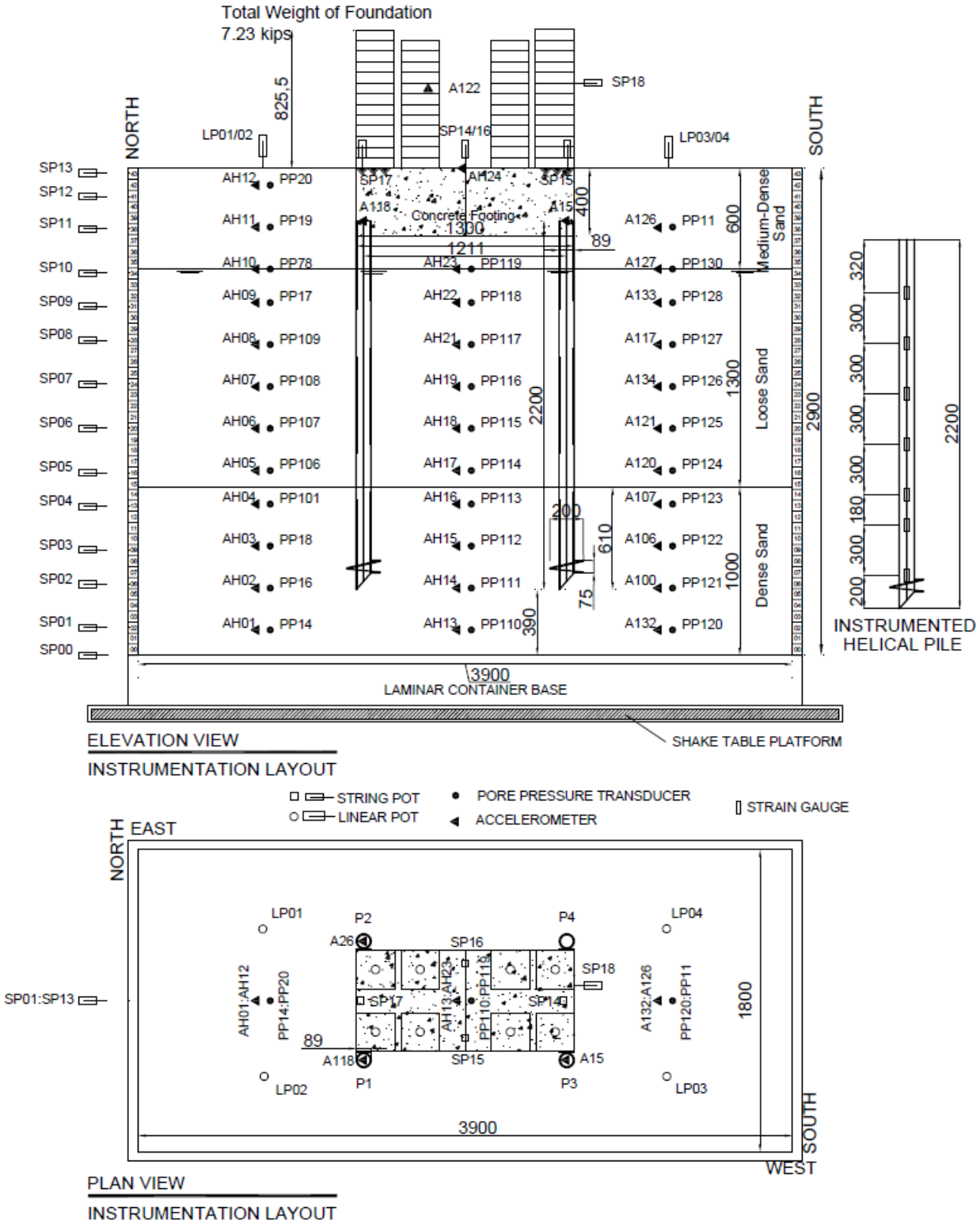

Figure 2.12 **Elevation and plan view of instrumentation layout for Helical Pile test (all dimensions are in millimeters).**

2.3.3 Helical Piles Specifications and Instrumentation

A total of four single-helix helical piles were used in the second test series; see Figure 2.13(a). Each of the helical piles was connected to the shallow foundation using 4021.1 side brackets; see Figure 2.13(c). Each side bracket was pinned to the foundation using two 1.6-cm anchor bolts; see Figure 2.13(b). A total of four 4021.1 side brackets with the allowable compression capacity of 162.5 kN and eight 1.6-cm anchor bolts were used in the Helical Pile tests to connect the piles to the shallow foundation. Details and specifications regarding the helical pile properties are provided in Table 2.8. More information regarding the mechanical properties of the helical piles and side brackets can be found in the ICC-ES evaluation report [ESR-1854 Ram Jack 2017]). Note: although there are no specific seismic design guidelines for using side brackets in the International Building Code (IBC), the designated side brackets performed reasonably well under specific ground motion applied in these shake table tests.

Figure 2.13 **Photo of (a) single-helix helical piles, (b) bolts and nuts, and (c) side bracket used in Helical Pile tests.**

Table 2.8 Helical pile properties and specifications.

Property	Value (cm)
Helix pitch	7.5
Helix level below ground	240.0
Penetration into dense layer	61.0
Longitudinal pile to pile spacing	121.0 (13.50*D*)
Transverse pile to pile spacing	69.0 (7.75*D*)
Outside diameter	8.9
Wall thickness	0.5
Shaft length	220.0
Helix diameter	20.0

In the Baseline test series, the allowable static bearing capacity of the shallow foundation was calculated, yielding a *FS* greater than three; however, the foundation underwent excessive settlement (during and after first shake), constituting an unsatisfactory performance [Jahed Orang et al. 2021a]. Underpinning the shallow foundation with four helical piles was expected to increase the bearing capacity and decrease the settlement, achieving an acceptable foundation performance under static and dynamic loading.

The bearing capacity of the helical piles was calculated using the individual bearing capacity method [Perko 2009]:

$$Q_H = \sum A\left(cN_c + q'N_q + \frac{1}{2}\gamma N_\gamma \right) \tag{2.1}$$

where N_c, N_q, and N_γ are bearing capacity factors; c is soil cohesion; q' is effective overburden pressure at the bearing depth; γ is the soil unit weight, and A is the area of the helical bearing plate. The following assumptions were made in the allowable bearing capacity calculation of the helical piles:

- N_q was obtained from Hansen and Vesic bearing capacity factors [Vesic 1973]).
- The friction angle of the dense sand was assumed to be 35° ($\phi = 35^\circ$).
- The effect of liquefiable layer weight was neglected in effective overburden pressure calculation.
- The factor of safety was assumed to be two (*F.S.* = 2) for each helical pile.

Based on Equation (2.1), the allowable capacity of each helical pile was calculated to be 16.7 kN. The pile group capacity, assuming a group efficiency of 1, was 66.8 kN. The calculated group capacity was almost twice the load exerted on the ground model through both shakes (the total load exerted to the ground model was 32.5 kN). The bearing capacity of the helical piles can be verified through torque measurements during helical pile installation, as the measured torque correlates to the ultimate bearing capacity of the helical pile. During the helical pile installation in this study, the measured torque was affected due to the presence of a shallow liquefiable layer and

relatively low thickness of the ground model compared to real site conditions. The maximum measured torque was about 0.68 kN.m, resulting in the 15.5 kN ultimate bearing capacity of a single helical pile, which was close to the estimated theoretical capacity. The calculated bearing capacity of the helical piles was further justified after both shakings, where there was no observed foundation bearing capacity failure due to the dynamic loading.

A total of 56 strain gauges (FLA 5-11-5LJC, Tokyo Sokki Kenyujo Co., Ltd) were attached to the helical piles to measure bending strain at different depths. Seven pairs of strain gauges were bonded on each helical pile at designated depths; see Figure 2.12. All strain gauges were connected in full-bridge configuration into the data acquisition system (DAQ). Various measures were adopted to protect the strain gauges from any damage during the helical pile installation. Figure 2.14 illustrates the protective measures taken to avoid damage in the strain gauges during installation. First, the area around each strain gauge location was welded in a U shape; see Figure 2.14(a). This measure can reduce the abrasion of the strain gauges during installation. Second, all the strain gauges were guided through the 2-cm holes [Figure 2.14(b)] drilled on the side of each helical pile at designated depths. These holes were used to guide strain gauge wires through the inner hollow part of the helical piles. All the strain gauges were set in place before applying the adhesive material; see Figure 2.14(c). Third, acrylic glue was applied on top of each strain gauge, followed by a mastic tape cover for further protection; see Figures 2.14(d) and 2.14(e). Finally, wide aluminum wraps were rolled around the periphery of the designated area to further protect the strain gauges; see Figure 2.14(f). These protective measures ensured that a high percentage of strain gauges functioned during the Helical Pile tests, with 22 out of 28 pairs measuring quality data. The protection procedure was based on information provided by Professor Amy Cerato of the University of Oklahoma, who used similar precaution procedures during a series of large-scale shake table tests on helical piles in 2015 [Cerato 2019].

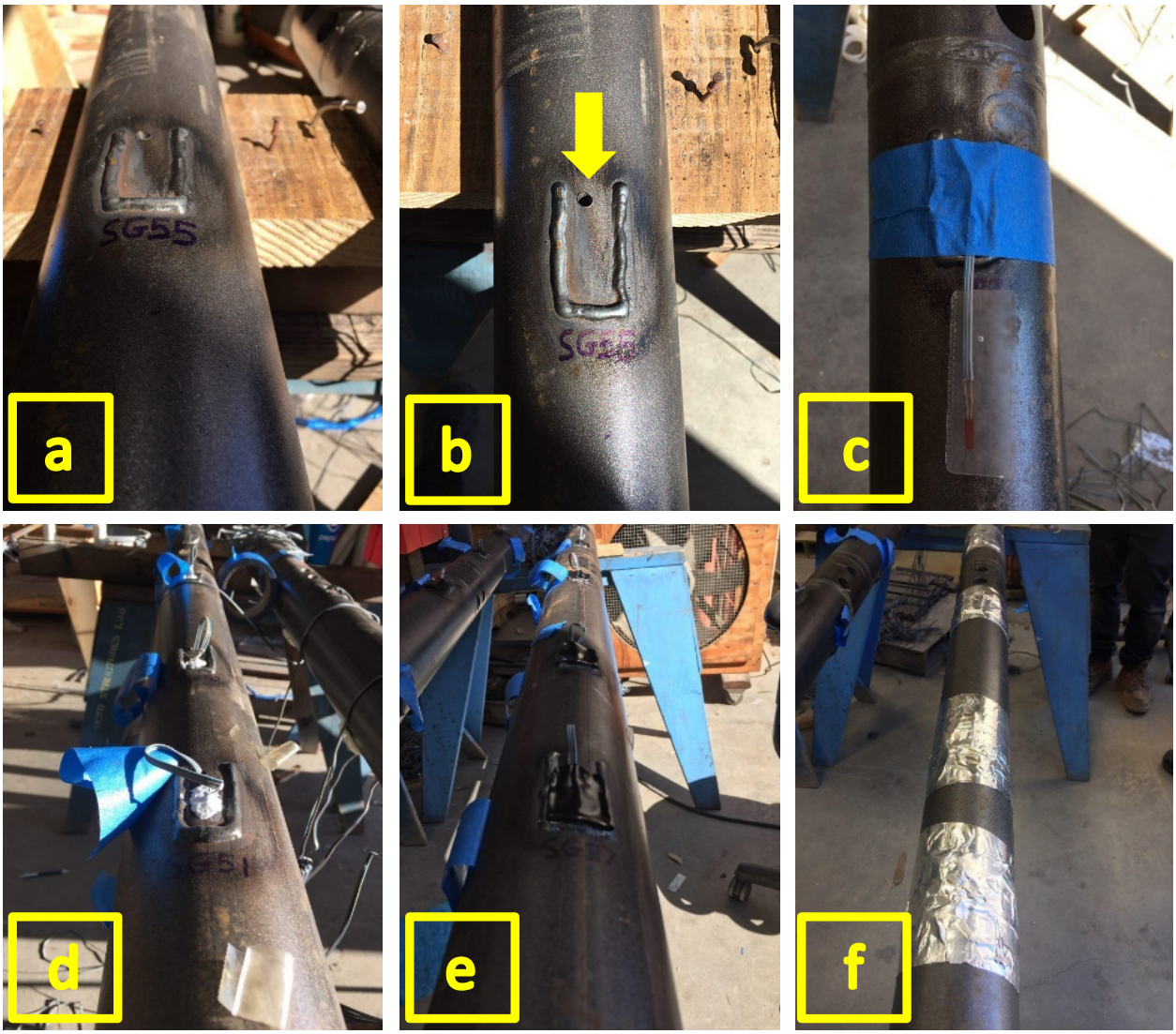

Figure 2.14 Strain gauge installation and protection measures.

2.3.4 CPT and Shear-Wave Velocity Measurements

The cone penetration test (CPT) was used to characterize the model soil profile before and after Shake 1 during the Helical Pile tests. Figure 2.10 illustrates the CPT apparatus used for this purpose. Two CPT soundings were obtained at each stage on the northern and southern sections of the soil box. The CPT test provided better realization of the variations in relative density of different layers, which helped to evaluate the ground model before and after each shake.

Figure 2.15 presents the measured tip resistance (q_c) along the depth of the ground model for the Helical Pile test series, along with the measured shear-wave velocity (V_s) profile for the Baseline test series; PCB accelerometers were used to screen the peak-to-peak wave arrival time between two consecutive PCB accelerometers. Further details regarding the shear-wave velocity measurements are provided in Jahed Orang et al. [2021a]. Both the tip resistance and shear-wave

velocity measurements before Shake 1 show an increasing trend with the increase in depth. The measured tip resistance along depth both in the northern and southern section of the ground model display increased resistance after Shake 1, especially at the dense-liquefiable layer interface (i.e., the bottom half of liquefiable and top one-third of the dense layer), indicative of increased relative density (D_r) after Shake 1; see Figure 2.15(b).

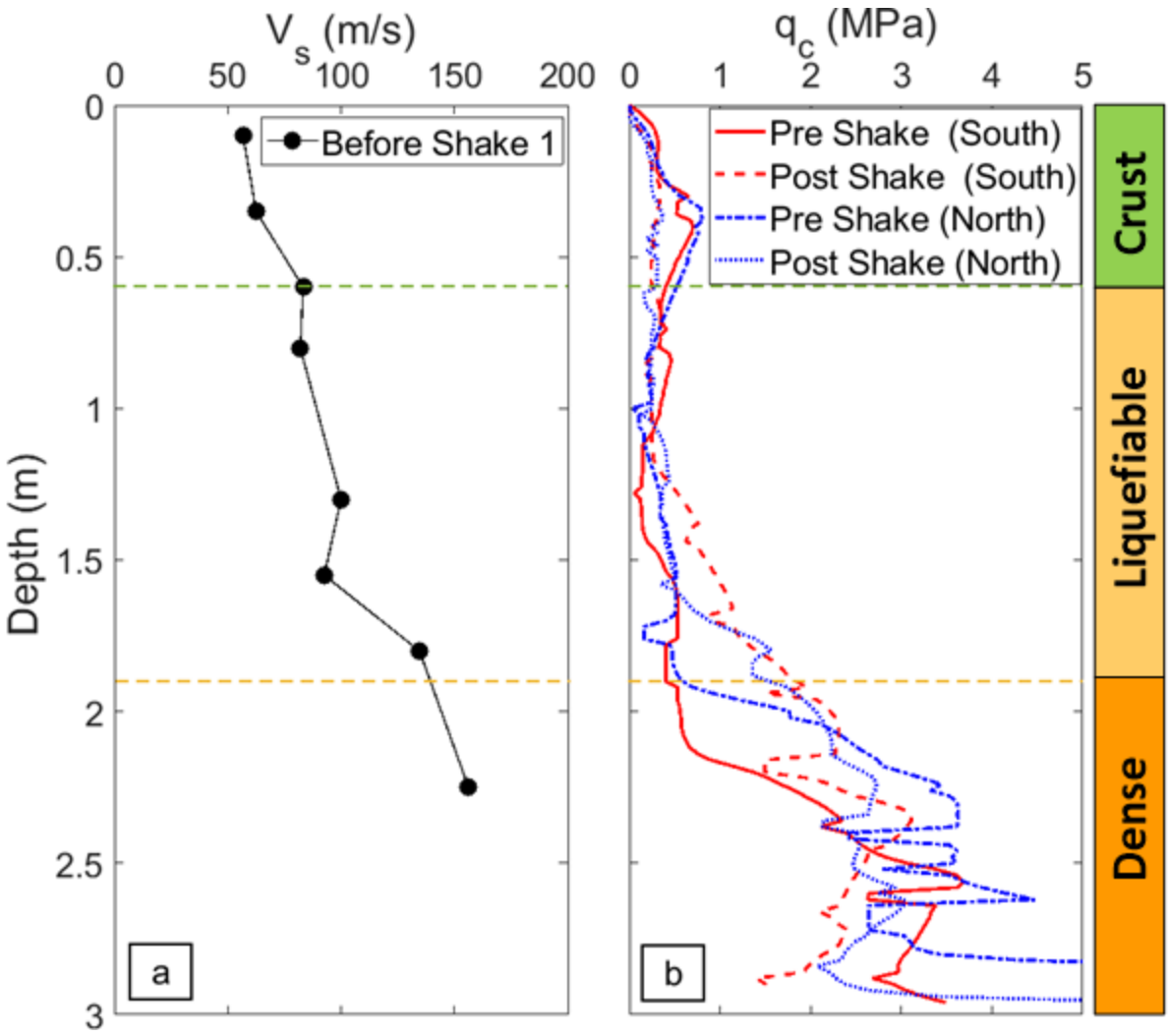

Figure 2.15 **(a) Shear-wave velocity (V_s) profile before Shake 1; and (b) cone penetration resistance (q_c) along depth before and after Shake 1.**

3 Experimental Results

3.1 BASELINE TEST SERIES

The experimental results for Baseline test series are provided in this section.

3.1.1 Experimental Results

The 1*g* shake table testing at this scale provides an opportunity to further investigate the behavior of shallow foundation systems located on ground with surficial liquefiable layers that have been observed in several past earthquakes without the need to worry about scaling and its effect on the results. The results of excess pore-water pressure (EPWP) generation due to liquefaction in different layers is thoroughly evaluated followed by relevant discussion on hydraulic gradient and its effect on observed sand ejecta. The effect of damage potential cumulative absolute velocity (CAV_{dp}) as an intensity measure (IM) is also discussed in the following section. Finally, the observed settlement of the shallow foundation and free-field conditions during the two shaking sequences are also discussed. Note: the results of Shake 1-1 comprise the bulk of the presentation, while the results from Shake 1-2 are included in the summary tables and figures.

Figure 3.1 shows the subset of sensors used in "Baseline Test" to display representative results such as acceleration, excess pore-water pressure, and settlement time histories. As shown in Figure 2.3, three arrays of accelerometers and pore-pressure transducers were embedded in the model ground; however, only two arrays—the "free field" and "below foundation"—were selected to be presented; see Figure 3.1. The soil surrounding the foundation at 0.6 m from edge of the foundation on each side is referred to as "free-field" condition per the Baseline Test as discussed earlier. Two pairs of sensors in the middle of dense layer were selected to illustrate acceleration and pore-water pressure results for that layer. Example sensors at the bottom, middle, and top of the loose layer identified as "bottom of liq. layer", "mid. of liq. layer" and "top of liq. layer," were selected for results pertaining to the loose layer.

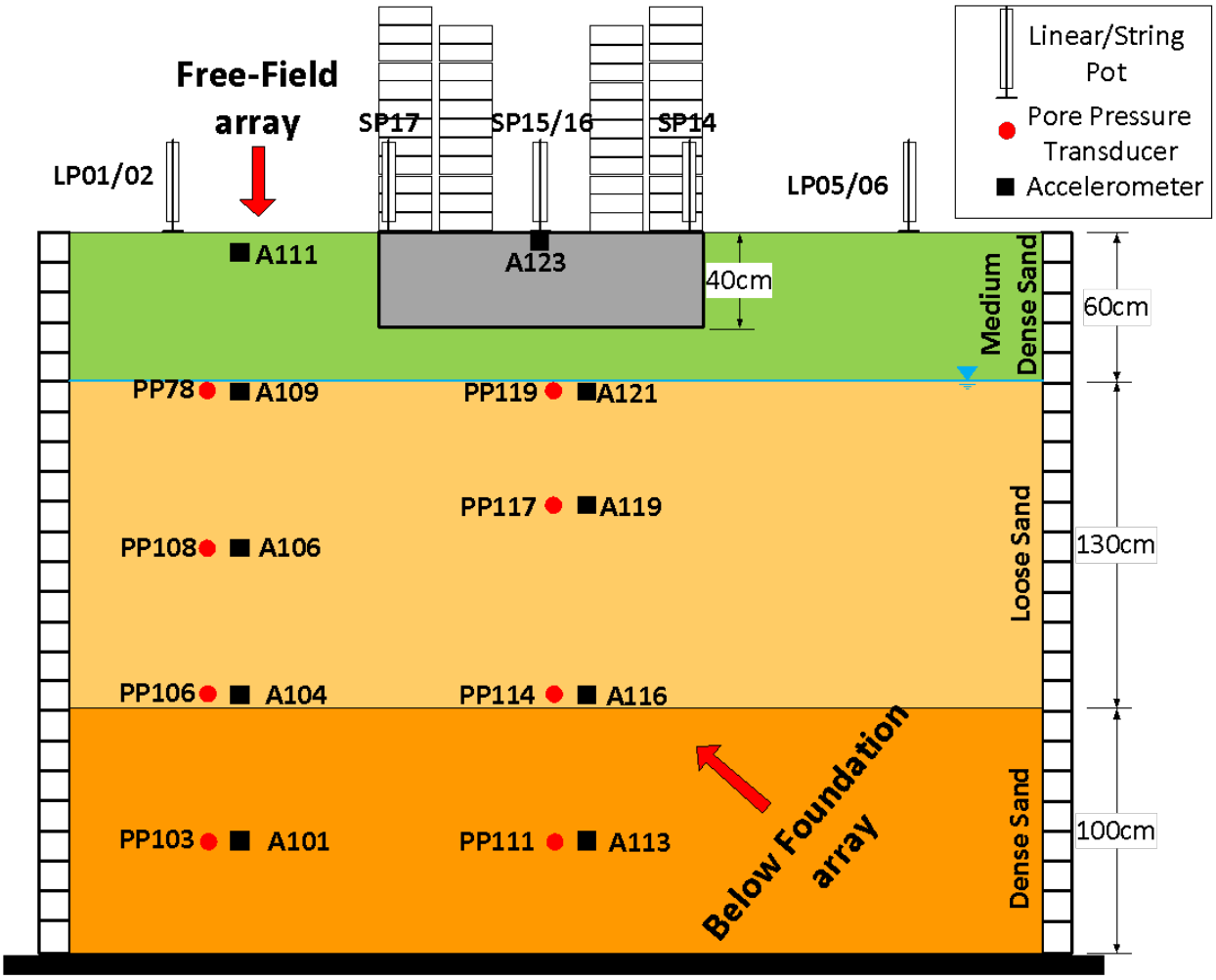

Figure 3.1 **Cross-section view of sensors used for data processing in Baseline test.**

3.1.2 Excess Pore-Water Pressure Generation

The liquefaction-induced settlement mechanisms introduced by Bray et al. [2014] highlighted the importance of pore-water pressure generation/dissipation, transient hydraulic gradients generated during strong shaking, and bearing capacity failure of shallow foundation due to strength reduction as contributing causes in different liquefaction-induced settlement mechanisms. As a result, extensive instrumentation of pore-water pressure transducers was used to monitor the generation and dissipation of excess pore-water pressure in the shake table tests discussed herein.

Figures 3.2 and 3.3 present the generated pore-water pressure and acceleration time histories at the free field and below the foundation arrays during Shake 1-1, respectively. The acceleration time histories were "as recorded" time histories without any filtering. These time histories are shown at different depths, which include bottom, top, and middle of liquefiable layer and also the middle of the dense layer. The dashed lines represent the case in which excess pore-water pressure ratio (r_u) corresponds to unity (i.e., 1.0) at different depths and locations. When

calculating the r_u values, the effect of vertical stress due to the foundation pressure was also incorporated using the 2:1 stress distribution method below the foundations. For the free-field case (Figure 3.2), the observed trend for excess pore-water pressure generation/dissipation is similar at bottom and middle of the liquefiable layer, where a drastic increase was observed in EPWP during strong shaking, which was then followed by a gradual dissipation of EPWP once shaking ceased. The rate of generation/dissipation is comparable in these depths.

In contrast, the observed EPWP trend in the upper part of the liquefiable layer and middle of the dense layer indicate a steady increase during the shaking that continued even after the shaking phase. This behavior was more pronounced in the middle of the dense layer. The reason for this progressive, though less significant, increase after the shaking could be due to the direction of pore-water pressure dissipation path at the bottom and middle of the liquefiable layer. The drainage paths created after the shaking most likely resulted in continuation of pore-water pressure buildup in the middle of dense layer and top of loose layer. This hypothesis is tested by the results presented in the next section. Results presented in Figure 3.2 show that the EPWP values reached the initial effective stress (dashed lines) in all three depths inside the liquefiable layer, indicating the occurrence of liquefaction. The pore-pressure ratio at the middle of the dense layer increased up to 0.4 as expected for a dense sandy medium; however, based on Bray and Macedo [2017], it is assumed that the dense saturated sandy soil still contributed to the liquefaction-induced settlement. The highest generated EPWP during Shake 1-1 is the same for free-field and below foundation arrays at the comparable depths, possibly due to the redistribution of EPWP and the proximity of the sensors.

The observations in the array under the foundation (Figure 3.3) were very similar to the free-field array presented in Figure 3.2 except for the fact that EPWP generation in the middle of liquefiable layer is not as steep as for the free-field array. This could be due to the added foundation pressure at top of the liquefiable layer, although the decreasing trend in EPWP just started after the ground shaking had ceased. The above discussion is also valid for the drainage paths, which resulted in a continued—although in a very insignificant manner—excess-pore pressure buildup at mid-dense and top liquefiable level below the foundation after the shaking had ceased. In addition, the r_u values (Figure 3.3, dashed lines) were lower than unity within the liquefiable layer under the foundation due to the added foundation pressure and its effect on the increased initial effective vertical stress. As illustrated in Figure 3.3, the r_u values were 1.5–2.0 times higher than their corresponding values in the free-field array; see Figure 3.2. The results for Shake 1-2 are not presented in this study for the case of acceleration and pore-water pressure time histories, but similar observations were obtained for Shake 1-2, which had a higher peak acceleration than Shake 1-1.

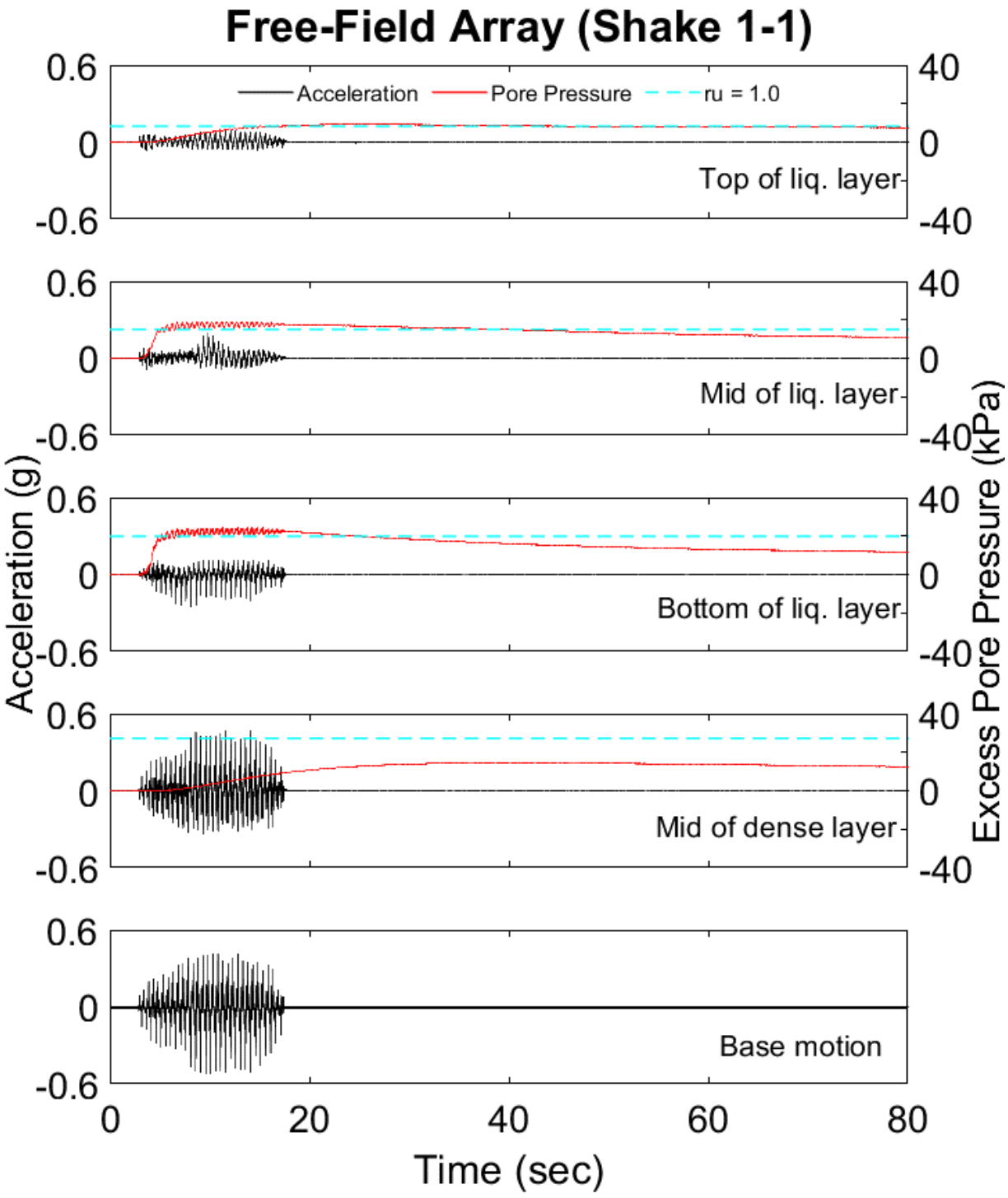

Figure 3.2 **Excess pore water pressure and acceleration time histories during Shake 1-1 at different depths in the free-field array (dashed lines indicating pore pressure ratio equal to 1 at different depths.).**

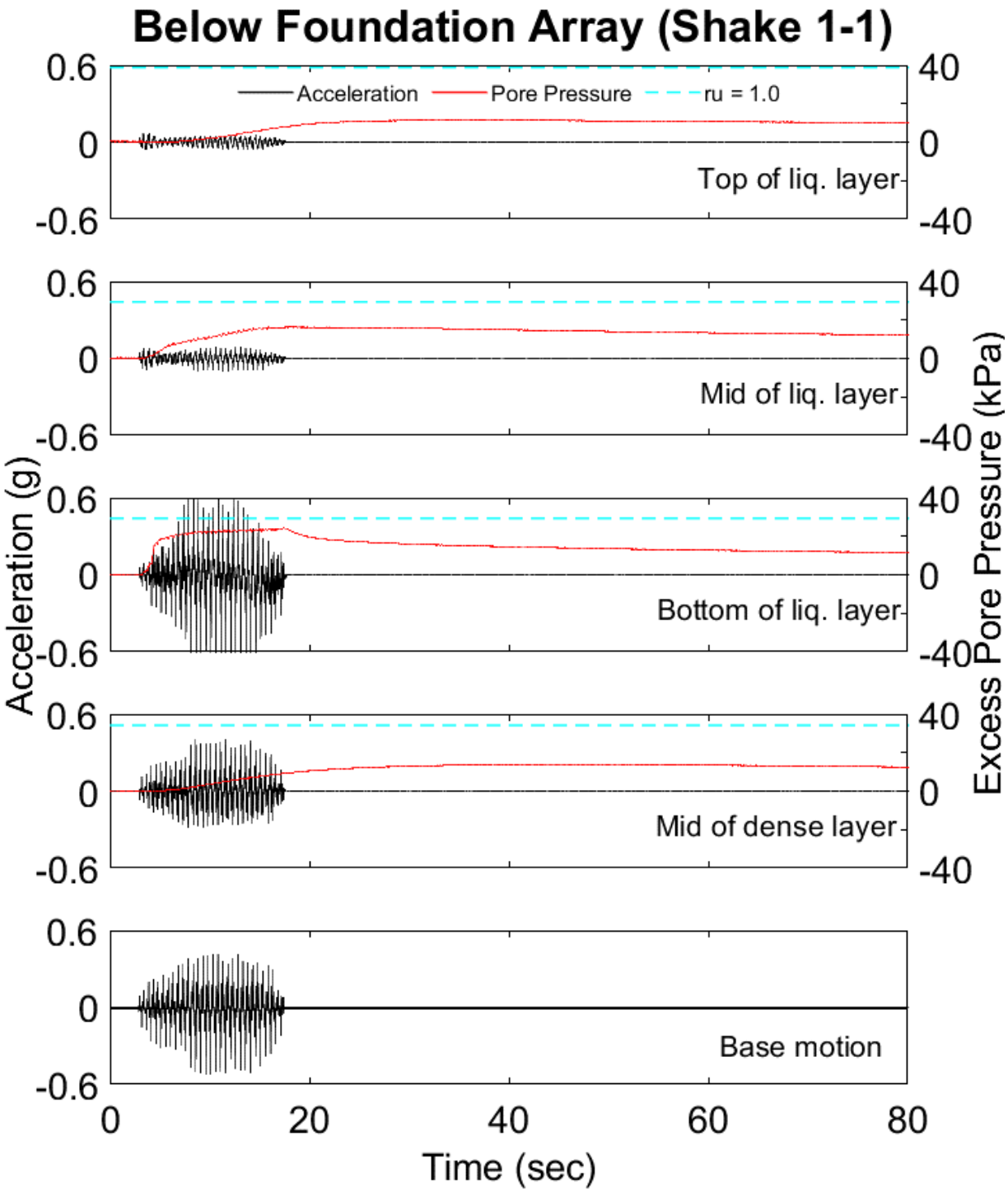

Figure 3.3 **Excess pore water pressure and acceleration time histories during Shake 1-1 at different depths below the foundation (dashed lines indicating pore pressure ratio equal to 1 at different depths).**

Example EPWP time histories are presented in Figures 3.2 and 3.3, while data from all other sensors were used to present the EPWP isochrones in Figure 3.4 for Shake 1-1 along depth of the soil model from 0.6 to 2.9 m (i.e., within liquefiable and dense layers). All of the pore-water pressure sensors in both arrays were used to generate these EPWP isochrones (a total of 20 pore pressure transducers). The observed trends of the isochrones provided some valuable insight into the generation and dissipation of EPWP data. As illustrated in Figure 3.4, the EPWP data in each depth inside the liquefiable layer seemed to increase during shaking (up to 20 sec) and followed a dissipative trend afterward. This trend was more profound at the bottom of the liquefiable layer. On the other hand, the EPWP isochrones inside the dense layer continued to increase even after the shaking had ceased (up to 50 sec). The pore-pressure dissipation within the dense layer initiated much later, after t = 50 sec, resulting in high pore-water pressure within the dense layer after the shaking had ceased (i.e., t = 20 sec). Another important observation based on Figure 3.4 was the stabilization of the EPWP starting from t = 50 sec yielding relatively uniform values along depth in both arrays after 50 sec.

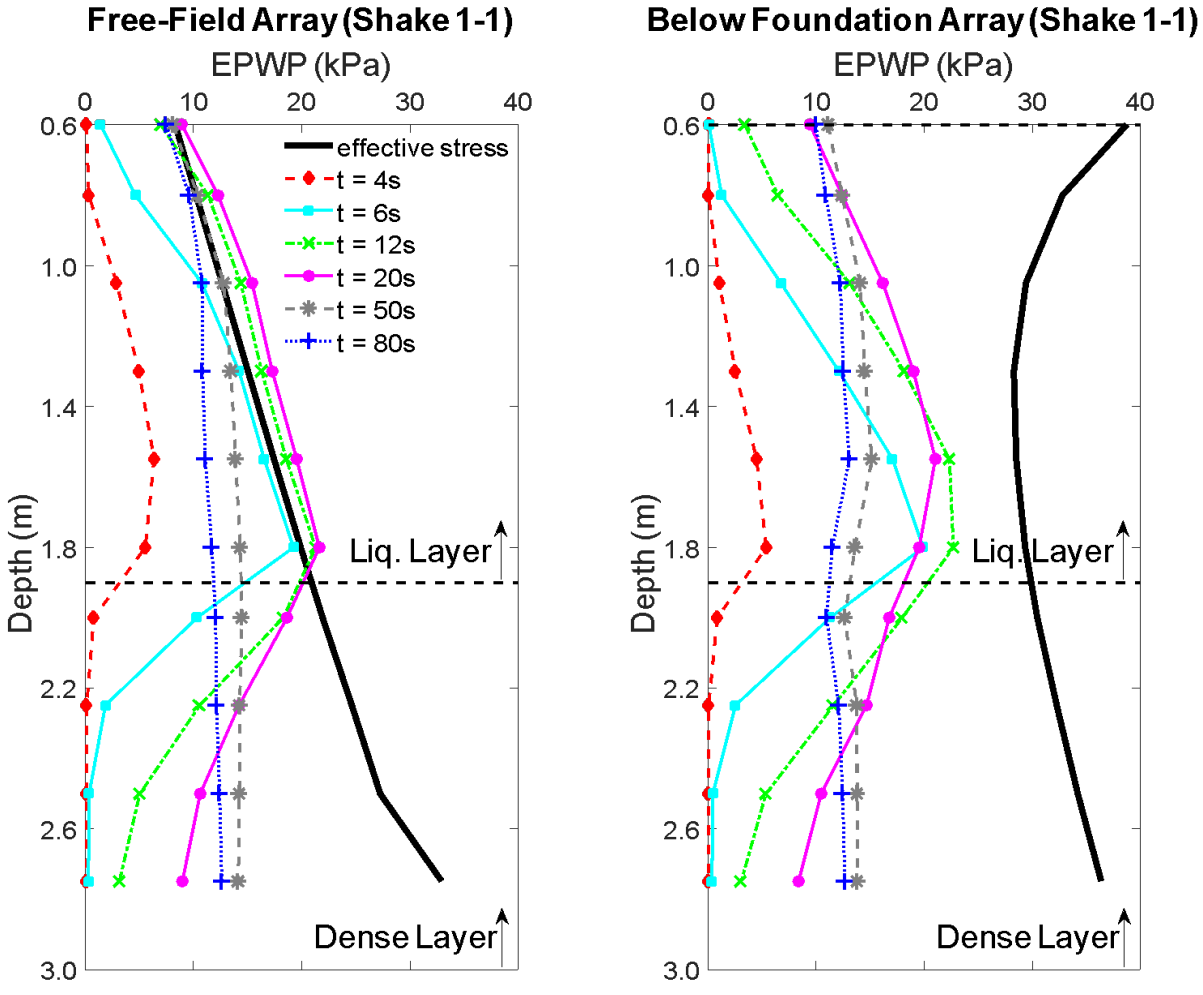

Figure 3.4 **Excess pore water pressure isochrones along depth of the soil profile for Shake 1-1 at free-field and below foundation arrays.**

3.1.3 Effect of Transient Hydraulic Gradient

The generated EPWP during strong shakings would result in high transient hydraulic gradients. Based on Darcy's law, the velocity of pore water is calculated using equation $V = k*i$, in which V is the velocity of the pore water, k is the hydraulic conductivity of the soil, and i is the hydraulic gradient. Before the shaking of the model in the experiment, there was no difference between total heads of any two points in the model ground. The generation of EPWP during liquefaction caused the total head difference at different depths inside the model ground. Assuming 1D flow along the model depth, the total head difference generated the flow of pore water in vertical direction. According to this assumption, the flow velocity of pore water during Shake 1-1 was calculated between consecutive PWP sensors in different depths and locations. Results of the calculated flow velocity time histories are presented in Figure 3.5 for the free-field case (i.e., dashed red lines) and below foundation (i.e., black continuous lines) arrays. The positive velocity between two PWP sensors indicates downward flow, while the negative velocity represents upward flow.

As can be seen in Figure 3.5, the maximum absolute flow velocity occurred in the boundary of dense and loose layers, indicating significant differences in the EPWP between dense and loose layers at the early stage of Shake 1-1. This observation is consistent with the data presented in Figures 3.2 and 3.3, where the rate of EPWP generation in the bottom of the loose layer was higher than the rates in the middle of the dense layer. The direction of flow at the top of the dense layer and at the boundary of the dense/loose layer was toward the dense layer (downward flow), whereas inside the loose layer, the direction of flow was upward. These observations can shed light on the fact that EPWP dissipation occurred sooner in the loose layer compared to the dense layer. In addition, the direction of upward flow coincides with the surface manifestation of sand ejecta, which occurred roughly after the shaking ceased. Multiple GoPro cameras (San Mateo, California) were utilized to capture the occurrence of ejecta, which indicated that the surface manifestation of ejecta started right after the shaking had ceased. The observed sand boil after Shake 1-1 is depicted in Figure 3.6, but there was no direct measurement of the volume of sand ejecta due to the excess water puddling on the ground surface after each shaking sequence.

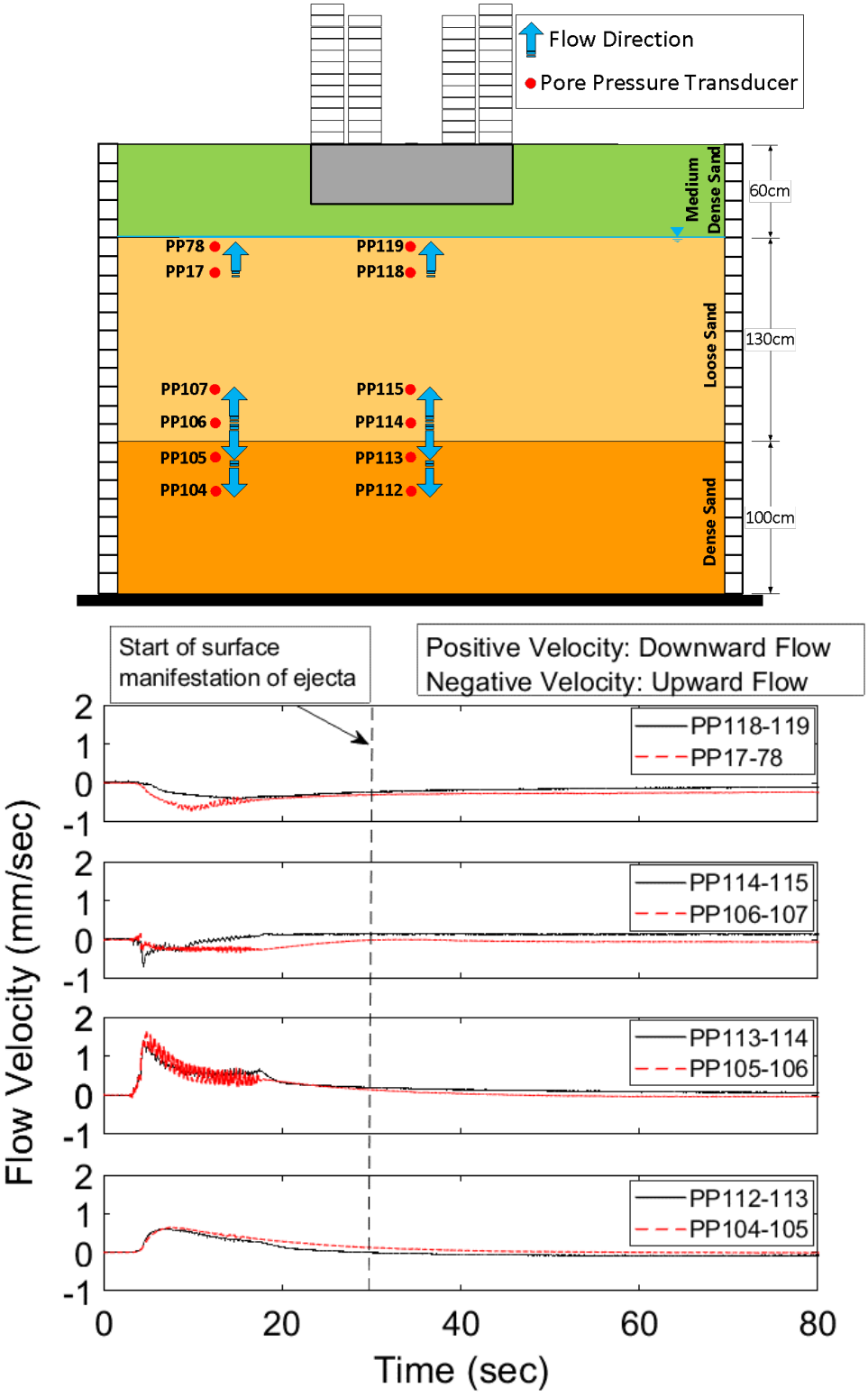

Figure 3.5 **Flow velocity between two consecutive PWP sensors during Shake 1-1 (Baseline test).**

Figure 3.6 Observed sand ejecta after Shake 1-1 (Baseline test).

3.1.4 Shear Stress–Strain Hysteresis Response

The shear-stress and strain-time histories and hysteresis loops were calculated using the acceleration records following the procedure outline by Zeghal and Elgamal [1994]; the results are presented in Figures 3.7 and 3.8 for the middle of the loose and dense layers, respectively. In this method, the shear–strain time histories were directly back calculated from the acceleration records; whereas the shear–stress values were obtained assuming a shear–beam condition in the free field. Higher shear stresses were generated at the middle of the dense layer compared to the middle of the liquefiable layer. The range of shear strains in the middle of both layers reached a maximum absolute value of 0.7%. Selected shear stress–strain hysteresis loops are presented in Figures 3.7 and 3.8 at different time steps during Shake 1-1. The stress–strain behavior in the middle of the liquefiable layer (Figure 3.7) indicated reduced stiffness after about 5 sec when the EPWP buildup became significant. As shown in Figure 3.8, there was no reduction in stiffness at the middle of the dense layer during selected time steps in Shake 1-1, which has been mainly attributed to the lower level of EPWP buildup.

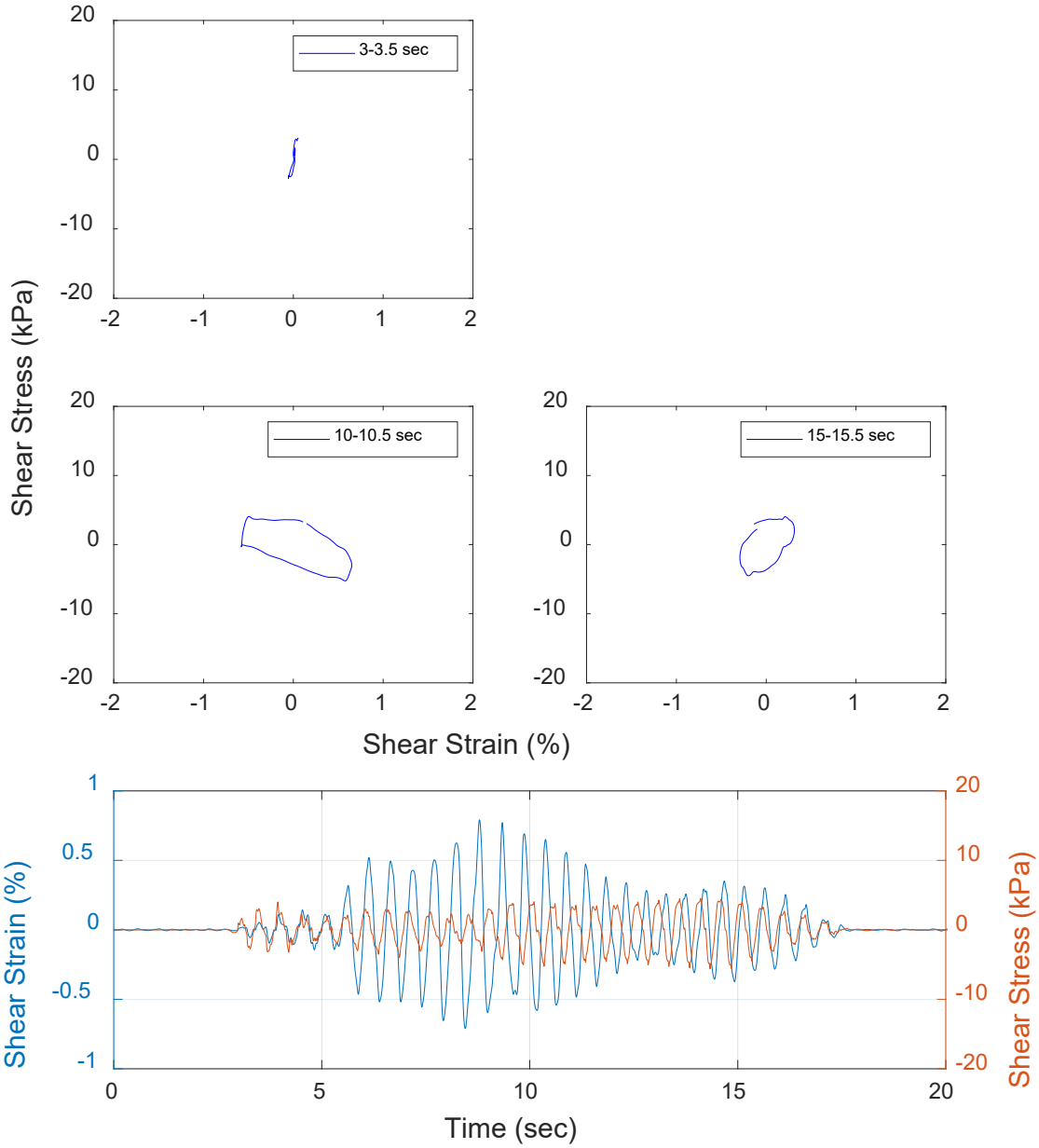

Figure 3.7 **Stress–strain loops generated at the middle of loose layer at selected time spans.**

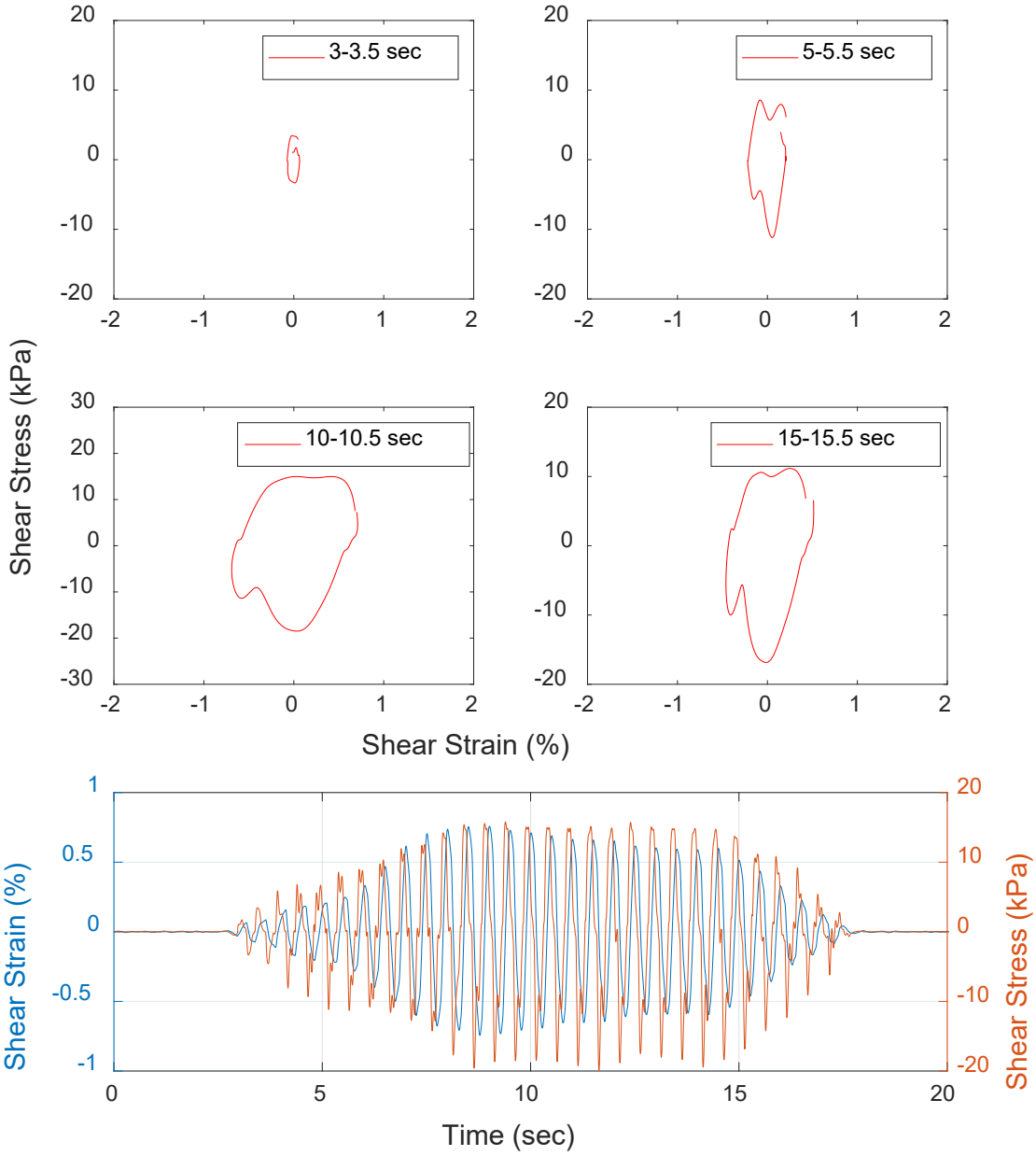

Figure 3.8 **Stress–strain loops generated at the middle of dense layer at selected time spans.**

3.1.5 Discussions of Damage Potential Cumulative Absolute Velocity

Recent research has evaluated the use of different IMs in liquefaction-induced foundation settlement calculation and reported that the plain CAV is a better predictor compared to other IMs [Karimi and Dashti 2017; Bullock et al. 2019]. Bray and Macedo [2017] extended this concept and considered damage potential cumulative absolute velocity (CAV_{dp}) as the most relevant IM to evaluate the amount of liquefaction-induced settlement. Bray and Macedo [2017] provided a simplified procedure to predict the amount of liquefaction-induced building settlement. This procedure includes CAV_{dp} as an IM to calculate shear-induced settlement of the foundation. In this study, the values of CAV_{dp} were calculated at different depths for both free-field and below foundation arrays during Shake 1-1 to further investigate on the effect of this IM on the amount of liquefaction-induced settlement.

Damage potential cumulative absolute velocity (CAV_{dp}) is defined in Campbell and Bozorgnia [2011] as:

$$\mathrm{CAV}_{dp} = \sum_{i=1}^{N} \left[H(\mathrm{PGA}_i - 0.025) \int_{i-1}^{i} |a(t)|\, dt \right] \tag{3.1}$$

where N is the number of discrete 1-sec time intervals, PGA_i is peak ground acceleration (g) in ith time interval, and $H(x)$ is the Heaviside Step Function [$H(x) = 0$ for $x < 0$ and $H(x) = 1$ for $x \geq 1$]. The CAV_{dp} is taken to be zero if S_a is less than $0.2g$ for periods between 0.2 and 0.5 sec, and S_v less than 15.34 cm/sec for periods ranging from 0.5 to 1 sec. The CAV_{dp} only utilizes a single component of a three-component acceleration record.

In this study, the acceleration records were applied and measured in a single horizontal direction only along the model length. Using the above equation and the acceleration time histories at different depths, the CAV_{dp} time histories were calculated and are presented in Figures 3.9 and 3.10 at the free field and below foundation arrays. In the case of the free-field array, the maximum generated CAV_{dp} is at the middle of the dense layer, while the corresponding maximum value for the array located below the foundation is at the bottom of the liquefiable layer. This indicates higher energy at similar depths in each array, which is in line with the acceleration time histories presented in Figures 3.2 and 3.3. The calculated CAV_{dp} for all other depths, including ground surface and the foundation itself, resulted in values lower than $0.5g$ sec. The importance of using damage potential cumulative absolute velocity as an IM to calculate settlement due to liquefaction is discussed in detail in Bray and Macedo [2017], and the calculated CAV_{dp} values (i.e., at different depths and arrays) were used herein to evaluate the liquefaction-induced settlement following the simplified procedure proposed by Bray and Macedo [2017], as discussed in detail in Chapter 4.

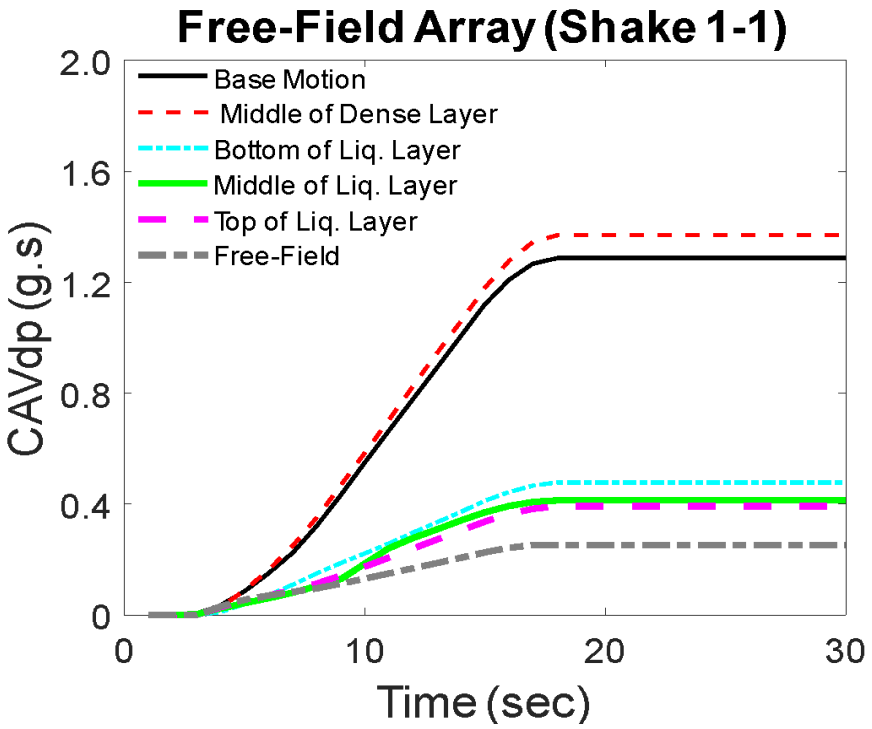

Figure 3.9 **CAV_{dp} at different depths along free-field ground during Shake 1-1.**

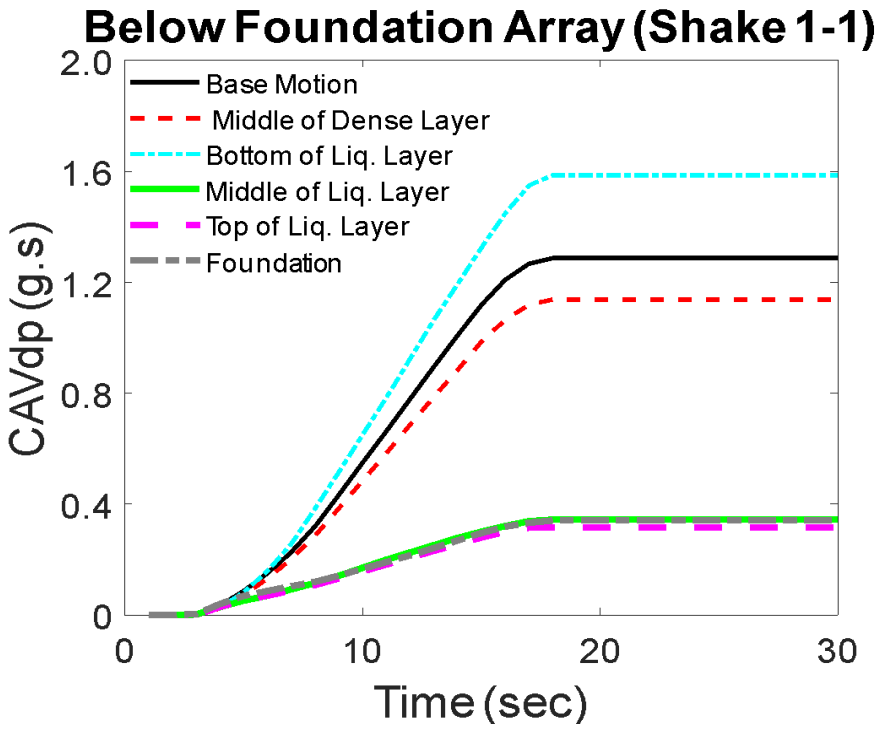

Figure 3.10 **CAV_{dp} at different depths below foundation during Shake 1-1.**

3.1.6 Liquefaction-Induced Foundation and Free-Field Settlements

Extensive foundation settlement was observed in this series of shake table tests. Figure 3.11(a) depicts the completed model just before the shaking sequence started; the effects of Shake 1-1 and 1-2 are shown in Figure 3.11(b) and 3.11(c), respectively. The shallow foundation tilted about 2° in-plane and punched into the soil after Shake 1-1 [Figure 3.11(b)], resulting in heave and significant cracks at the soil surface in the free field. The in-plane and out-of-plane differential settlement were 4.9 and 2 cm, respectively [Jahed Orang et al. 2020]. Excessive amount of settlement was also noted during Shake 1-2; see Figure 3.11(c).

The settlement-time histories of the foundation and ground surface (free field) for Shake1-1 and 1-2 are presented in Figures 3.12 and 3.13, respectively. The recorded foundation settlement using string potentiometer on each corner of the foundation for Shake 1-1 and 1-2 is summarized in Tables 3.1 and 3.2. The foundation and ground surface settlement during both shakings were measured using four string potentiometers and four linear potentiometers. The location of the settlement transducers is shown in Figure 2.3. For both shakings, the trends for settlement-time histories were similar in that the foundation started to sink inside the ground with the initiation of shaking and continued to settle in a relatively linear manner with respect to time until the shaking ceased. The settlement of the foundation continued even after the shaking ended, but the rate of settlement significantly decreased until it reached an asymptotic value, which was regarded as the total foundation settlement due to the liquefaction. The post shaking settlement of the foundation with respect to the total settlement of the foundation is presented in Figure 3.14 for both shakings, ranging on average 17 % and 7%, respectively. These percentages are attributed to mechanisms such as ground loss due to ejecta as well as post-liquefaction consolidation of liquefied soils. In the case of Shake 1-1, the post shaking settlement to the total settlement ratio (17%) was higher compared to Shake 1-2 (7%). Similar behavior was also reported in previous studies, such as Bray and Dashti [2014], which elaborated on the liquefaction-induced settlement and contributing components such as shear-induced, volumetric-induced, and ejecta-induced mechanisms.

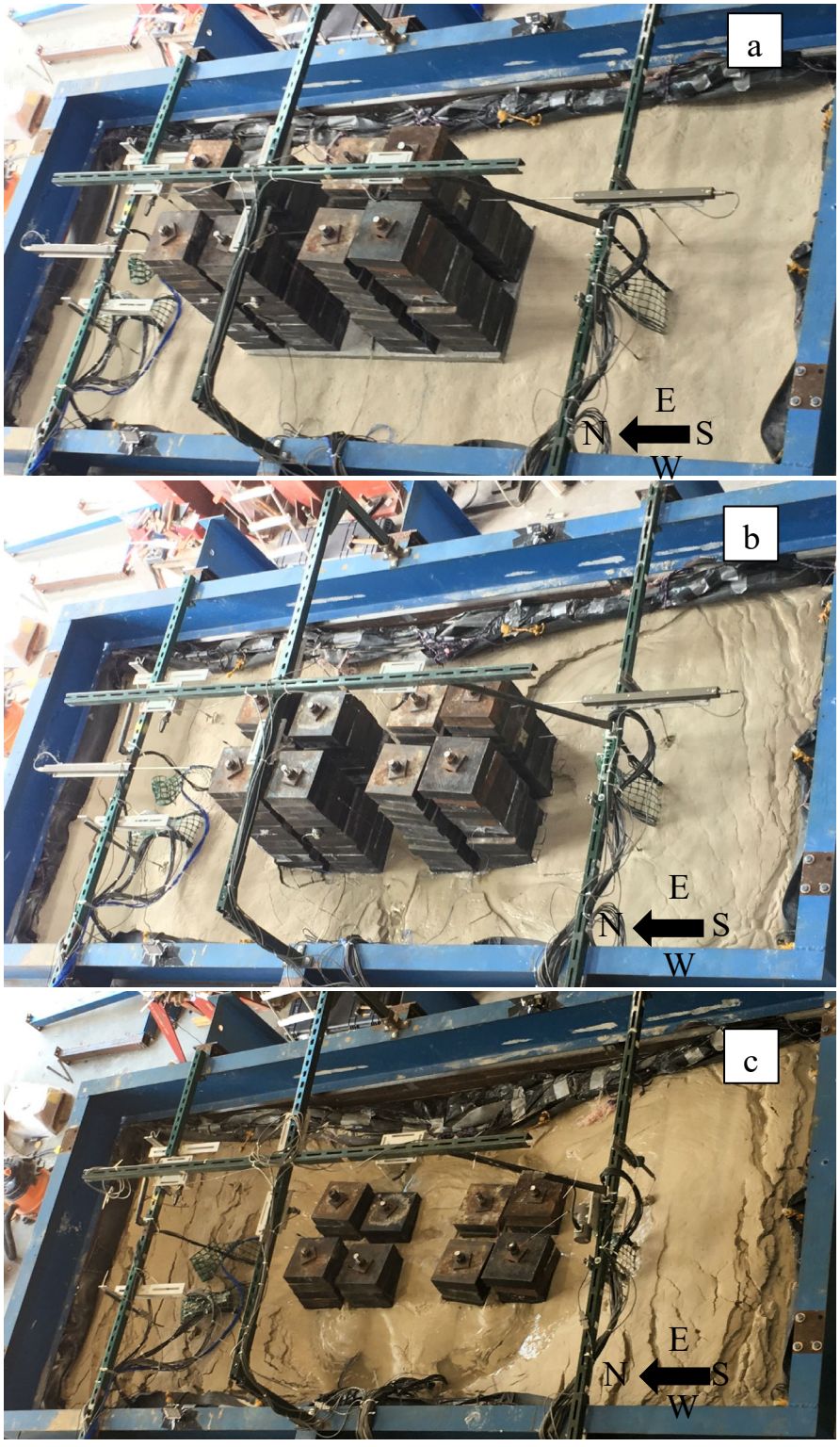

Figure 3.11 **Photos of Baseline model: (a) before Shake 1-1; (b) after Shake 1-1; and (c) after Shake 1-2.**

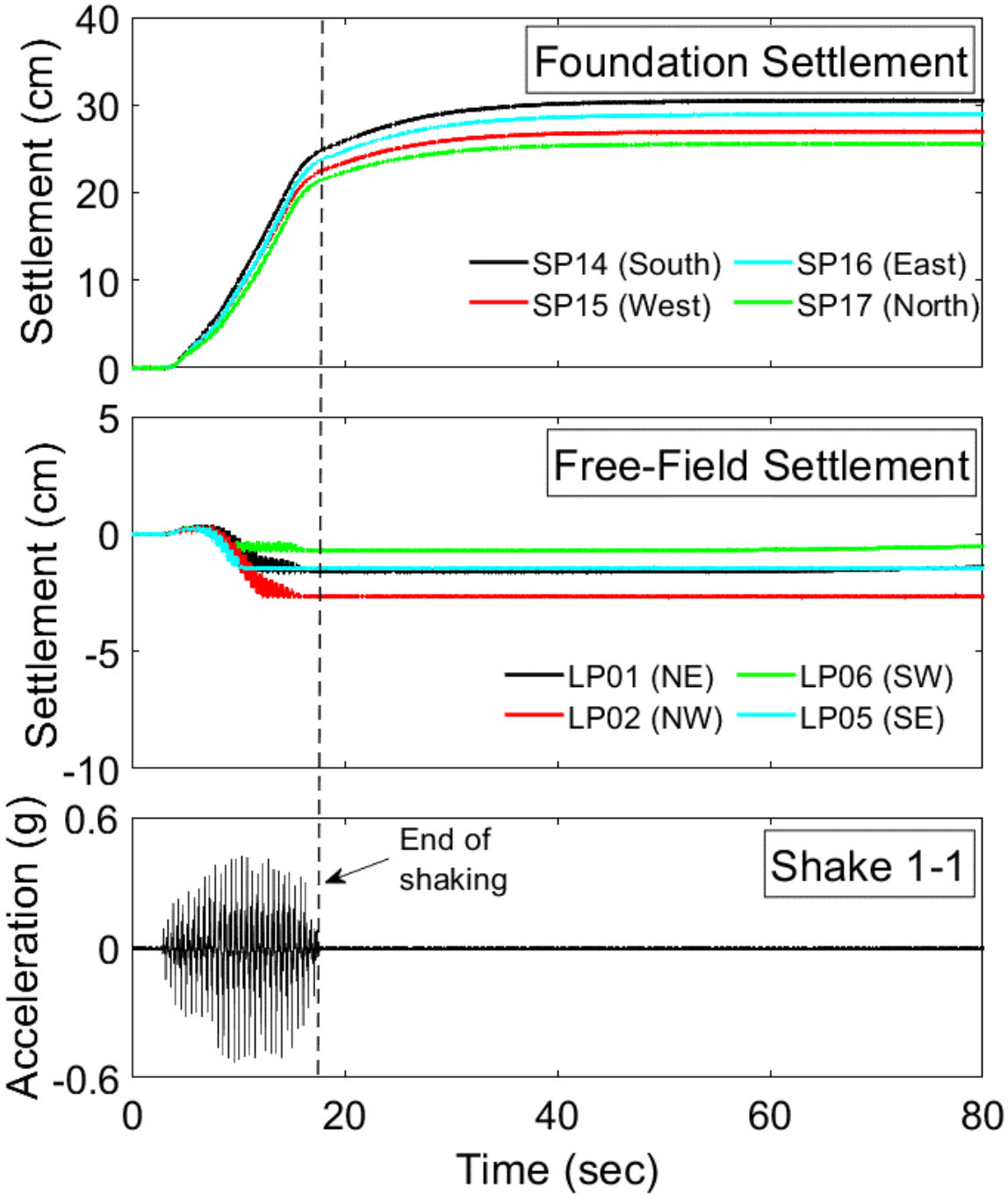

Figure 3.12 **Settlement time histories at the foundation and surface free-field level during Shake 1-1 (negative settlement values indicate heave in free-field settlements.).**

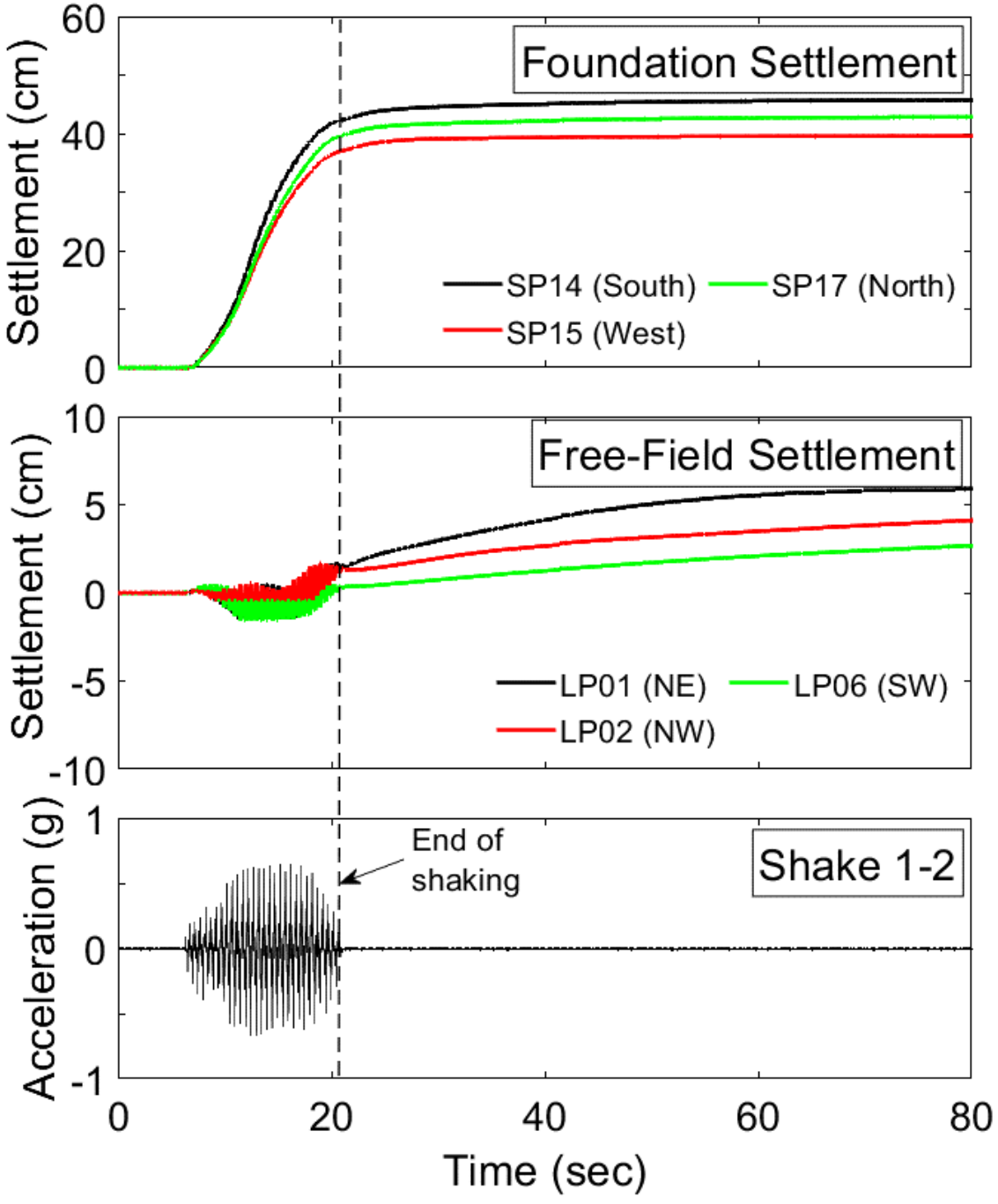

Figure 3.13 **Settlement time histories at the foundation and surface free-field level during Shake 1-2.**

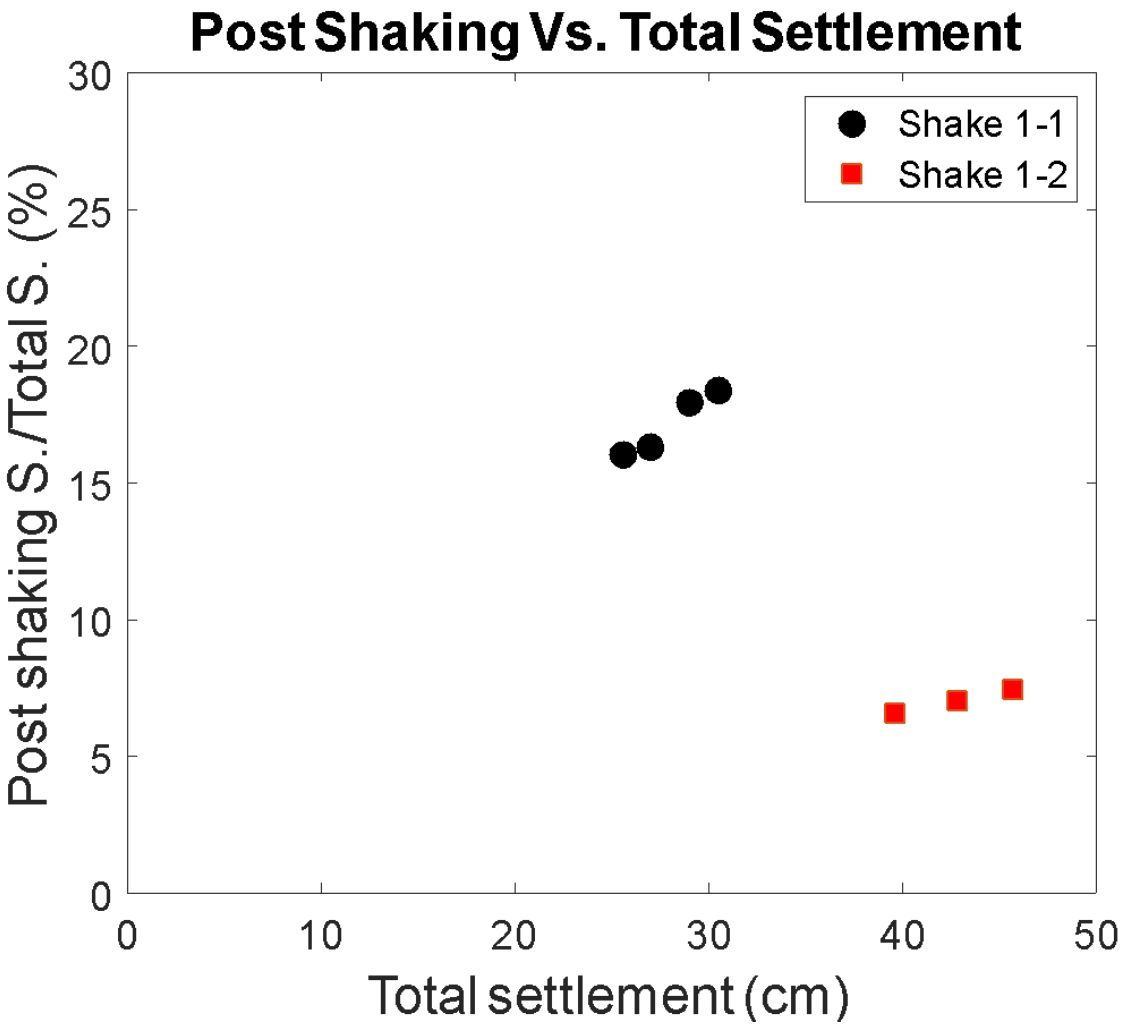

Figure 3.14 **Post-shaking foundation settlement ratio with respect to total foundation settlement for Shakes 1-1 and 1-2.**

Table 3.1 **Measured foundation settlement values for Shake 1-1 (values in cm).**

String pot. #	Total settlement	Settlement during shaking	Post shaking settlement
SP15	27.0	22.6	4.4
SP16	29.0	23.8	5.2
SP14	30.5	24.9	5.6
SP17	25.6	21.5	4.1
S_{avg}	28.0	23.2	4.8

In addition, the free-field settlement during both shaking events is presented in Figures 3.12 and 3.13. During Shake 1-1, there was some permanent heave due to the foundation bearing capacity failure. The average of four linear potentiometer measurements indicated a 1.6 cm heave during Shake 1-1. In the case of Shake 1-2, the average free-field settlement was 4.3 cm. Table 3.3 summarizes the measured settlement values for the free-field ground at the location of each linear potentiometer.

Shake 1-1 had a lower peak acceleration compared to Shake 1-2, resulting in lower total settlement of the foundation. The amount of settlement during Shake 1-2 was strongly affected by the bearing capacity failure of the shallow foundation as well as the consequent variation of the ground condition during Shake 1-1. Based on the chart presented by Vesic [1973], showing the modes of foundation failure in sand based on relative density and D_f to B^* ratio where D_f is the embedment depth and $B^* = (2BL)/(B+L)$, local shear failure of the foundation bearing capacity took place. In this study, embedment depth, foundation length, and width were 0.4 m, 1.3 m, and 0.4 m, respectively. Consequently, the D_f/B^* ratio was 0.61, and relative density for the crust layer was 53%, resulting in local shear failure type based on Vesic's [1973] chart that is consistent with the experimental observation and the heave at the free-field ground after Shake 1-1.

Table 3.2 Measured foundation settlement values for Shake 1-2 (values in cm).

String pot. #	Total settlement	Settlement during shaking	Post shaking settlement
SP15	39.6	37.0	2.6
SP14	45.7	42.3	3.4
SP17	42.8	39.8	3.0
S_{avg}	42.7	39.7	3.0

Table 3.3 Measured free-field settlement values for Shake 1-1 and 1-2 (values in cm).

Linear pot.	Total settlement		Settlement during shaking		Post shaking settlement	
	Shake 1-1	Shake 1-2	Shake 1-1	Shake 1-2	Shake 1-1	Shake 1-2
LP01	-1.6	6.0	-1.6	1.5	0	4.5
LP02	-2.7	4.2	-2.7	1.3	0	2.9
LP05	-1.5	2.7	-1.5	0.3	0	2.4
LP06	-0.7	-	-0.7	-	0	-
S_{avg}	-1.6	4.3	-1.6	1.0	0	3.3

3.2 HELICAL PILE TEST SERIES

The experimental findings for Helical Pile tests are provided in this section. Test results comparing the Baseline and Helical Pile test series are also discussed. Dashed lines are used to represent Baseline test results, and solid lines are used for Helical Pile test results in the figures presented throughout Section 3.2.

3.2.1 Experimental Findings

Measured data from two large-scale shake table test series were utilized to better understand the dynamic behavior of helical piles in liquefied soils and their efficacy in reducing liquefaction-induced shallow foundation settlement. Both test series featured similar model ground conditions and shallow foundations, with the ground model and structural components subjected to similar input motions described earlier. The acceleration time histories measured at various locations inside the ground model within different layers are presented in Figure 3.15. A comparison between these records illustrates a comparable response in acceleration time histories at the north and south arrays, indicating the reproduction of reasonable near-foundation conditions in both tests. Recorded accelerations at the surface exhibit two key features of liquefaction response: reductions in amplitude and period elongation. In addition, the observed higher frequency response in the below-foundation array compared to the near-foundation arrays for Helical Pile test could be attributed to higher confinement around helical piles as a result of helical pile installation.

The extent of mitigation efficiency can be seen in Figure 3.16. Both photos were taken after Shake 1, indicating a smaller settlement and tilt of the foundation during the Helical Pile test; see Figure 3.16(b). Extensive cracks and near-foundation heaves, along with the punching settlement of the foundation, occurred in the Baseline test; see Figure 3.16(a). Detailed discussions regarding EPWP generation, dynamic response of the helical piles, liquefaction-induced foundation and near-foundation settlements, foundation tilt and differential settlement, and the contribution of liquefaction-induced settlement mechanisms in both the Baseline and Helical Pile tests are provided hereafter.

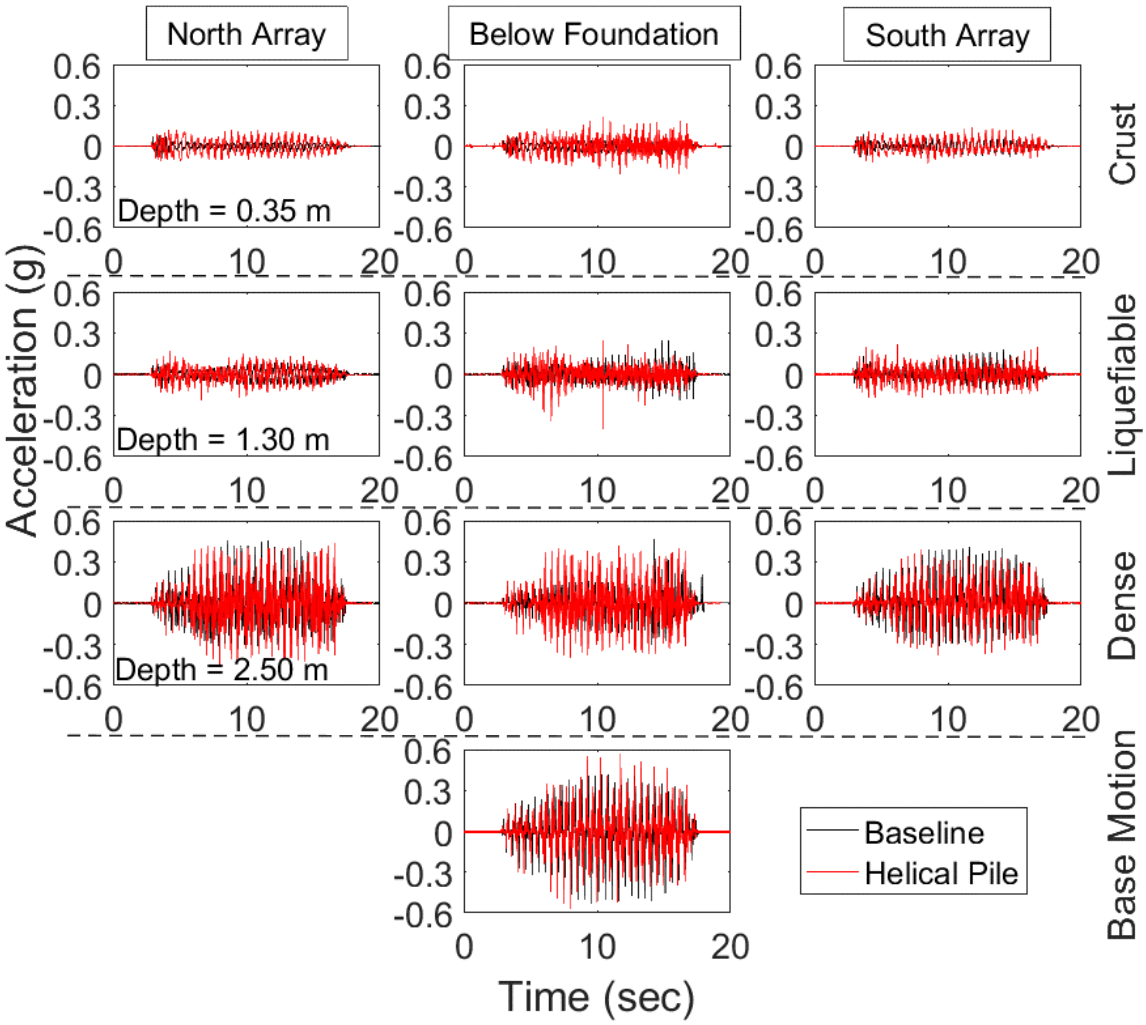

Figure 3.15 **Acceleration time histories at various depths within each layer during Shake 1.**

(a) **(b)**

Figure 3.16 **Ground model and shallow foundation after Shake 1 in (a) Baseline and (b) Helical Pile tests.**

3.2.2 Excess Pore-Water Pressure Generation

The generated EPWP isochrones in the near-foundation and below-foundation arrays are presented in Figure 3.17. These EPWP isochrones present time steps before, during, and after shaking for the Helical Pile test during Shake 1. As can be seen, the increase in EPWP within the dense layer continued even after shaking ceased. Moreover, the EPWP values were stabilized long after shaking (i.e., starting after t = 50 sec) along the depth of the ground model for both the near- and below-foundation arrays. In addition to the EPWP data, Figure 3.17 includes an estimate for the initial effective vertical stresses at the two locations, illustrating the significance of the shallow-foundation presence in the increased stresses at the below-foundation array; see Figure 3.17(b). The EPWP generation pattern within the liquefiable layer showed rapid buildup at the bottom half, which reached a steady state as the shaking proceeded. The patterns of the pore-water pressure generation/dissipation behavior were similar in both test series. Detailed discussions regarding EPWP response in the Baseline test series can be found in Jahed Orang et al. [2021a].

The EPWP contours along the depth and length of the ground model were also generated using three arrays of pore-water pressure sensors located at different depths and are presented in Figure 3.18. The internal MATLAB interpolation function was used to determine the EPWPs around three measured arrays. The contour plots represent the Baseline and Helical Pile tests during Shake 1 and the EPWP difference between these two tests. Three different time steps were selected to present the measured EPWP at different depths. The selected time steps were the time of maximum generated EPWP, middle of shaking (i.e., t = 10.5 sec), and long after shaking ceased (i.e., t = 80 sec).

The observed EPWPs during the Helical Pile test were generally lower than in the corresponding Baseline test, especially inside the zone of pile group influence at the bottom of the liquefiable and top of the dense layer. To some extent, this zone further extended around each pile. The EPWP difference in Figure 3.18 also illustrates higher variation around the group of helical piles. This effect is mainly attributed to the stress bulb generated around helical piles, which subsequently increased the relative density of the liquefiable layer at their zone of influence. In addition, densification around each pile as a result of installation could have contributed to this observation. The transferred foundation pressure through the helical piles into a more competent layer (i.e., dense layer) resulted in a higher surcharge carried through the dense layer during the Helical Pile test (this negates the reduced relative density of the dense layer due to soil disturbance around a group of helical piles), which further substantiates the observed maximum EPWP difference around the helical piles.

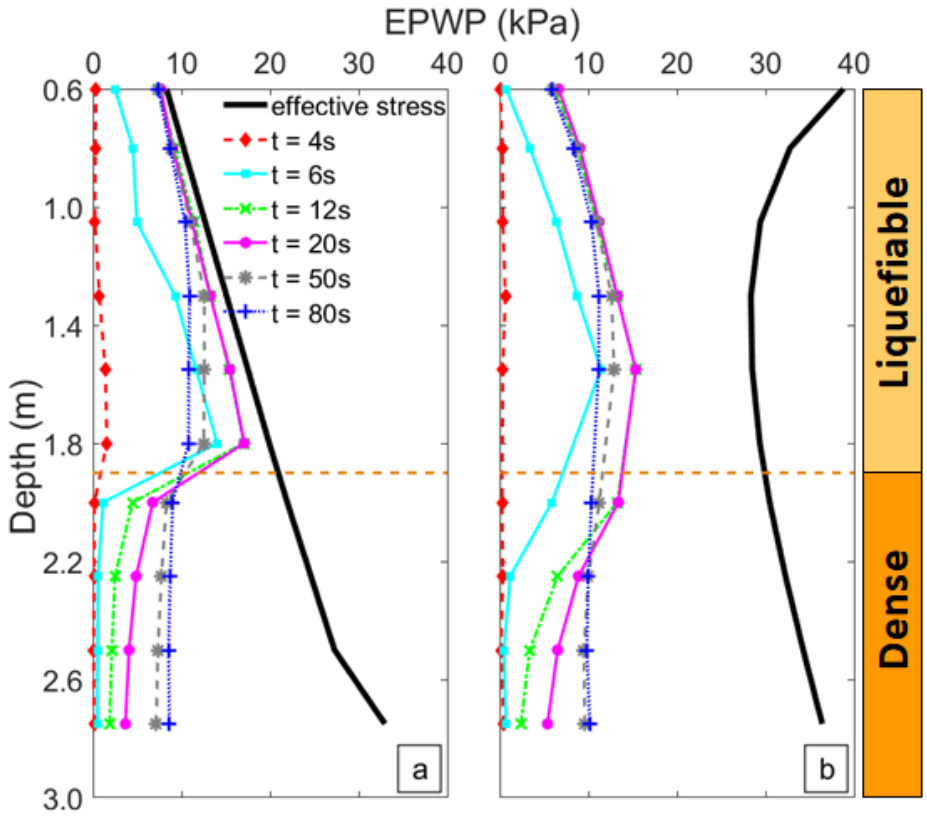

Figure 3.17 **EPWP isochrones for (a) near-foundation and (b) below-foundation arrays in Helical Pile test (Shake 1).**

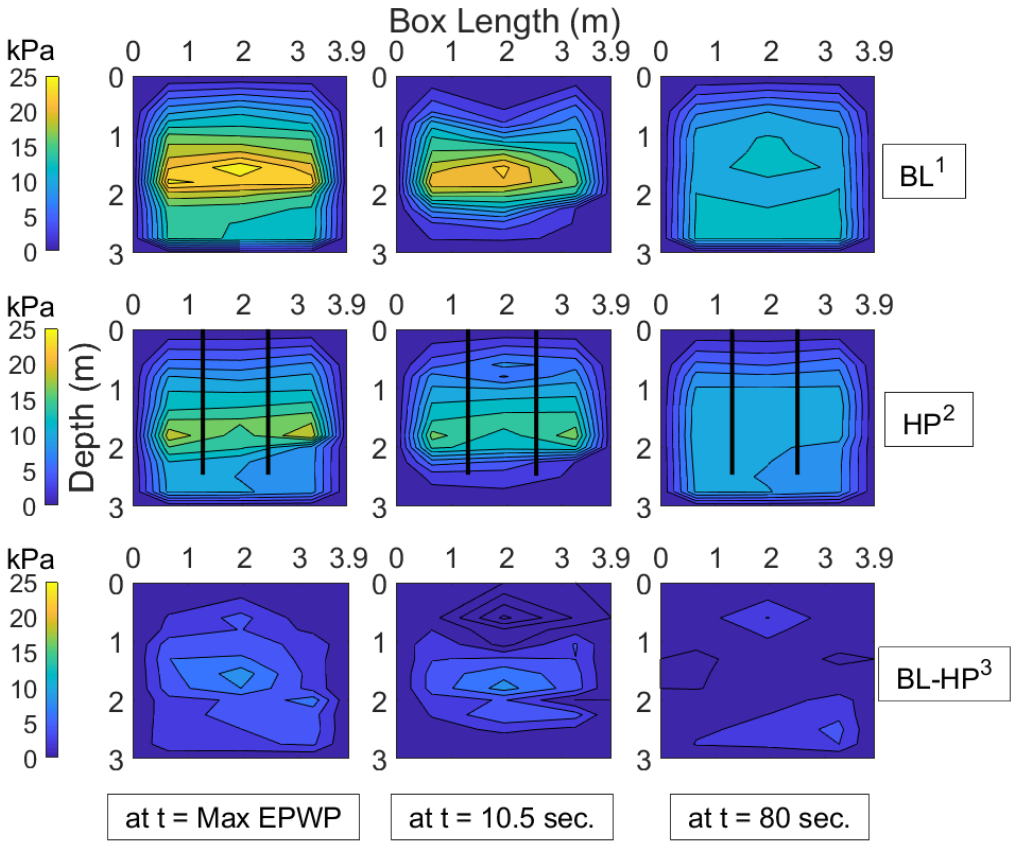

1Baseline test. 2Helical Pile test. 3EPWP difference.

Figure 3.18 **EPWP difference between Baseline and Helical Pile tests at time of maximum generated PWP, *t* = 10.5 sec (i.e., middle of shaking) and *t* = 80 sec (long after shaking ceased) during Shake 1.**

3.2.3 Dynamic Response of Helical Piles

The bending moment along the depth of each pile was measured using the attached strain gauges to evaluate the dynamic response of the helical piles, discussed in more depth below. The bending moment time histories were obtained using Equation (3.2), and the bending strain data measured by strain gauges attached on the piles at different depths:

$$M = \frac{(EI)_p(\varepsilon_1 - \varepsilon_2)}{D} \tag{3.2}$$

where D is the pile outer diameter; $(EI)_p$ is the bending stiffness of helical pile; and ε_1 and ε_2 are strain gauge readings at opposite sides of each pile section at their corresponding depth.

The maximum bending moments of piles at each depth were derived using the absolute maximum bending moment observed in the time histories. Figure 3.19 presents the bending moment time histories at different depths in selected helical piles during Shake 1, and Figure 3.20 exhibits the calculated maximum bending moments along depth for all the piles. Several researchers have studied the response of piles in layered soil profiles involving liquefiable soils.

For example, Abdoun et al. [2003] used model steel-driven piles in a series of centrifuge tests to study their dynamic behavior in layered soil deposits. A critical observation from Abdoun et al. [2003]'s study was the maximum bending moment at the loose-dense layer interface, which is attributed to the shear discontinuity effect. This effect is mainly due to the difference in the shear stiffness of the loose and dense layers, where both layers undergo the same shear stresses, ultimately resulting in the maximum bending moment at the interface of loose and dense layers [Abdoun et al. 2003]. A similar response was also observed in this series of tests, where the maximum bending moments along the helical piles occurred at the interface of the liquefiable-dense layers for all the single-helix helical piles during both shaking sequences; see Figure 3.20. As can be seen in Figure 3.20, all the helical piles exhibited similar responses during both shakings, which is also expected due to the similarity in the size, shape, and number of helices in all helical piles. Overall, the bending moments along depth during Shake 2 were generally higher, especially within the dense and lower half of the liquefiable layer compared to the measured bending moments at corresponding depths during Shake 1. This is also expected due to densification of the ground layers due to post-liquefaction consolidation discussed using the CPT-tip resistance data presented in Figure 2.15(b).

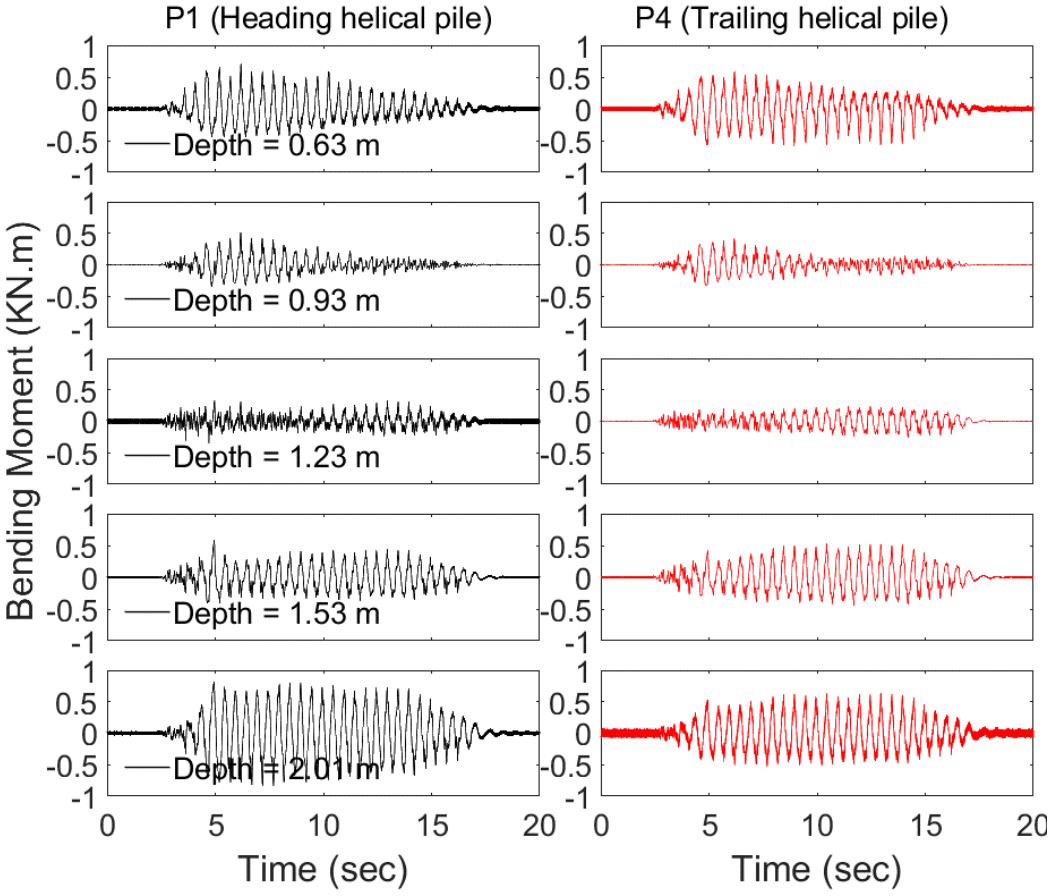

Figure 3.19 **Bending moment time histories at different depths in heading (P1) and trailing (P4) helical pile.**

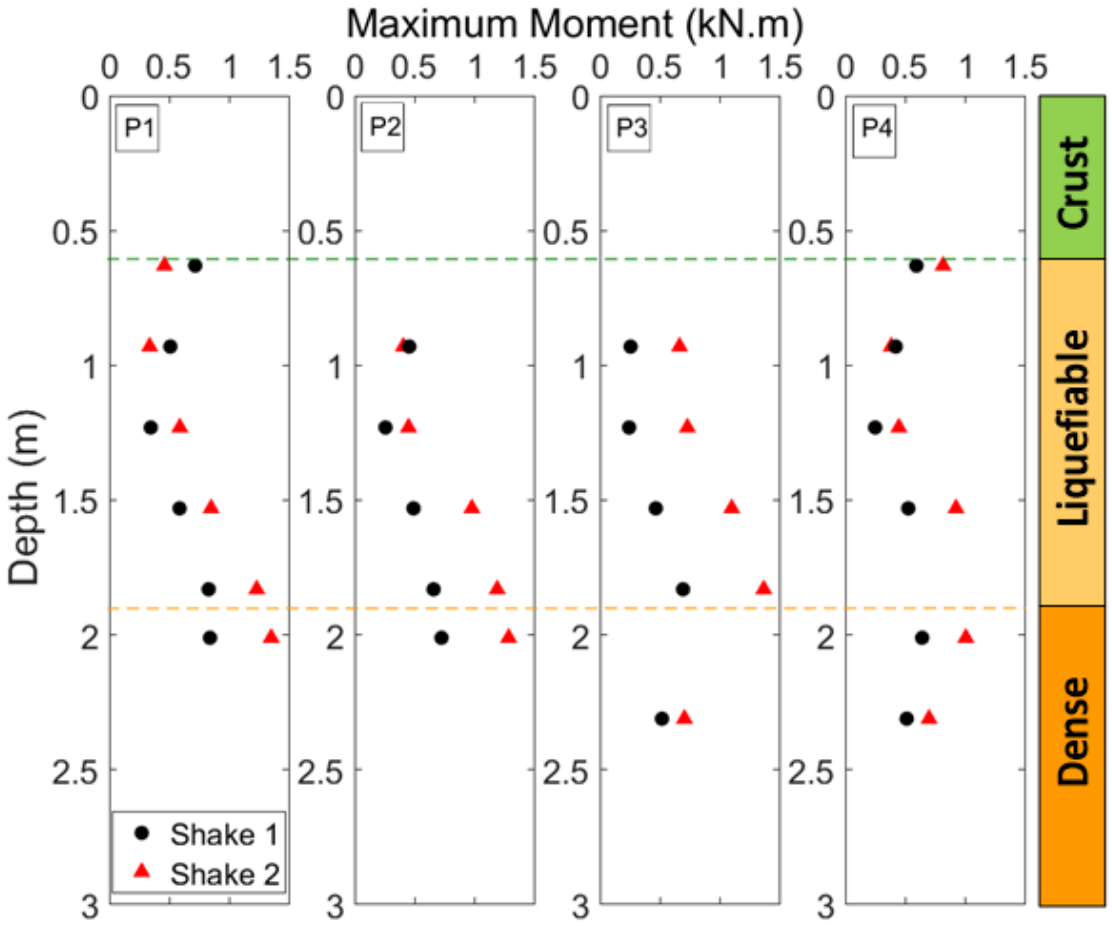

Figure 3.20 **Maximum bending moment along depth for both Shake 1 and Shake 2 for all the helical piles.**

3.2.4 Liquefaction-Induced Foundation and Near-Foundation Settlements

The foundation and near-foundation settlements were measured using string and linear potentiometers during both test series. Four string potentiometers were used to measure foundation settlement at four different locations as shown in Figure 2.12, while four linear potentiometers were utilized to record settlement of the near-foundation ground indicated in Figure 2.12. Figure 3.21 presents the foundation settlement for both test series during Shake 1. At four different locations during the Helical Pile test, the measured foundation settlement was almost twenty times lower than the corresponding foundation settlement in the Baseline test. Note the different scales for the *y*-axes in Figure 3.21: there was no observed foundation settlement after the shaking ceased during the Helical Pile test, whereas there was a visible and continuous post-shaking component of liquefaction-induced foundation settlement in the Baseline test. Details of foundation and near-foundation settlements and contribution of different liquefaction-induced foundation settlement mechanisms during the Baseline test series are thoroughly discussed in Jahed Orang et al. [2021a].

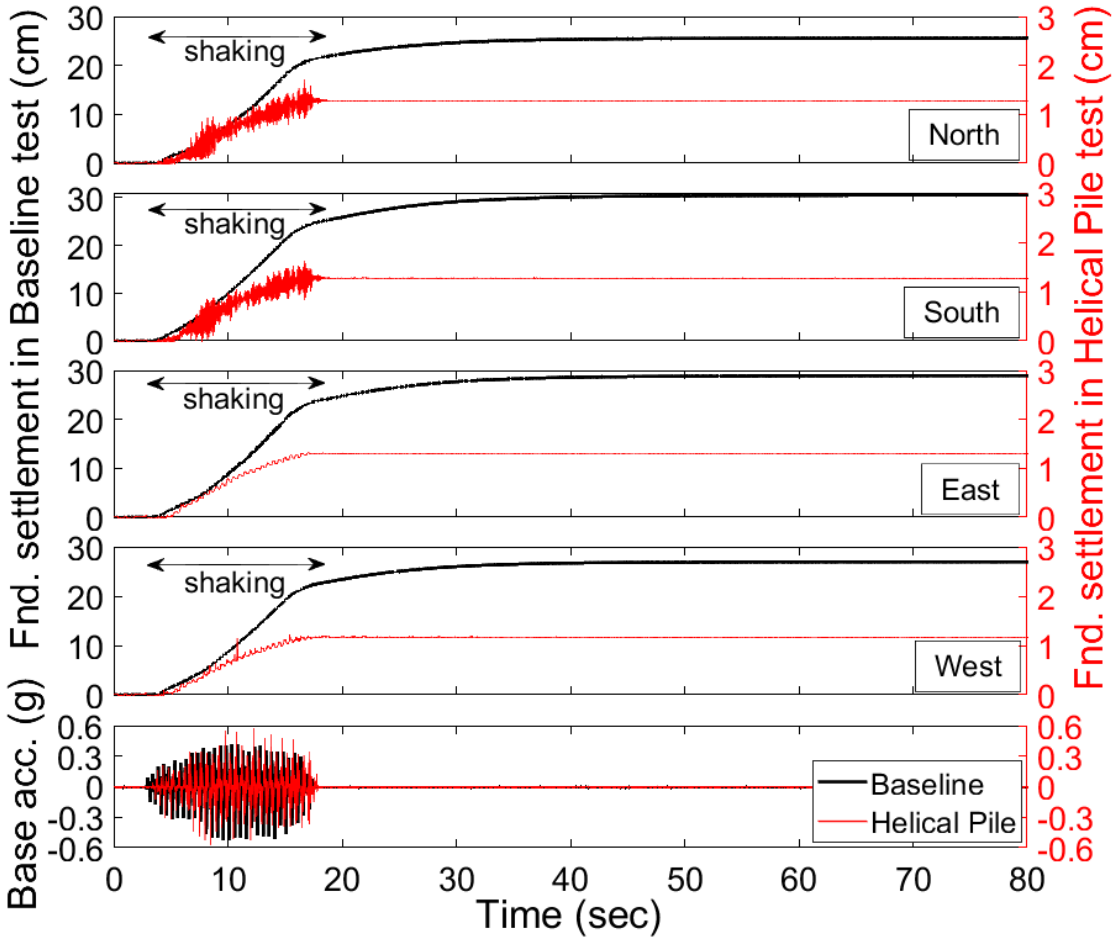

Figure 3.21 Foundation settlement at four different locations during Shake 1.

The measured near-foundation and foundation settlements during both shakes are summarized in Tables 3.4 and 3.5, respectively. These measured values are also illustrated in Figures 3.22(a) and 3.22(b). The total measured settlements are divided into two categories depending on their occurrence time (during or after shaking), and are labeled as "settlement during shaking" and "post-shaking settlement" in this section.

The total near-foundation settlements measured at four different locations presented in Table 3.4 and Figure 3.22(a) were fairly comparable for the Baseline and Helical Pile tests during Shake 2; however, higher post-shaking settlements were observed in the Baseline test compared to the Helical Pile test due to the continuous settlement even when the shaking ceased. The substantial post-shaking settlement in the Baseline test is attributed to observed sand ejecta and post-shaking consolidation of the liquefied soil layer. The latter component was absent in the Helical Pile test. Figure 3.23 shows the observed sand ejecta near the shallow foundation after Shake 1 in the Helical Pile test. Negative near-foundation settlement values, indicating the observed heave during the Baseline test for Shake 1 as a result of the local shear bearing capacity failure of the shallow foundation, were caused by reduced shear strength and stiffness of the liquefiable soil during shaking and manifested as near-foundation heave at all four measuring

locations [Motamed et al. 2020]; Jahed Orang et al. 2021a]. Nonetheless, the positive near-foundation settlement values indicated settled ground conditions in the Helical Pile test where no bearing capacity failure of the shallow foundation was observed during either shake test. The average near-foundation settlements are also tabulated in Table 3.4.

Figure 3.22(b) compares the foundation settlements measured during and after shaking in both test series. There was no measured post-shaking settlement of the foundation during the Helical Pile test series since the foundation load was transferred to the bottom dense layer by the helical piles. The significant extent of foundation settlement mitigation is also illustrated in Figure 3.22(b), in which the foundation settlements were reduced drastically in both shakes where helical piles were used as a countermeasure. Different liquefaction-induced settlement mechanisms contributed to the foundation and near-foundation settlements during each shake. Further discussion on the controlling mechanisms is provided in Section 3.3.6.

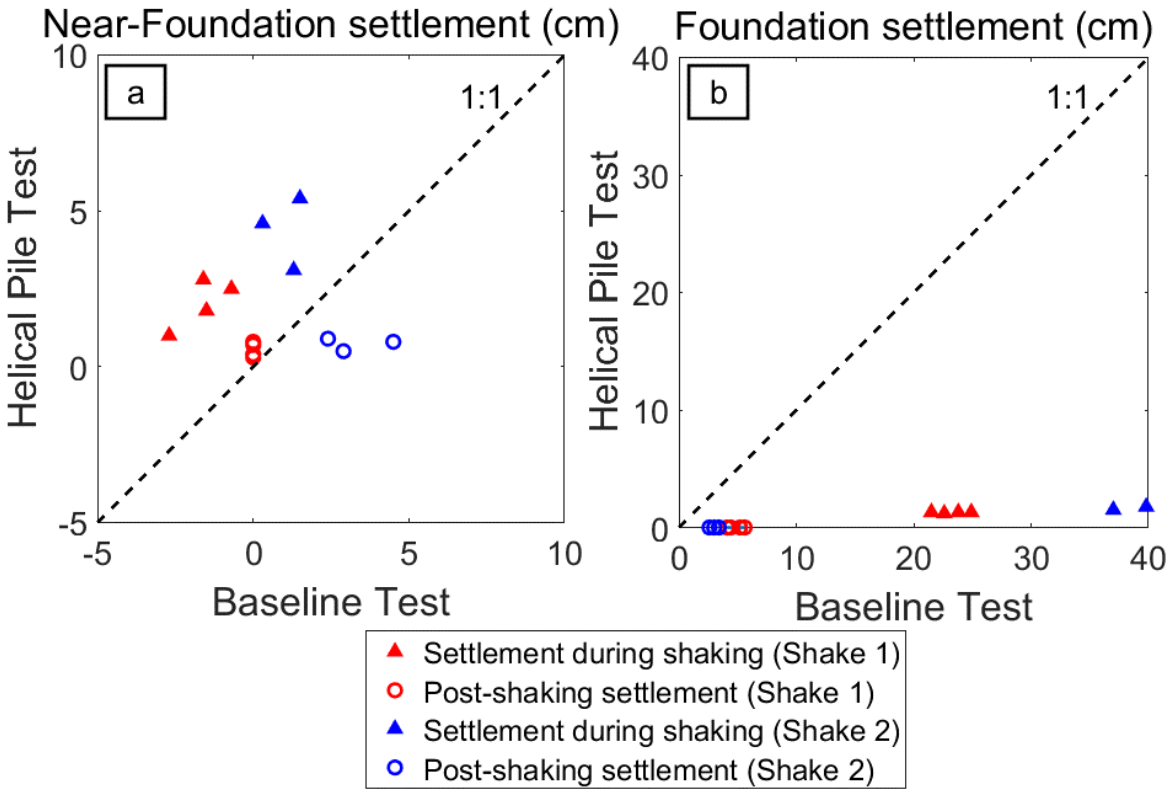

Figure 3.22 **(a) Near-Foundation and (b) foundation settlement during Baseline and Helical Pile tests for both Shakes 1 and 2.**

Figure 3.23 **Observed sand ejecta in both (a) eastern and (b) western side of the soil box in the Helical Pile test after Shake 1.**

Table 3.4 **Near-foundation settlements in Baseline and Helical Pile tests for both Shakes 1 and 2.**

	Total settlement (cm)				Settlement during shaking (cm)				Post-shaking settlement (cm)			
Test	**Baseline***		**Helical Pile**		**Baseline**		**Helical Pile**		**Baseline**		**Helical Pile**	
Shake No.	1	2	1	2	1	2	1	2	1	2	1	2
Northeast	-1.6	6.0	3.6	6.2	-1.6	1.5	2.8	5.4	0.0	4.5	0.8	0.8
Northwest	-2.7	4.2	1.3	-	-2.7	1.3	1	-	0.0	2.9	0.3	-
Southeast	-1.5	2.7	2.2	3.6	-1.5	0.3	1.8	3.1	0.0	2.4	0.4	0.5
Southwest	-0.7	-	3.2	5.5	-0.7	-	2.5	4.6	0.0	-	0.7	0.9
Average	-1.6	4.3	2.6	5.1	-1.6	1.0	2.0	4.4	0.0	3.3	0.6	0.7

*Negative values indicate heave

Table 3.5 Foundation settlements in Baseline and Helical Pile tests for both Shakes 1 and 2.

	Total settlement (cm)				Settlement during shaking (cm)				Post-shaking settlement (cm)			
Test	Baseline		Helical Pile		Baseline		Helical Pile		Baseline		Helical Pile	
Shake No.	1	2	1	2	1	2	1	2	1	2	1	2
North	25.6	42.8	1.3	1.8	21.5	39.8	1.3	1.76	4.1	3.0	0.0	0.0
South	30.5	45.7	1.3	-	24.9	42.3	1.3	-	5.6	3.4	0.0	0.0
East	29.0	-	1.3	1.7	23.8	-	1.3	1.7	5.2	-	0.0	0.0
West	27.0	39.6	1.2	1.5	22.6	37.0	1.2	1.5	4.4	2.6	0.0	0.0
Average	28.0	42.7	1.26	1.67	23.2	39.7	1.26	1.67	4.8	3.0	0.0	0.0

3.2.5 Foundation Tilt and Differential Settlement

This study assessed the performance of helical piles in minimizing the adverse effects on superstructures as a result of liquefaction-induced foundation movements. As a result, the settlement-rotation response of the foundation during the Baseline and Helical pile tests were evaluated; the results are presented in Figure 3.24. As can be seen, the tilt of the foundation in the Helical Pile test was measured as very small during both shakes, with the residual value of almost zero; however, the measured residual foundation rotation in the Baseline tests were 0.038 radians (2.2°) and 0.022 radians (1.3°), respectively. The maximum foundation rotation during the second shake in the Baseline test was 0.026 radians (1.5°), as shown in Figure 3.24. In addition, the rate of tilt accumulation was higher during Shake 1 compared to Shake 2 in the Baseline tests, as illustrated in Figure 3.24, with a steeper response in Shake 1. Overall, the use of helical piles resulted in superior performance of the shallow foundation and impeded foundation movements including settlement and tilt during the liquefaction phenomenon compared to the response of the Baseline tests.

In-plane and out-of-plane differential settlements of the foundation are illustrated in Figure 3.25. The ground motion was applied in the north–south direction along the laminar soil box during both test series. The amount of in-plane and out-of-plane differential settlements in the Baseline tests were 4.9 and 2.0 cm, respectively; however, the use of helical piles merely compensated the foundation differential settlement in both directions. These observations, along with the negligible measured foundation tilt, verified the improved performance of the shallow foundation underpinned with helical piles in liquefiable ground conditions.

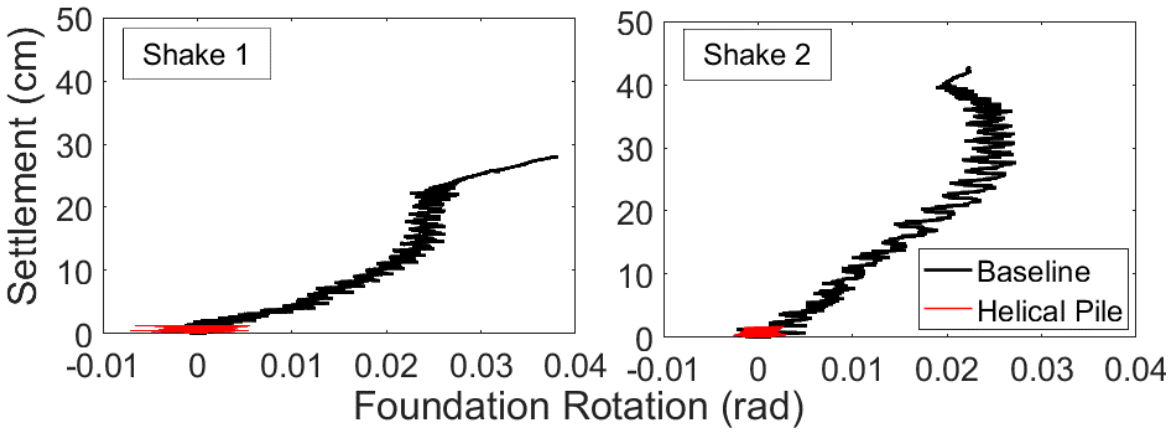

Figure 3.24 **Settlement-rotation of the shallow foundation during Baseline and Helical Pile tests.**

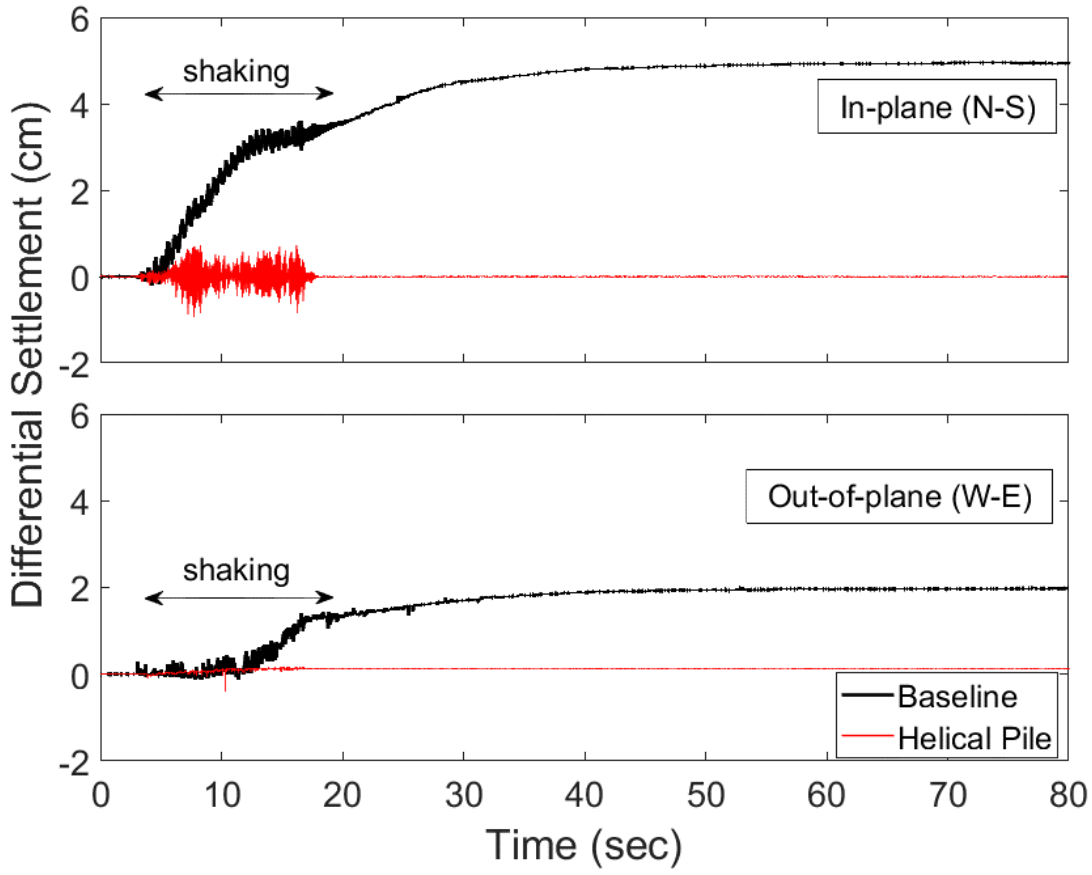

Figure 3.25 **In-plane and out-of-plane differential settlement during Baseline and Helical Pile tests (Shake 1).**

3.2.6 Discussion on the Contributing Settlement Mechanisms

As presented in Chapter 1, liquefaction-induced foundation settlement mechanisms are categorized as follows: (1) volumetric-induced, (2) shear-induced, and (3) ejecta-induced. Each of these mechanisms contributes to the foundation settlement during and after shaking. Figure 3.26 demonstrates the average foundation settlement during both shakes in the Baseline and Helical Pile tests. These average settlements were obtained from four string potentiometer measurements presented earlier in Table 3.5. The improved performance of the shallow foundation during the Helical Pile test during both shakes can be seen in Figure 3.26: a significant reduction in the foundation settlement (96% on average) was achieved, demonstrating the efficacy of using helical piles to mitigate liquefaction-induced shallow foundation settlements.

The contribution of liquefaction-induced settlement mechanisms was evaluated during both test series using the presented time histories in Figure 3.26. All the listed settlement mechanisms contributed to the foundation settlement during the Baseline tests, as discussed below. The settlement of the foundation during shaking is attributed to the shear-induced mechanism (including SSI ratcheting and partial bearing capacity failure), as well as the high hydraulic transient gradients. Although this mechanism existed in both the Baseline and Helical Pile tests, its magnitude was significantly higher in the Baseline tests, resulting in 23.2 cm and 39.7 cm of settlement during Shake 1 and 2, respectively. The corresponding numbers in the Helical Pile tests were 1.3 cm and 1.7 cm, illustrating a 95% reduction on average. The observed mitigation in the foundation settlement during the Helical Pile tests (Figure 3.26, solid lines) indicated a significant reduction in the contribution of these two mechanisms, coupled with the exclusion of foundation bearing capacity failure as a result of helical piles. Comparison between the rates of settlement accumulation between the two tests (i.e., the average rate of settlement during Shake 1 in the Baseline and Helical Pile tests were 1.5 cm/sec and 0.08 cm/sec, respectively) further substantiates the effectiveness of helical piles to mitigate liquefaction-induced damage.

As illustrated in Figure 3.26, the post-shaking settlement mechanisms included ejecta-induced and volumetric-induced settlement (excluding the high hydraulic transient gradients), where the contribution of these mechanisms after shaking ceased. During the Baseline tests, the shallow foundation continued to settle up to 4.8 cm and 3.0 cm after Shake 1 and 2, respectively. These numbers indicate a smaller post-shaking settlement accumulation compared to the shaking phase in the Baseline tests. In contrast, the use of helical piles resulted in practically no observed foundation settlement after both shakings ceased. This observation indicates that the post-shaking settlement mechanisms were eliminated in the Helical Pile tests.

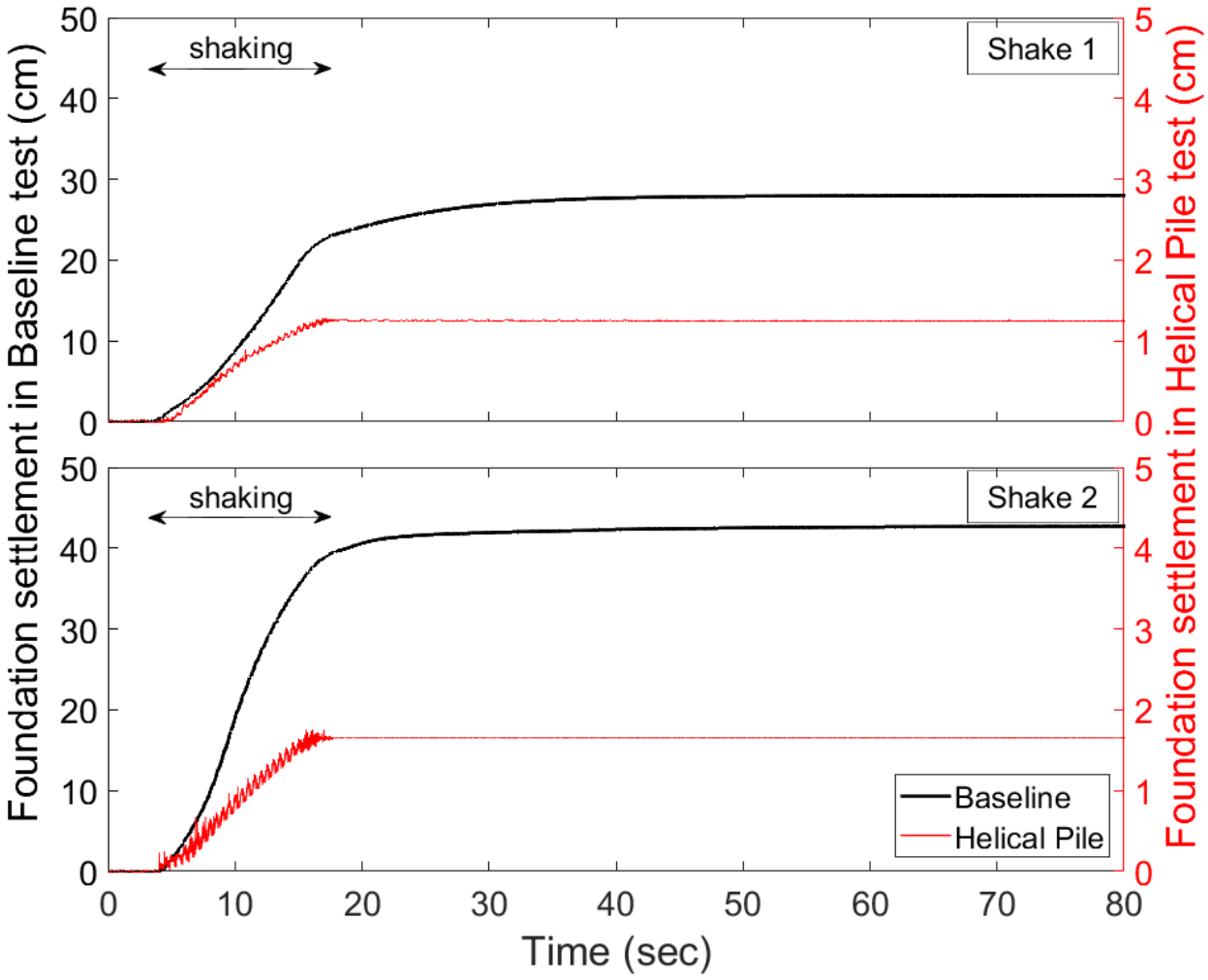

Figure 3.26 Average foundation settlement in Baseline and Helical Pile tests.

4 Liquefaction-Induced Building Settlement Estimation

4.1 VOLUMETRIC-INDUCED SETTLEMENT

The volumetric-induced settlement (D_v) was calculated based on the Ishihara and Yoshmine's [1992] methodology, in which the post-liquefaction volumetric strain is obtained based on a *FS* term against liquefaction (FS_L) for different relative densities of clean sand. Calculation for the volumetric-induced settlement was made using the achieved relative densities for each soil layer; see Table 2.2. A high *FS* against liquefaction ($FS_L > 1$) was assumed for the dense layer, while the *FS*s against liquefaction for the liquefiable layer was 0.80 based on calculated τ_{cyc} and $\tau_{cyc,L}$. The pore pressure sensors in unsaturated crust layer indicated no EPWP generation, which means liquefaction was not triggered in the unsaturated crust layer during Shake 1-1. The presence of unsaturated crust can lead to lower foundation settlement. Several past research has indicated that lowering the groundwater level (i.e., unsaturated top layer) resulted in lower foundation settlement compared to saturated and dry ground model conditions [Mirshekari and Ghayoomi 2017; Borghei et al. 2020]. Consequently, a high *FS* ($FS_L > 1$) was also assumed for the top crust layer in the volumetric-induced settlement calculations. The volumetric strain in each layer was subsequently multiplied by its corresponding layer thickness, resulting in 5.5 cm of volumetric-induced settlement for the Baseline test during Shake 1-1.

4.2 SIMPLIFIED PROCEDURE BY BRAY AND MACEDO [2017] FOR SHEAR-INDUCED SETTLEMENT

Bray and Macedo [2017] recently introduced a simplified procedure to calculate the liquefaction-induced building settlement. The simplified procedure was suggested to calculate the amount of shear-induced settlement (D_s) based on the results of 1300 analyses conducted using FLAC Version 7.0 with PM4Sand as the constitutive model in Bray and Macedo [2017]. The final form of the equation for shear-induced settlement is:

$$Ln(Ds) = c1 + 4.59 * Ln(Q) - 0.42 * Ln(Q)^2 + c2 * LBS + 0.58 * Ln\left[\operatorname{Tan\,h}\left(\frac{HL}{6}\right)\right] - 0.02 * B + 0.84 * Ln(\mathrm{CAV}_{dp}) + 0.41 * Ln(Sa_1) + \varepsilon \quad (4.1)$$

where the variables in Equation (4.1) are defined in the notation list. The liquefaction building settlement index is calculated as:

$$LBS = \int_{0.6}^{1.9} W * \frac{\varepsilon_{\text{shear}}}{z} dz \tag{4.2}$$

Description of the variables used to calculate *LBS* is provided in Bray and Macedo [2017]. The upper and lower bounds in Equation (4.2) indicate the depth of the top and bottom of the liquefiable layer measured from the ground surface. In order to calculate $\varepsilon_{\text{shear}}$, the *FS* against liquefaction (FS_L) is required. The *FS* against liquefaction for Shake 1-1 was 0.80. The estimated shear-induced settlement based on this simplified procedure is presented in Table 4.1. The presented values for CAV_{dp} and S_{a1} IMs were calculated using DEEPSOIL V7.0 [Hashash et al. 2020] based on equivalent linear analysis assuming no liquefaction in free-field ground condition, which is consistent with the recommendations by the Bray and Macedo's simplified procedure. According to the calculated results the mean D_s was 3.3 cm based on $FS_L = 0.80$; see Table 4.1.

The D_s in this case varies from 2 cm–5.4 cm due to the error term variation (i.e., $-0.5 \leq \varepsilon \leq 0.5$). Note: if the presented CAV_{dp} values in Section 3.2.4 were used in this procedure, the calculated settlements would be even lower. The lower-than-usual S_{a1} value in this study is attributed to the simplified harmonic input motion used in this series of shake table experiments, with a dominant frequency of 2 Hz (0.5 sec), which resulted in unrealistically low spectral accelerations at other response periods.

The variation of estimated D_s was strongly affected by the first three terms in Equation (4.1). The terms $c1$ and $c2$ are based on the calculated *LBS* and are important variables in shear-induced settlement calculation. Another important factor is the error term (ε), which varies between -0.5 and 0.5. Its effect on the estimated D_s is presented in Table 4.1.

Table 4.1 Details of parameters used to estimate shear-induced settlement for Shake 1-1.

Variable	$FS_L = 0.80$		
$\varepsilon_{\text{shear}}$ (%)	51.2		
LBS	79.7		
c1	-7.84		
c2	0.014		
Q (kPa)	41.6		
B (m)	1.3		
H_L (m)	1.55		
CAV_{dp} (g.sec)	1.82		
S_{a1} (g)	0.07		
ε	-0.5	0.0	0.5
D_s (cm)	2[a]	3.3[b]	5.4[c]

[a]Mean - σ; [b]Mean; and [c]Mean + σ.

4.3 COMPARISON OF OBSERVED AND ESTIMATED FOUNDATION SETTLEMENTS

Liu and Dobry [1997] presented upper and lower boundaries for the normalized settlement data based on field observations from the 1964 Niigata and 1990 Luzon Philippine earthquakes against normalized building width. In this study, the normalized building width ratio (B/H_L) was 1.0 (B = 1.3 m and H_L = 1.3 m). The range of normalized settlement (S_t/H_L) based on the illustrated upper and lower bounds presented in Liu and Dobry [1997] was from 0.02 to 0.175. The estimated settlement based on these limits are in the range of 2.6–22.7 cm for Shake 1-1. The measured total settlement of the foundation in case of Shake 1-1 was 28 cm, which was 19% larger than the upper limit recommended by Liu and Dobry [1997].

In addition, Bray and Macedo's simplified procedure was used to estimate the liquefaction-induced foundation settlement for Shake 1-1. The total liquefaction-induced building settlement is the sum of volumetric-induced (D_v), shear-induced (D_s), and ejecta-induced settlement (D_e), as presented in Bray and Macedo [2017]:

$$D_t = D_e + D_v + D_s \tag{4.3}$$

The volumetric-induced settlement was calculated based on Ishihara and Yoshimine's chart [1992], and the shear-induced settlement of the foundation was obtained using Bray and Macedo's simplified method, described above.

The effect of ejecta-induced settlement is still not well quantified; ground failure indices or Ishihara's ground failure design chart [Ishihara 1985] can help estimate the amount of ground loss due to ejecta formation (D_e) [Bray and Macedo 2017]. Recently, an exploratory study based on a series of medium-scale shake table tests was conducted at UNR to correlate the volume of the ejecta to the total settlement of the foundation. The results indicated a linear relationship between ejecta volume and total foundation settlement up to a threshold volume of ejecta, beyond which the increase in the volume of ejecta had no considerable impact on total liquefaction-induced foundation settlement [Jahed Orang et al. 2019a]. In this study, it was difficult to measure the amount of ejecta due to the significant water flow to the ground surface; however, based on post-shaking foundation settlement measurement, the ejecta appears to contribute up to 17% of the total settlement (i.e., 4.8 cm out of 28 cm). Nonetheless, there is still no well-calibrated correlation to estimate the amount and contribution percentage of ejecta-induced settlement.

A detailed summary of the estimated and measured total settlement of the foundation for Shake 1-1 is provided in Tables 4.2 and 4.3 and Figure 4.1. The estimated settlement values in Table 4.2 are based on FS_L = 0.80, ranging from 7.5 cm–10.9 cm depending on the error term (i.e., $-0.5 \leq \varepsilon \leq 0.5$). The estimated total settlement value based on ε = 0.5 had the least deviation from the measured total settlement of the foundation; see Figure 4.1. The estimated settlement values excluded the effect of sediment ejecta (D_e), and its inclusion can increase the estimated settlement values accordingly. Additionally, probabilistic-based methods—such as Moss et al. [2006] and Cetin et al. [2009—can be used to calculate the volumetric component of liquefaction-induced settlement, which can increase the confidence interval around the total settlement calculation. Overall, the average estimated liquefaction-induced foundation settlement based on Bray and

Macedo [2017] underestimated the observed foundation settlement in this study by 68%. Bray and Luque [2017] employed this simplified procedure for a building in Christchurch Central Business District and reported conservative estimations, while the measured settlement values based on centrifuge tests conducted by Dashti [2009] reported underestimation of measured settlement values compared to the estimated values based on Bray and Macedo's [2017] simplified procedure. The range of uncertainty for the estimated settlement is mainly due to the assumptions made in this simplified procedure, as well as to the unrealistically low S_{a1} value generated in this series of experiments.

Table 4.2 Estimated settlement for Shake 1-1 (values in cm).

Parameter	Mean - σ	Mean	Mean + σ
D_v	5.5	5.5	5.5
D_s[a]	2.0	3.3	5.4
$D_t = D_v + D_s$	7.5	8.8	10.9

[a]Based on calculated $FS_L = 0.80$.

Table 4.3 Measured settlement during Shake 1-1 (values in cm).

Parameter	Value
Settlement during shaking	23.2
Post shaking settlement	4.8
Total Settlement Dt	28.0

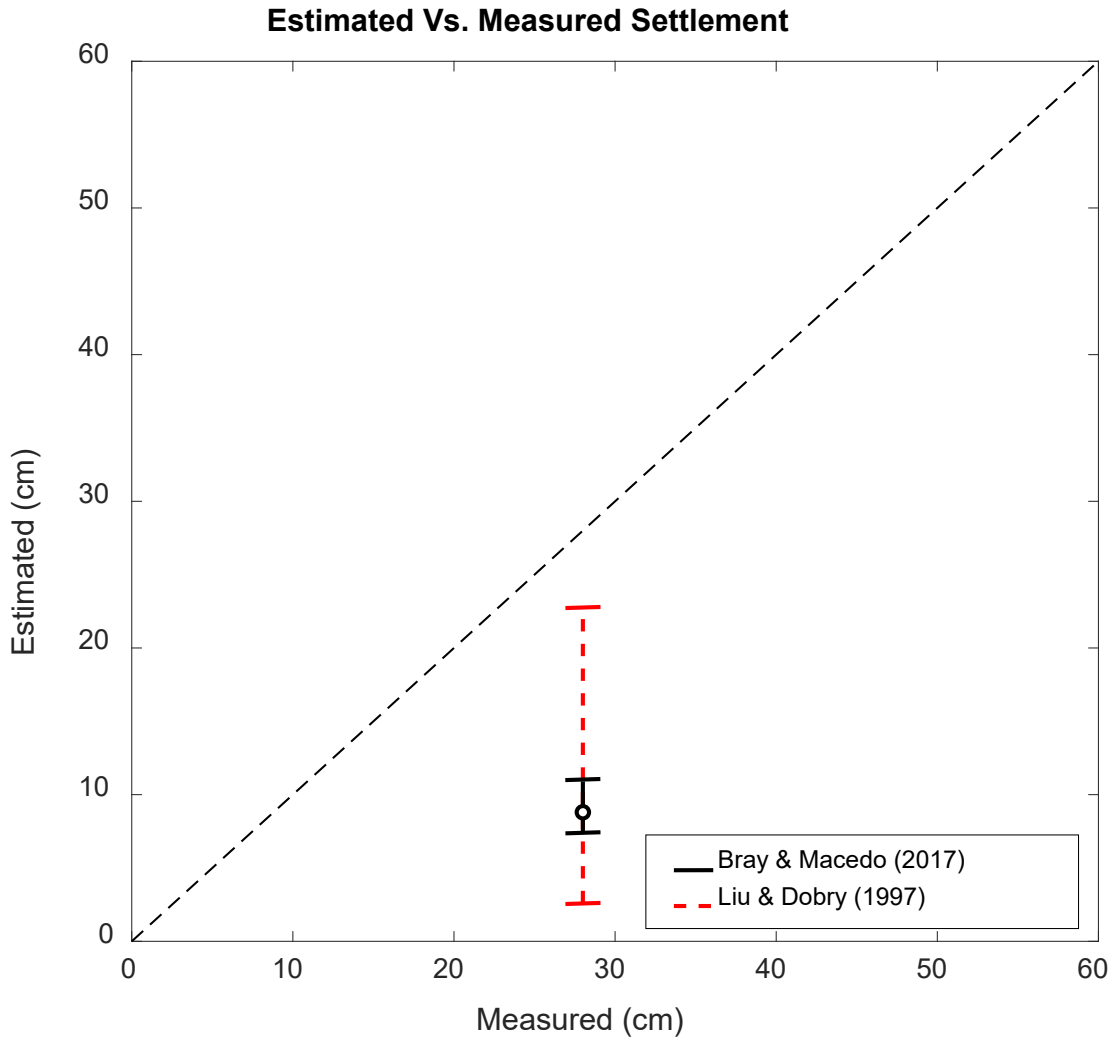

Figure 4.1 **Estimated versus measured total settlement of the foundation for Shake 1-1.**

5 Efficiency Evaluation of Different Mitigation Measures

5.1 SETTLEMENT MITIGATION EFFICIENCY

The application of various liquefaction mitigation techniques has been discussed in Section 1.2.3. Figure 5.1 illustrates the Settlement Mitigation Efficiency (SME) of different ground improvement methods to mitigate liquefaction-induced foundation settlement, including stone columns [Adalier et al. 2003], densification [Olarte et al. 2017; Rasouli et al. 2018], prefabricated vertical drains (PVD) [Olarte et al. 2017]), and structural walls [Olarte et al. 2017; Rasouli et al. 2018], along with the use of helical piles (this study). The measured foundation settlements (S_f) were normalized with respect to the liquefiable layer thickness (H_L) for all provided datasets in Figure 5.1. The SME is defined as the foundation settlement difference between the baseline and mitigated test divided by the baseline foundation settlement. As presented in Figure 5.1, the previous liquefaction mitigation methods resulted in lower efficiency as the S_f / H_L increased; however, the use of helical piles provided high efficiency regardless of the S_f / H_L calculation. The largest SME achieved in the previous research reached 67%, whereas the application of helical piles yielded 96% SME on average, which was substantially higher compared to other methods.

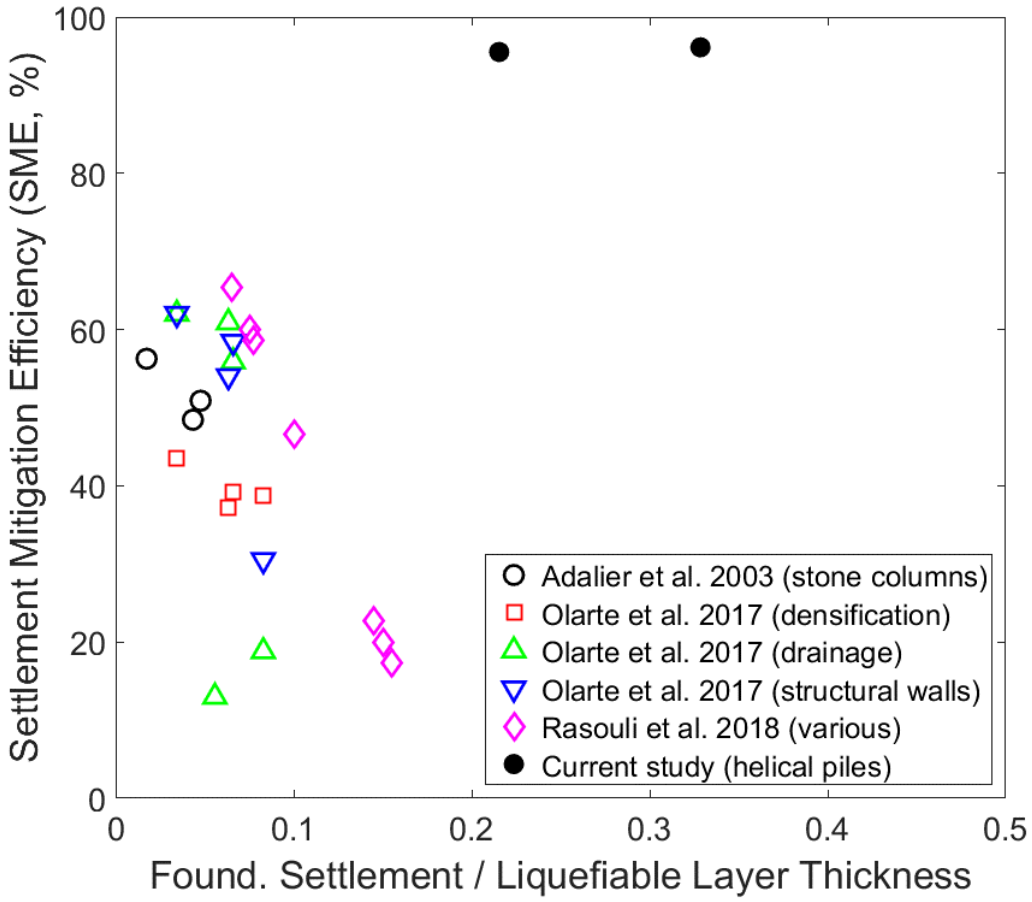

Figure 5.1 **Settlement mitigation efficiency versus normalized foundation settlement for different mitigation measures in liquefaction-induced foundation settlement.**

5.2 TILTING MITIGATION EFFICIENCY

Tilting of the foundations as a result of liquefaction is one of the important aspects to be considered when evaluating the efficacy of a selected liquefaction mitigation methodology. Figure 5.2 presents the tilting mitigation efficiency (TME) of these ground improvement approaches. The higher embedment depth will result in higher restraint against foundation rocking and tilting. Thus, the rotation of the foundation due to liquefaction is normalized with the ratio of embedment depth to foundation width [i.e., Arctan (D_f / B)]. The use of various methods under different test conditions can also result in negative TMEs, which indicates an increase in the foundation tilt compared to the Baseline test and an unsatisfactory performance; see Figure 5.2. The use of helical piles resulted in 99% TME on average, exhibiting a satisfactory efficiency amongst all other methods. The significantly improved performance of the shallow foundation was observed consistently during both shakes. This series of large-scale shake table experiments substantiated the state-of-the-practice information on the salient performance of helical piles in liquefiable ground by providing high settlement and rotation mitigation efficiencies.

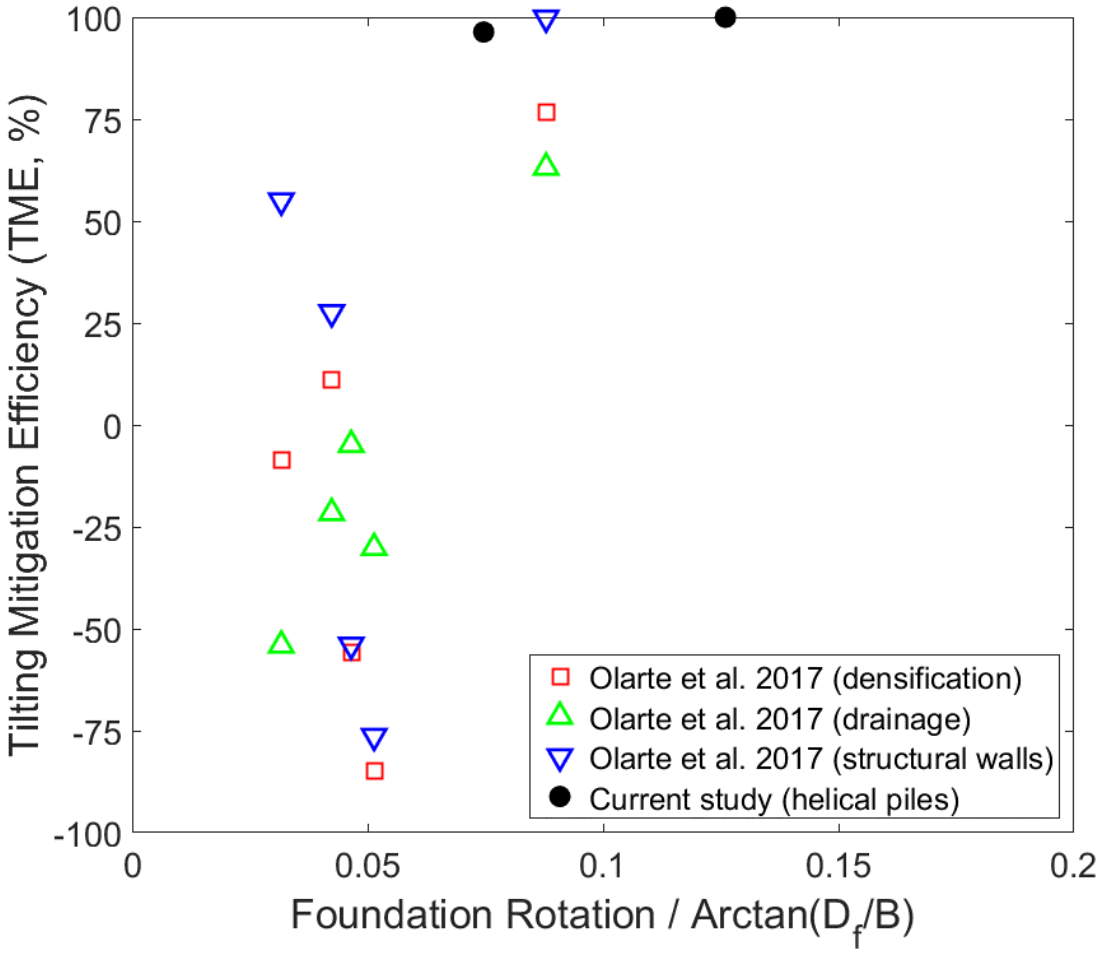

Figure 5.2 **Tilting mitigation efficiency versus normalized foundation rotation for different mitigation measures in liquefaction-induced foundation rotation.**

5.3 INFLUENCE OF HELICAL PILES ON THE SUPERSTRUCTURE RESPONSE

The implementation of different ground improvement techniques can increase the structural demand due to the amplified superstructure response. The tradeoff between liquefaction mitigation measures and the corresponding increase in structural demand should be considered when exploring different mitigation strategies [Olarte et al. 2017]. In this series of shake table tests, the target foundation contact pressure was replicated using several steel plates on top of the foundation to simulate the superstructure response. The measured acceleration and lateral displacement of the shallow foundation may provide insight into the superstructure response, considering the rigid nature of the model superstructure used in the experiments. The response acceleration time histories on top of the foundation were measured during Shake 1 for both tests; see Figure 5.3. According to Figure 5.3, the comparison between the recorded foundation motions in the Baseline and Helical pile tests shows an increased amplitude in the acceleration time history in the Helical Pile test, which is further manifested at short periods in the transfer function and amplification factor plots as well. This increase in the structural response at short periods in the Helical Pile test

implies the subsequent increase in the structural demand due to the use of helical piles. The increased response intensity in the Helical Pile test was mainly evident at short periods (i.e., T = 0.1–0.3 sec).

Figure 5.3 further illustrates the calculated transfer functions for the Baseline and Helical Pile tests, along with the code-based recommended transfer function [ASCE 41-17], which has been developed for buildings with shallow embedded foundations. The transfer functions for both tests are fairly consistent with the code-based transfer function from the comparison plots. Moreover, the higher variability within the transfer function in the Helical Pile test confirms the increase in structural demand, especially in shorter periods (i.e., around T = 0.1 sec). This can be attributed to a stiffer response of the soil–pile–foundation system in the Helical Pile test. This observation further highlights the importance of short-period structural response when helical piles are used to mitigate liquefaction-induced settlement. Thus, care should be taken considering the use of any liquefaction mitigation measures that can alter the soil–foundation system's stiffness due to higher superstructure demand, along with their settlement and tilting mitigation efficiencies.

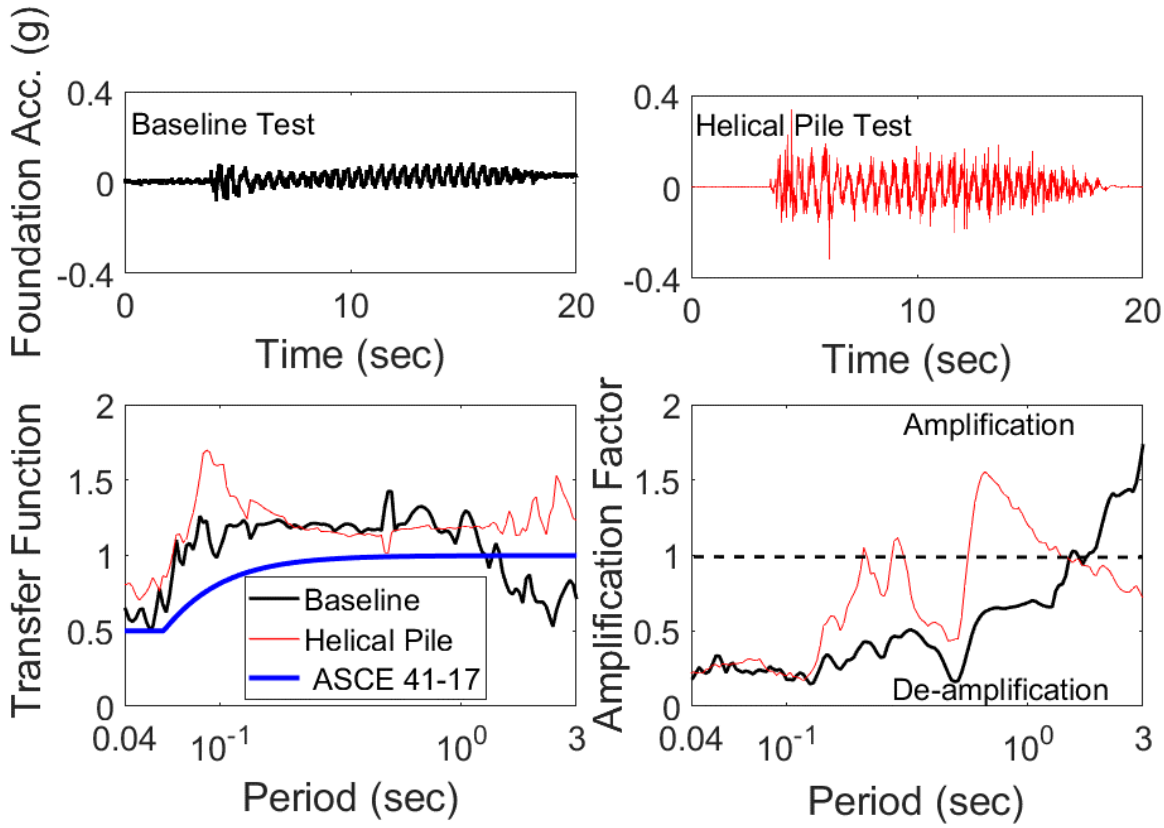

Figure 5.3 **Comparison between foundation acceleration time histories, transfer functions, and amplification factors in Baseline and Helical Pile tests during Shake 1.**

6 Concluding Remarks

Two test series (one without any mitigation and one using helical piles as a mitigation measure) with similar ground conditions and input motions—but with different soil–foundation response characteristics—were conducted at the UCSD's Powell Laboratory. In the first test series (i.e., Baseline tests) a shallow rigid foundation was placed atop a three-layer model ground, including a shallow liquefiable medium representing typical soil profiles observed in past earthquakes. In the second test series (i.e., Helical Pile tests) a group of helical piles was used to underpin the shallow foundation in a similar model ground. This study aimed at evaluating the liquefaction-induced settlement of a shallow foundation and examining the dynamic behavior of helical piles and the effectiveness of using these deep foundation elements in reducing liquefaction-induced foundation settlement and tilt. A summary of the main findings throughout this study is provided below:

- This series of 1*g* shake table tests are the first set of experimental data at this scale exploring the response of a soil–foundation–superstructure system to liquefaction-induced ground movement effects including all three controlling mechanisms, namely: (1) shear-induced, (2) volumetric-induced, and (3) ejecta-induced. The data obtained in the Baseline test provides researchers and practicing engineers with a benchmark dataset to validate numerical simulations focused on the liquefaction-induced settlement of buildings as well as future evaluation of effective mitigation strategies.
- Realistic reproduction of surface manifestation of liquefaction and sand ejecta is a key highlight of this experimental study, illustrating the benefits of large-scale 1*g* shake table testing.
- A dense array of high-resolution accelerometers was utilized for system identification, capturing the fundamental frequency of the model ground (i.e., around 5 Hz) by establishing transfer functions. This dataset was further used to characterize the shear-wave velocity profile of the model ground. As the testing proceeded deeper into the dense layer, the shear-wave velocity increased. Two sets of CPT tests were conducted in the Helical Pile tests, one before and one after Shake 1, to evaluate further the continuous variations in the relative density of the three-layered soil profile. The variation of cone tip resistance indicated higher values inside the dense layer, which is in line with the observed elevated shear-wave velocity values. Additionally, higher cone tip resistance was measured after

Shake 1 especially at the bottom half of the liquefiable layer and the top half of the dense layer.

- The EPWP generation at different depths indicated extensive liquefaction and pore-water pressure buildup in the middle of the dense layer even after shaking ceased. The EPWP isochrones became relatively uniform along with the depth in both the free-field and below the foundation arrays in the Baseline and the Helical Pile tests after Shake 1. Consequently, the transient hydraulic gradients vanished after the end of ground shaking. The calculation of flow velocity, based on Darcy's law and assuming 1D flow inside the ground, indicated the direction of flow on top of the dense layer and the boundary of the dense/loose layers was toward the dense layer (downward flow), whereas inside the loose layer, the direction of flow was upward. This further demonstrates how EPWP dissipation at the middle of the dense layer did not occur even after the shaking ended, especially in the downward direction of flow. The upward flow direction in the loose layer was confirmed by the observed sand ejecta after shaking ceased. Moreover, EPWP contour plots at different time steps indicated reduced pore-water pressure generation in the Helical Pile test. The extent of EPWP reduction was more considerable in the zone of helical pile influence at the top of the dense layer and the bottom of the liquefiable layer. The densification of the area around helical piles, with the changes in the load-carrying patterns of the coupled pile-foundation-ground model system in the Helical Pile tests, explains the observed EPWP difference between these two test series.
- The maximum CAV_{dp} was measured at the middle of the dense layer in the case of the free-field array, where the corresponding maximum value for the below foundation array was observed at the bottom of the liquefiable layer. This indicates higher acceleration at similar depths in each array, which is in line with the presented acceleration time histories. The CAV_{dp} values were also used for calculating shear-induced settlement of the foundation based on Bray and Macedo's [2017] simplified procedure. The IMs (including CAV_{dp}) were also estimated based on DEEPSOIL version 7.0 analysis assuming free-field array with no liquefaction condition for shear-induced settlement of the foundation as suggested by Bray and Macedo [2017]. The use of CAV_{dp} at different depths and locations resulted in lower consistency of the estimated settlement values compared with the observed settlement, whereas utilizing IM parameters (i.e., in this case, CAV_{dp} and S_{a1}) at the free field array; no liquefaction condition yielded a better estimate for the shear-induced component of the foundation settlement.
- Implementing various protective measures on the strain gauges resulted in the high functionality of these strain-measuring elements. The bending moments, obtained through the measured bending strains along with the depth of the ground model, were used further to inspect the dynamic response of the single-helix helical piles. All the helical piles exhibited a similar trend in their bending moment response in both shakings. The higher bending moment difference between the two shakes was observed at the bottom half of the liquefiable layer. The highest bending moment at all of the helical piles observed at the loose-dense layer interface was in line with the observation in the steel-driven piles in layered deposits (i.e., shear discontinuity effect).

- Measured near-foundation and foundation settlement trends displayed a local shear failure mechanism in the Baseline test, which is supported by observed heave in the surrounding ground and excessive punching settlement of the foundation. Post-shaking settlements were carefully quantified and attributed to ground loss due to observed sand boils as well as to post-liquefaction consolidation of the liquefiable layer.
- The measured near-foundation settlements were comparable in both test series during Shake 2, whereas excessive heave was observed in the near-foundation ground due to bearing capacity failure of the unsupported shallow foundation in the Baseline test during Shake 1. A higher portion of the foundation settlement took place during shakings in both the Baseline and Helical Pile tests; however, the foundation supported by helical piles did not experience any settlement after both shakings. The use of helical piles resulted in almost no measured differential settlement and tilt of the foundation.
- The observed foundation settlement accumulation in both test series shed light on the contribution of different liquefaction-induced settlement mechanisms. The only contributing mechanisms of the foundation settlement during the Helical Pile tests were transient high-hydraulic gradients and SSI ratcheting during shakings. During each shake, the settlement accumulation rate was significantly reduced using a group of helical piles to support the shallow foundation. The contribution of ejecta-induced and volumetric-induced (except high hydraulic transient gradients) components of foundation settlement were eliminated during the Helical Pile tests.
- Two simplified procedures were used to estimate the liquefaction-induced settlement of the foundation: see Liu and Dobry [1997] and Bray and Macedo [2017]. The normalized settlement versus normalized width of the foundation presented by Liu and Dobry [1997] indicated settlement values in the range of 2.6–22.7 cm, which is lower than the 28 cm measured settlement of the foundation in the case of Shake 1-1. Using Bray and Macedo's [2017] simplified procedure resulted in a total settlement of the foundation ranging from 7.5 cm to 10.9 cm (excluding ejecta-induced settlement), which is also lower than the measured total settlement value (i.e., 28 cm). Both methods underestimated the measured total settlement obtained through this shake table study.
- Comparison between various mitigation techniques revealed the salient performance of helical piles in reducing settlement and tilt of the shallow foundation. Considering the differences in testing conditions, including the type of physical model test, simulated ground model, structural model characteristics, and input motions, the highest settlement and tilting mitigation efficiencies (i.e., SME and TME) were achieved using four single-helix helical piles in shallow liquefiable deposits. Nonetheless, measured acceleration time histories and the calculated transfer functions in both tests indicated amplified response due to increased stiffness of the soil–pile–foundation system in the Helical Pile test. This study, in conjunction with previous research, suggests a holistic strategy in exploring the efficiency of different liquefaction-mitigation measures considering the amplified demand for the superstructure.

Overall, this study demonstrated the significant contribution of the results of 1*g* shake table tests in providing a broader understanding of the liquefaction-induced building settlement phenomenon by reproducing all the controlling mechanisms. Additionally, this series of large-scale shake table tests provided useful insight into the efficacy of helical piles as a reliable countermeasure in liquefaction-induced foundation settlement and rotation. This series of large-scale tests focused on evaluating the effects of a shallow liquefiable layer on the response of a shallow foundation that is consistent with the observed damage during past earthquakes. One limitation of shake table experiments is the inability to reproduce higher confining pressures observed at deeper depths, which should be considered in utilizing the results of this study for deeper liquefiable deposits. Finally, the results of this study were obtained on a specific ground condition, foundation contact pressure, and input motion characteristics. Caution should be taken in the real built environment since any change or combined variation of these factors can ultimately affect the performance of helical piles in liquefiable grounds.

REFERENCES

Abdelghany Y. (2008). *Monotonic and Cyclic Behavior of Helical Screw Piles Under Axial and Lateral Loading,* Department of Civil and Environmental Engineering, University of Western Ontario, London, Ontario, Canada.

Abdoun T., Dobry R., O'Rourke T.D., Goh S.H. (2003). Pile response to lateral spreads: Centrifuge modeling, *J. Geotech. Geoenviron. Eng.,* 129(10):869–878, https://doi.org/10.1061/(ASCE)1090-0241(2003)129:10(869).

Adachi T., Iwai S., Yasui M., Sato Y. (1992). Settlement and inclination of reinforced concrete buildings in Dagupan City due to liquefaction during 1990 Philippine earthquake, *Proceeding, 10th World Conference on Earthquake Engineering,* 2:147–152, A.A. Balkema Rotterdam, The Netherlands.

Adalier K., Elgamal A., Meneses J., Baez J.I. (2003). Stone columns as liquefaction countermeasure in non-plastic silty soils, *Soil Dyn. Earthq. Eng.,* 23(7):571–584, https://doi.org/10.1016/S0267-7261(03)00070-8.

ASCE (2017). *Seismic Evaluation and Retrofit of Existing Buildings: ASCE/SEI, 41-17*, Reston. VA.

Ashford S.A., Rollins K.M., Bradford S.C., Weaver T.J., Baez J.I. (2000). Liquefaction mitigation using stone columns around deep foundations: Full scale test results, *Transp. Res. Rec.,* 1736:110–118, https://doi.org/10.3141/1736-14.

Badanagki M., Dashti S., Kirkwood P. (2018). Influence of dense granular columns on the performance of level and gently sloping liquefiable sites, *J. Geotech. Geoenviron. Eng.,* 144(9), https://doi.org/10.1061/(ASCE)GT.1943-5606.0001937.

Bahadori H., Motamedi H., Hasheminezhad A., Motamed R. (2020). Shaking table tests on shallow foundations over geocomposite and geogrid-reinforced liquefiable soils, *Soil Dyn. Earthq. Eng.,* 128, https://doi.org/10.1016/j.soildyn.2019.105896.

Bahmanpour A., Towhata I., Sakr M., Mahmoud M., Yamamoto Y., Yamada S. (2019). The effect of underground columns on the mitigation of liquefaction in shaking table model experiments, *Soil Dyn. Earthq. Eng.,* 116(3):15–30, https://doi.org/10.1016/j.soildyn.2018.09.022.

Bastidas A M.P. (2016). *Ottawa F-65 Sand Characterization*. Ph.D. thesis, Department of Civil and Environmental Engineering, University of California, Davis, CA.

Borghei A., Ghayoomi M., Turner M. (2020). Centrifuge tests to evaluate seismic settlement of shallow foundations on unsaturated silty sand, *Proceedings, Geo-Congress 2020: Geotechnical Earthquake Engineering and Special Topics,* ASCE, Reston, VA, pp. 198–207.

Boulanger R.W., Khosravi M., Khosravi A., Wilson D.W. (2018). Remediation of liquefaction effects for an embankment using soil-cement walls: Centrifuge and numerical modeling, *Soil Dyn. Earthq. Eng.,* 114:38–50, https://doi.org/10.1016/j.soildyn.2018.07.001.

Boulanger R.W., Kutter B.L., Brandenberg S.J., Singh P., Chang, D. (2003). Pile foundations in liquefied and laterally spreading ground during earthquakes: centrifuge experiments and analyses, *Report No. UCD/CGM-03/01*. Center for Geotechnical Modeling, Department of Civil and Environmental Engineering, University of California, Davis, CA.

Bray J.D., Cubrinovski M., Zupan J., Taylor M. (2014). Liquefaction effects on buildings in the Central Business District of Christchurch, *Earthq. Spectra,* 30(1):85–109, https://doi.org/10.1193/022113EQS043M.

Bray J.D., Dashti S. (2014). Liquefaction-induced building movements, *Bull. Earthq. Eng.,* 12:1129–1156, https://doi.org/10.1007/s10518-014-9619-8.

Bray J.D., Frost J.D. (eds.) (2010). Geo-engineering reconnaissance of the 2010 Maule, Chile, earthquake, GEER Report, http://learningfromearthquakes.org/2010-02-27-chile/images/2010_02_27_chile/pdfs/prel_report/GEER_Report_Chile_2010_Final.pdf, Accessed May 25, 2010.

Bray J.D., Luque R. (2017). Seismic performance of a building affected by moderate liquefaction during the Christchurch earthquake, *Soil Dyn. Earthq. Eng.,* 102:99–111, https://doi.org/10.1016/j.soildyn.2017.08.011.

Bray J.D., Macedo J. (2017). 6th Ishihara Lecture: Simplified Procedure for estimating liquefaction-induced building settlement, *Soil Dyn. Earthq. Eng.,* 102:215–231, http://dx.doi.org/10.1016/j.soildyn.2017.08.026.

Bray J.D., Markham C.S., Cubrinovski M. (2017). Liquefaction assessments at shallow foundation building sites in the Central Business District of Christchurch, New Zealand, *Soil Dyn. Earthq. Eng.,* 92:153–164, http://dx.doi.org/10.1016/j.soildyn.2016.09.049.

Bray J.D., Rollins K., Hutchinson T., Verdugo R., Ledezma C., Mylonakis G., Assimaki A., Montalva G., Arduino, P., Olson S.M., Kayen R., Hashash Y.M.A., Candia G. (2012). Effects of ground failure on buildings, ports, and industrial facilities, *Earthq Spectra,* 28(S1):S97–S11, https://doi.org/10.1193/1.4000034.

Bray J.D., Sancio R.B., Durgunoglu H.T., Onalp A., Youd T.L., Stewart J.P., Seed R.B., Cetin O.K., Bol E., Baturay M.B., Christensen C., Karadayilar T. (2004). Subsurface characterization at ground failure sites in Adapazari, Turkey, *J. Geotech. Geoenviron. Eng.*, 130(7):673–685, https://doi.org/10.1061/(ASCE)1090-0241(2004)130:7(673).

Bray J.D., Stewart J P. (2000). Chapter 8: Damage patterns and foundation performance in Adapazari. Kocaeli, Turkey Earthquake of August 17, 1999, in Reconnaissance Report, T.L. Youd, J.P. Bardet, and J.D. Bray, eds, Earthq. Spectra, Supplement A, 16(S1):163–189, https://doi.org/10.1193/1.1586152.

Bullock, Z., Dashti S., Liel A.B., Porter, K.A., Karimi Z. (2019). Assessment supporting the use of outcropping rock evolutionary intensity measures for prediction of liquefaction consequences, *Earthq. Spectra,* 35(4):1899–1926, https://doi.org/10.1193/041618EQS094M.

Bullock Z., Karimi Z., Dashti S., Porter K.A., Liel A.B., Franke K.W. (2018). A physics-informed semi-empirical probabilistic model for the settlement of shallow-founded structures on liquefiable ground, *Géotechnique,* 69(5):406–419, https://doi.org/10.1680/jgeot.17.P.174.

Campbell K.W., Bozorgnia Y. (2011). Predictive equations for the horizontal component of standardized cumulative absolute velocity as adapted for use in the shutdown of U.S. nuclear power plants, *Nucl. Eng. Des*., 241(7):2558–2569, https://doi.org/10.1016/j.nucengdes 933.2011.04.020.

Cerato A.B. (2019). Discussions on how to instrument helical piles in large-scale testing. *Personal Communication*.

Cerato A.B., Victor R. (2008). Effects of helical anchor geometry on long-term performance of small wind tower foundations subject to dynamic loads, *J. Deep Found. Inst.*, 2(1):30–41, https://doi.org/10.1179/dfi.2008.004.

Cerato A.B., Vargas T.M., Allred S.M. (2017). A critical review: state of knowledge in seismic behavior of helical piles, *J. Deep Found. Inst.*, 11(1): 39–87, https://doi.org/10.1080/19375247.2017.1414108.

Cerato A.B., Victor R. (2009). Effects of long-term dynamic loading and fluctuating water table on helical anchor performance for small wind tower foundations, *J. Perform. Constr. Fac.*, 23(4):251–261, https://doi.org/10.1061/(ASCE)CF.1943-5509.0000013.

Cetin K O., Bilge H.T., Wu J., Kammerer A.M., Seed R.B. (2009). Probabilistic model for the assessment of cyclically induced reconsolidation (volumetric) settlements, *J. Geotech. Geoenviron. Eng.*, 135(3):387–398, https://doi.org/10.1061/(ASCE)1090-0241(2009)135:3(387).

Cubrinovski M. (2013). Liquefaction-induced damage in the 2010–2011 Christchurch (New Zealand) earthquakes. *Proceedings, International Conference on Case Histories in Geotechnical Engineering.* Missouri University of Science and Technology, Rolla, MO.

Cubrinovski M., Green R.A., Allen J., Ashford S., Bowman E., Bradley B., Cox B., Hutchinson T., Kavazanjian E., Orense R., Pender M., Quigley M., Wotherspoon L. (2010). Geotechnical reconnaissance of the 2010 Darfield (Canterbury) earthquake, *Bull. N.Z. Soc. Earthq. Eng.*, 43(4):243–320, https://doi.org/10.5459/bnzsee.43.4.243-320.

Cubrinovski M., Bray, J.D., Taylor, M., Giorgini, S., Bradley, B., Wotherspoon, L., Zupan, J. (2011). Soil liquefaction effects in the central business district during the February 2011 Christchurch earthquake. *Seismol. Res. Lett.,* 82(6):893–904, https://doi.org/10.1785/gssrl.82.6.893.

Darby K.M., Hernandez G.L., DeJong J.T., Boulanger R.W., Gomez M.G., Wilson D.W. (2019). Centrifuge model testing of liquefaction mitigation via microbially induced calcite precipitation, *J. Geotech. Geoenviron. Eng.*, 145(10), https://doi.org/10.1061/(ASCE)GT.1943-5606.0002122.

Dashti S. (2009). *Toward Evaluating Building Performance on Softened Ground*, Ph.D. thesis, Department of Civil and Environmental Engineering, University of California, Berkeley, CA.

Dashti S., Bray J.D. (2013). Numerical simulation of building response on liquefiable sand, *J Geotech Geoenviron Eng.,* 139(8):1235–1249, https://doi.org/10.1061/(ASCE)GT.1943-5606.0000853.

Dashti S., Bray J.D., Pestana J.M., Riemer M.R., Wilson D (2010a). Mechanisms of the seismically induced settlement of buildings with shallow foundations on liquefiable soil, *J. Geotech. Geoenviron. Eng.*, 136(1):151–164, https://doi.org/10.1061/(ASCE)GT.1943-5606.0000179.

Dashti S., Bray J.D., Pestana J.M., Riemer M.R., Wilson D (2010b). Centrifuge testing to evaluate and mitigate liquefaction-induced building settlement mechanisms, *J. Geotech. Geoenviron. Eng.,* 136(7):918–929, https://doi.org/10.1061/(ASCE)GT.1943-5606.0000306.

Dobry R., O'Rourke T.D., Abdoun T. (2001). Centrifuge-based evaluation of pile foundation response to lateral spreading and mitigation strategies, *Report MCEER-01-SP01*, Multidisciplinary Center for Earthquake Engineering Research, 2000–2001:87–101. (Vol. 2000-2001, pp. 87-101).

Ebeido A., Elgamal A., Tokimatsu K., Akio A. (2019a). Pile and pile group response to liquefaction-induced lateral spreading in four large-scale shake table experiments. *J. Geotech. Geoenviron. Eng.,* 145(10), https://doi.org/10.1061/(ASCE)GT.1943-5606.0002142.

Ebeido A., Elgamal A., Zayed M. (2019b). Large scale liquefaction-induced lateral spreading shake table testing at the University of California San Diego, *Proceedings, Geo-Congress 2019: Earthquake Engineering and Soil Dynamics*, ASCE, Reston, VA, pp. 22–30.

El Naggar M.H., Abdelghany Y. (2007a). Seismic helical screw foundations systems, *Proceedings, 60th Canadian Geotechnical Conference*, Ottawa, Canada, Paper No. 160.

El Naggar, M.H., Abdelghany Y. (2007b). Helical screw piles (HSP) capacity for axial cyclic loadings in cohesive soils, *Proceedings, 4th International Conference on Earthquake Geotechnical Engineering*. June 25-28, Thessaloniki, Greece. Paper No. 1567.

Elsawy M.K., El Naggar M.H., Cerato A., Elgamal A. (2019a). Seismic performance of helical piles in dry sand from large-scale shaking table tests, *Géotechnique*, 69(12):1071–1085, https://doi.org/10.1680/jgeot.18.P.001.

Elsawy M.K., El Naggar M.H., Cerato A., Elgamal A. (2019b). Data reduction and dynamic *p-y* curves of helical piles from large-scale shake table tests, *J. Geotech. Geoenviron. Eng.*, 145(10), https://doi.org/10.1061/(ASCE)GT.1943-5606.0002146.

Eseller-Bayat E., Gokyer S., Yegian M.K., Alshawabkeh A. (2013). Liquefaction response of partially saturated sands: an empirical model, *J. Geotech. Geoenviron. Eng*., 139(6):872–879, https://doi.org/10.1061/(ASCE)GT.1943-5606.0000816.

Hashash Y.M.A., Musgrove M.I., Harmon J.A., Ilhan O., Xing G., Groholski D.R., Phillips C.A., Park D. (2020). *DEEPSOIL 7.0, User Manual*, University of Illinois at Urbana-Champaign, Urbana, IL.

Hausler E.A. (2002). *Influence of Ground Improvement on Settlement and Liquefaction: A Study Based on Field Case History Evidence and Dynamic Geotechnical Centrifuge Tests*, Ph.D. thesis, Department of Civil and Natural Resources Engineering, University of California, Berkeley, CA.

Hayden R.F., Baez J.I. (1994). State of practice for liquefaction mitigation in North America, *Proceedings, International Workshop on Remedial Treatment of Liquefiable Soils*, Public Works Research Institute, Tsukuba, Japan.

Hayden C.P., Zupan J.D., Bray J.D., Allmond J.D., Kutter B.L. (2015). Centrifuge tests of adjacent mat-supported buildings affected by liquefaction, *J. Geotech. Geoenviron. Eng.*, 141(3), https://doi.org/10.1061/(ASCE)GT.1943-5606.0001253.

Henderson D. (2013). *The Performance of House Foundations in the Canterbury Earthquakes*, Master's thesis, University of Canterbury, Christchurch, NZ, http://ir.canterbury.ac.nz/handle/10092/8741.

Honnette T.R. (2018). *Measuring Liquefied Residual Strength Using Full-Scale Shake Table Cyclic Simple Shear Tests*, Master's thesis, Department of Civil and Environmental Engineering, California Polytechnic State University, San Luis Obispo, CA.

Howell R., Rathje E.M., Kamai R., Boulanger R.W. (2012). Centrifuge modeling of prefabricated vertical drains for liquefaction remediation, *J Geotech Geoenviron Eng.*, 138(3):262–71, https://doi.org/10.1061/(ASCE)GT.1943-5606.0000604.

Iai S., Matsunaga Y., Morita T., Miyata M., Sakurai H., Oishi H, et al. (1994). Effects of remedial measures against liquefaction at 1993 Kushiro-Oki earthquake, *Proceedings, 5th U.S-Japan workshop on earthquake resistant design of lifeline facilities and countermeasures against soil liquefaction,* pp. 135–152, *Technical Report NCEER-94-0026*, National Center for Earthquake Engineering Research, Buffalo, NY.

ICC-ES (2017). *RAM JACK Foundation and Driven Foundation Systems*, ICC Evaluation Service, LLC, ESR-1854.

Ishihara K. (1985). Stability of natural deposits during earthquakes, *Proceedings, 11th International Conference on Soil Mechanics and Foundation Engineering,* San Francisco, CA, 1:321–376, A.A. Balkema Publishers.

Ishihara K., Yoshimine M. (1992). Evaluation of settlement in deposits following liquefaction during earthquakes, *Soils Found.,* 32(1):173–188, https://doi.org/10.3208/sandf1972.32.173.

Jacobs J.S. (2016). *Full-Scale Shake Table Cyclic Simple Shear Testing of Liquefiable Soil*, Master's Thesis, Department of Civil and Environmental Engineering, California Polytechnic State University, San Luis Obispo, CA, http://digitalcommons.calpoly.edu/theses/1527/.

Jafarian Y., Mehrzad B., Lee C.J., Haddad A.H. (2017). Centrifuge modeling of seismic foundation-soil-foundation interaction on liquefiable sand, *Soil Dyn. Earthq. Eng.,* (97):184–204, https://doi.org/10.1016/j.soildyn.2017.03.019.

Jahed Orang M., Bousheri R., Motamed R., Prabhakaran A., Elgamal A. (2020). Large-scale shake table experiment on the performance of helical piles in liquefiable soils. *Proceedings, DFI 45th Annual Conference on Deep Foundations,* Hawthorne, NJ.

Jahed Orang, M., Boushehri, R., Motamed, R., Prabhakaran, A., Elgamal, A. (2021b). An Experimental Evaluation of Helical Piles as a Liquefaction-Induced Building Settlement Mitigation Measure (Submitted to *Soil Dynamics and Earthquake Engineering*).

Jahed Orang M., Brukett S., Motamed R. (2019a). Experimental evaluation of spatial variability effects on liquefaction-induced settlements, *Proceedings, Geo-Congress 2019: Earthquake Engineering and Structural Dynamics,* ASCE, Reston, VA, pp. 294–303.

Jahed Orang M., Motamed R., Prabhakaran A., Elgamal A. (2021a). Large-scale shake table tests on a shallow foundation in liquefiable soils, *J. Geotech. Geoenviron. Eng.,* 147(1), https://doi.org/10.1061/(ASCE)GT.1943-5606.0002427.

Jahed Orang M., Toth J., Motamed R. (2019b). Experimental evaluation of dynamic response of helical piles in dry sand using 1g shaking table tests, *Proceedings, VII International Conference on Earthquake Geotechnical Engineering,* Rome, Italy, pp 4226–4234.

Karamitros D.K., Bouckovalas G.D., Chaloulos Y.K., Andrianopoulos K.I. (2013). Numerical analysis of liquefaction-induced bearing capacity degradation of shallow foundations on a two-layered soil profile, *Soil Dyn. Earthq. Eng.,* 44:90–101, https://doi.org/10.1016/j.soildyn.2012.07.028.

Karimi Z., Dashti S. (2016). Numerical and centrifuge modeling of seismic soil-foundation-structure interaction on liquefiable ground, *J Geotech Geoenviron Eng.*, 142(1), https://doi.org/10.1061/(ASCE)GT.1943-5606.0001346.

Karimi Z., Dashti S. (2017). Ground motion intensity measures to evaluate II: the performance of shallow-founded structures on liquefiable ground, *Earth. Spectra,* 33(1):277–298, https://doi.org/10.1193/103015eqs163m.

Karimi Z., Dashti S., Bullock Z., Porter K., Liel A.B. (2018). Key predictors of structure settlement on liquefiable ground: a numerical parametric study, *Soil Dyn. Earthq. Eng.,* 113:286–308, https://doi.org/10.1016/j.soildyn.2018.03.001.

Kavazanjian E., Orense R., Pender M., Quigley M., Wotherspoon L. (2010). Geotechnical reconnaissance of the 2010 Darfield (Canterbury) earthquake, *Bull. NZ. Soc. for Earthq. Eng.* 43 (4):243–320.

Khosravi M., Boulanger R.W., Tamura S., Wilson D.W., Olgun G., Wang Y. (2016). Dynamic centrifuge tests of soft clay reinforced by soil-cement grids, *J. Geotech. Geoenviron. Eng.,* 142(7), https://doi.org/10.1061/(ASCE)GT.1943-5606.0001487.

Kirkwood P., Dashti S. (2018). A centrifuge study of seismic structure-soil-structure interaction on liquefiable ground and implications for design in dense urban areas, *Earthq. Spectra,* 34(3):1113–1134, https://doi.org/10.1193/052417EQS095M.

Kirkwood, P., Dashti S. (2019). Influence of prefabricated vertical drains on the seismic performance of similar neighboring structures founded on liquefiable deposits. *Géotechnique,* 69(11):971–985, https://doi.org/10.1680/jgeot.17.P.077.

Kokusho T. (1999). Water film in liquefied sand and its effect on lateral spread, *J. Geotech. Geoenviron. Eng.*, 125(10):817–826, https://doi.org/10.1061/(ASCE)1090-0241(1999)125:10(817).

Lambe P.C., Whitman R.V. (1985). Dynamic centrifugal modeling of a horizontal dry sand layer, *J. Geotech. Eng.*, 111(3):265–287, https://doi.org/10.1061/(ASCE)0733-9410(1985)111:3(265).

Liu L., Dobry R. (1997). Seismic response of shallow foundation on liquefiable sand, *J. Geotech. Geoenviron. Eng.,* 123(6):557–567, https://doi.org/10.1061/(ASCE)1090-0241(1997)123:6(557).

Lu C.W. (2017). A simplified calculation method for liquefaction-induced settlement of shallow foundation, *J. Earthq. Eng.,* 21(8):1385–1405, https://doi.org/10.1080/13632469.2016.1264327.

Luque R., Bray J.D. (2017). Dynamic analyses of two buildings founded on liquefiable soils during the Canterbury earthquake sequence, *J. Geotech. Geoenviron. Eng.,* 143(9), https://doi.org/10.1061/(ASCE)GT.1943-5606.0001736.

Macedo J., Bray J.D. (2018). Key trends in liquefaction-induced building settlement, *J. Geotech. Geoenviron. Eng.,* 144(11), https://doi.org/10.1061/(ASCE)GT.1943-5606.0001951.

Mehrzad B., Jafarian Y., Lee C.J., Haddad A.H. (2018). Centrifuge study into the effect of liquefaction extent on permanent settlement and seismic response of shallow foundations, *Soils Found.,*(58(1):228–240, https://doi.org/10.1016/j.sandf.2017.12.006.

Mirshekari, M., Ghayoomi M. (2017). Centrifuge tests to assess seismic site response of partially saturated sand layers, *Soil Dyn. Earthq. Eng.*, 94:254–265, https://doi.org/ 10.1016/j.soildyn.2017.01.024.

Montoya B. M., DeJong J.T., Boulanger R.W. (2013). Dynamic response of liquefiable sand improved by microbial induced calcite precipitation, *Geotechnique,* 63(4):302–312

Moss R.E., Seed R.B., Kayen R.E., Stewart J.P., Der Kiureghian A., Cetin K.O. (2006). CPT-based probabilistic and deterministic assessment of in situ seismic soil liquefaction potential, *J. Geotech. Geoenviro. Eng.,* 132(8):1032–1051, https://doi.org/10.1061/(ASCE)1090-0241(2006)132:8(1032).

Motamed R., Orang M.J., Parayancode A., Elgamal A. (2020). Results of a class c blind prediction competition on the numerical simulation of a large-scale liquefaction shaking table test, *Proceedings, Geo-Congress 2020: Foundations, Soil Improvement, and Erosion*, pp. 334–342, Reston, VA.

Motamed R., Towhata I. (2009). Shaking table model tests on pie groups behind quay walls subjected to lateral spreading, *J. Geotech. Geoenviro. Eng.,* 136(3):477–489, https://doi.org/10.1061/(ASCE)GT.1943-5606.0000115.

Motamed R., Towhata I., Honda T., Yasuda S., Tabata K., Nakazawa H. (2009). Behaviour of pile group behind a sheet pile quay wall subjected to liquefaction-induced large ground deformation observed in shaking test in E-defense project, *Soils Found.,* 49(3):459–475, https://doi.org/10.3208/sandf.49.459.

Motamed R., Towhata I., Honda T., Tabata K., Abe A. (2013). Pile group response to liquefaction-induced lateral spreading: E-Defense large shake table test, *Soil Dyn. Earthq. Eng.,* 51:35-46, http://dx.doi.org/10.1016/j.soildyn.2013.04.007.

Mousavi S., Ghayoomi M. (2019). Liquefaction mitigation of silty sands via microbial induced partial saturation., *Proceedings, Geo-Congress 2019: Earthquake Engineering and Soil Dynamics*, pp. 304–312, Reston, VA.

Mousavi S., Ghayoomi M. (2021). Liquefaction mitigation of sands with nonplastic fines via microbial-induced partial saturation, *J. Geotech. Geoenviro. Eng.*, 147(2), https://doi.org/10.1061/(ASCE)GT.1943-5606.0002444

Olarte J., Paramasivam B., Dashti S., Liel A., Zannin J. (2017). Centrifuge modeling of mitigation-soil-foundation-structure interaction on liquefiable ground, *Soil Dyn. Earthq. Eng.* https://doi.org/10.1016/J.SOILDYN.2017.03.01.

Paramasivam B., Dashti S., Liel A. (2018). Influence of prefabricated vertical drains on the seismic performance of structures founded on liquefiable soils, *J. Geotech. Geoenviro. Eng.,* 144(10), https://doi.org/10.1061/(ASCE)GT.1943-5606.0001950.

Perko H.A. (2009). *Helical Piles: A Practical Guide to Design and Installation,* New York, NY, USA: John Wiley & Sons.

Prabhakaran A., Kyungtae K., Ebeido A., Jahed Orang, M., Motamed R., Elgamal A., Frazao C. (2020a). Polymer injection and associated site liquefaction remediation mechanisms, Proceedings, *17th World Conference on Earthquake Engineering, 17WCEE,* Sendai, Japan – September 13-18., Paper no: 4b-0024

Prabhakaran A., Kyungtae K., Jahed Orang M., Qiu Z., Ebeido A., Zayed M., Boushehri R., Motamed R., Elgamal A., Frazao C. (2020b). Polymer injection and liquefaction-induced foundation settlement: a shake table test investigation, Proceedings, *Geo-Congress 2020: Geotechnical Earthquake Engineering and Special Topics*, pp. 1–9, Reston, VA

Rasouli R., Towhata I., Akima T. (2016). Experimental evaluation of drainage pipes as a mitigation against liquefaction-induced settlement of structures, *J. Geotech. Geoenviron. Eng.,* 142 (9): https://doi.org/10.1061/(ASCE)GT.1943-5606.0001509.

Rasouli R., Towhata I., Rattez H., Vonaesch R. (2018). Mitigation of nonuniform settlement of structures due to seismic liquefaction, *J. Geotech. Geoenviro. Eng.,* 144(11), https://doi.org/10.1061/(ASCE)GT.1943-5606.0001974.

Sancio R.B., Bray J.D., Stewart J.P., Youd T.L., Durgunoglu H.T., Onalp A., Seed R.B., Christensen C., Baturay M.B., Karadayilar T. (2002). Correlation between ground failure and soil conditions in Adapazari, Turkey. *Soil Dyn Earthq Eng*., 22(9–12):1093–1102, https://doi.org/10.1016/S0267-7261(02)00135-5.

Shahbazi M., Cerato A.B., Allred S., El Naggar M.H., Elgamal A. (2020a). Damping characteristics of full-scale grouped helical piles in dense sands subjected to small and large shaking events, *Can. Geotech. J.,* 57(6):801–814, https://doi.org/10.1139/cgj-2018-0769.

Shahbazi M., Cerato A.B., El Naggar H M., Elgamal A. (2020b) Evaluation of seismic soil–structure interaction of full-scale grouped helical piles in dense sand, *Int. J. Geomech.,* 20(12), https://doi.org/10.1061/(ASCE)GM.1943-5622.0001876.

Tokimatsu K., Hino K., Suzuki H., Ohno K., Tamura S., Suzuki Y. (2019). Liquefaction-induced settlement and tilting of buildings with shallow foundations based on field and laboratory observation, *Soil Dyn. Earthq. Eng.,* 124: 268-279, https://doi.org/10.1016/j.soildyn.2018.04.054.

Tokimatsu K., Katsumata K. (2012). Liquefaction-induced damage to buildings in Urayasu City during the 2011 Tohoku Pacific earthquake, *Proceedings, International Symposium on Engineering Lessons Learned from the 2011 Great East Japan Earthquake*, pp. 665–674.

Tokimatsu K., Seed H.B. (1987). Evaluation of settlements in sands due to earthquake shaking, *J. Geotech. Eng.,* 113(8): 861–878, https://doi.org/10.1061/(ASCE)0733-9410(1987)113:8(861).

Tokimatsu K., Tamura S., Suzuki H., Katsumata K. Tokimatsu K. (2011). Quick report on geotechnical problems in the 2011 Tohoku Pacific Ocean earthquake, Tokyo Institute of Technology, CUEE #118:21–47 (in Japanese).

Toth J.A.W., Motamed R. (2017). Parametric study on liquefaction-induced building settlements using 1-g shake table experiments, *Proceedings*, *3rd International Conference on Performance-based Design in Earthquake Geotechnical Engineering,* Vancouver, Canada.

Vesic A.S. (1973). Analysis of ultimate loads of shallow foundations, *J. Soil Mech. Found. Div.* 99(1):45–73, https://doi.org/10.1061/JSFEAQ.0001846.

Yasuda S., Harada K., Ishikawa K., Kanemaru Y. (2012). Characteristics of liquefaction in Tokyo Bay area by the 2011 Great East Japan earthquake, *Soils Found.,* 52(5):793–810, https://doi.org/10.1016/j.sandf.2012.11.004.

Yegian M.K., Eseller-Bayat E., Alshawabkeh A., Ali S. (2007). Induced partial saturation for liquefaction mitigation: Experimental investigation, *J. Geotech. Geoenviro. Eng.,* 133:(4), https://doi.org/10.1061/(ASCE)1090-0241(2007)133:4(372).

Yoshimi Y., Tokimatsu K. (1977). Settlement of buildings on saturated sand during earthquakes, *Soils Found.,* 17(1):23–38, https://doi.org/10.3208/sandf1972.17.23.

Zeghal M., Elgamal A.W. (1994). Analysis of site liquefaction using earthquake records, *J. Geotech. Eng.,* 120(6):996–1017, https://doi.org/10.1061/(ASCE)0733-9410(1994)120:6(996).

Zeghal M., Elgamal A.W., Zeng X., Arulmoli K. (1999). Mechanism of liquefaction response in sand–silt dynamic centrifuge tests, *Soil Dyn. Earthq. Eng.,* 18(1):71–85, https://doi.org/10.1016/S0267-7261(98)00029-3.

The Pacifi c Earthquake Engineering Research Center (PEER) is a multi-institutional research and education center with headquarters at the University of California, Berkeley. Investigators from over 20 universities, several consulting companies, and researchers at various state and federal government agencies contribute to research programs focused on performance-based earthquake engineering.

These research programs aim to identify and reduce the risks from major earthquakes to life safety and to the economy by including research in a wide variety of disciplines including structural and geotechnical engineering, geology/seismology, lifelines, transportation, architecture, economics, risk management, and public policy.

PEER is supported by federal, state, local, and regional agencies, together with industry partners.

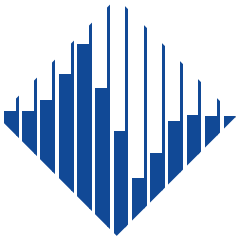

PEER Core Institutions

University of California, Berkeley (Lead Institution)
California Institute of Technology
Oregon State University
Stanford University
University of California, Davis
University of California, Irvine
University of California, Los Angeles
University of California, San Diego
University of Nevada, Reno
University of Southern California
University of Washington

PEER reports can be ordered at https://peer.berkeley.edu/peer-reports or by contacting

Pacific Earthquake Engineering Research Center
University of California, Berkeley
325 Davis Hall, Mail Code 1792
Berkeley, CA 94720-1792
Tel: 510-642-3437
Email: peer_center@berkeley.edu

ISSN 2770-8314
https://doi.org/10.55461/UFHH2641